CHARACTERIZATION OF THE STRUCTURE, STABILITY, MECHANICAL AND ELECTROCHEMICAL PROPERTIES OF METALLIC GLASSES

MSc Maria Jazmin Duarte Correa

Supervisors:
Dr. Aldo Humberto Romero Castro
Dr. Jorge Serrano Gutiérrez
Tutor:
Prof. Daniel Crespo Artiaga

within the Thesis co-supervision agreement between the Programa de Doctorat en Física Computacional i Aplicada at the UPC, Spain and the Programa de Doctorado en Ciencias con especialidad en Materiales at the CINVESTAV-Querétaro, Mexico

Barcelona, December 2012.

CENTRO DE INVESTIGACION Y DE ESTUDIOS AVANZADOS
DEL INSTITUTO POLITECNICO NACIONAL
UNIDAD QUERETARO

UNIVERSITAT POLITECNICA DE CATALUNYA
DEPARTAMENT DE FISICA APLICADA
EPSC

CARACTERIZACION DE LA ESTRUCTURA, ESTABILIDAD, PROPIEDADES MECANICAS Y ELECTROQUIMICAS DE VIDRIOS METALICOS

MSc Maria Jazmin Duarte Correa

Directores de Tesis:
Dr. Aldo Humberto Romero Castro
Dr. Jorge Serrano Gutiérrez
Tutor:
Prof. Daniel Crespo Artiaga

dentro del convenio de cotutela de Tesis entre el Programa de Doctorat en Física Computacional i Aplicada de la UPC, España y el Programa de Doctorado en Ciencias con especialidad en Materiales del CINVESTAV-Querétaro, México

Barcelona, Diciembre 2012.

CENTRO DE INVESTIGACION Y DE ESTUDIOS AVANZADOS
DEL INSTITUTO POLITECNICO NACIONAL
UNIDAD QUERETARO

UNIVERSITAT POLITECNICA DE CATALUNYA
DEPARTAMENT DE FISICA APLICADA
EPSC

Acknowledgements

I want to express my gratitude to Cinvestav-Unidad Querétaro, Mexico, and to ESPC from Universitat Politècnica de Catalunya (UPC), Barcelona, Spain, which supported my research project over these years. Special recognition deserve my supervisors, Dr. Aldo Romero y Dr. Jorge Serrano, for their support and guidance in this work and their wise comments.

Thanks to Prof. Daniel Crespo, for his wise comments and sugestions, Dr. Eloi Pineda, Dr. Pere Bruna from UPC for their valuable support in the preparation and characterization of the samples as well as discussion of results.

Thanks to the Max-Planck Institut für Eisenforschung (MPIE), Düsseldorf, Germany, and Dr. Frank Renner for the valuable collaboration in this project. Thanks to all people at Max-Planck who participated in this work, M. Stratman, D. Raabe, J. Lengsfeld, S. Borodin, S. Klemm, K. Mayrhofer, A. Kotska, P.-P. Choi, S.S.A. Gerstl.

Thanks to Jingfei Chu for her collaboration during her Master Thesis at the MPIE. Thanks to Estefany Mondragón and Guillaume Roinsol for their participation during the elaboration of their respective *Trabajo de fin de carrera* (TFC) at the UPC.

Thanks to the European Synchrotron Radiation Facility (ESRF), Grenoble, France, for provision of synchrotron radiation facilities under proposals CGR-16-01-726 and HD-349 and thanks to G. Garbarino, G. Monaco, M. Krisch, R. Verbeni, for their participation in the project related with polyamorphism in Ce-based metallic glasses and thanks A. Labrador for assistance in using beamline BM16.

Thanks to W. H. Wang and K. Zhao from the Chinese Academy of Sciences, Institute of Physics, China for providing the Ce-based alloy.

This research was supported in part by CONACYT and UPC.

Thanks the support of Conacyt, México, through projects PPPROALMEX-DAAD-Conacyt and 152153.

Dedicatoria

A mis padres Francisco y María. Este logro es también suyo. Sus sabios consejos y enseñanzas me han llevado a ser la persona que ahora soy y a no rendirme ante las adversidades. Gracias.

A David por alentarme siempre a continuar con mis proyectos. Tú eres mi modelo a seguir, siempre trabajando para lograr tus metas sin darte por vencido. Gracias también por desvelarte conmigo y compartir tantos buenos momentos. A Paco y Karina por todo su apoyo y constante entusiasmo.

A Gilberto por su apoyo a pesar de la distancia. Gracias por creer en mi, tus consejos y tu enorme paciencia.

A mis amigos en Cinvestav, especialmente Ale, Ale, Alexs y Gis, Dany, Jeanneth, Rosy. A mis amigos en la UPC, en especial Isa, Fran, Rouger y Gemma, Victor y Delia. Con ustedes compartí tantos momentos y experiencias que hicieron que todo este proceso fuera más sencillo y agradable.

A mis amigos que compartieron este proceso de una manera más indirecta, pero igual de importante, Alexs, Arlette, Carito, Flavio, Jessica y Carlitos, Luis y Lety, Rosario, a quienes valoro por su sincera amistad.

A todos y cada uno de mis familiares y amigos, que han estado conmigo en cada etapa influenciando de manera positiva este proyecto.

Contents

List of Figures

List of Tables

Abstract

Metallic glasses are often referred as glassy or amorphous alloys. They lack long-range order and microstructural defects that are characteristics in crystals, such as grain and phase boundaries and dislocations. These new materials have demonstrated very interesting structural and mechanical properties derived from their homogeneity in composition and the absence of grain boundaries. Structural, mechanical or chemical properties, among others, may be even superior to those observed in conventional metallic alloys, and therefore attracted great scientific and technological interest. This thesis project aims to achieve a better understanding of amorphous metallic alloys. Three different families of metallic glasses have been selected for this thesis work. First, a Ce-based alloy has been used to analyze a polyamorphic transition upon application of pressure to a more densely packed structure. X-ray diffraction and inelastic x-ray scattering data show a polyamorphic transition in the 2–10 GPa range, and this transition presents a hysteresis cycle between both compression and decompression data. The effect of this transition on mechanical properties is then evaluated. Second, a family of Fe-based metallic glasses, or amorphous steels, has been selected to study their mechanical and electrochemical properties as a function of structure and composition, changing the Yttrium concentration and modifying the structure by thermal annealing up to a complete crystallization state. Finally, an entirely new alloy for biocompatible purposes has been designed, synthesized, and characterized. This new Zr-Ti based amorphous alloy does not contain toxic or unhealthy elements.

Resumen

Los vidrios metálicos, comunmente conocidos como aleaciones amorfas o vitrificadas, carecen de orden a largo alcance así como de defectos microestructurales comunes en los cristales, tales como dislocaciones o fronteras de grano y/o de fase. Esta nueva clase de materiales ha demostrado poseer propiedades muy interesantes derivadas de la ausencia de microestructura y la homogeneidad en su composición. Estas propiedades, estructurales, mecánicas y químicas, entre otras, pueden llegar a ser incluso superiores a las observadas en materiales convencionales, y por lo tanto los vidrios metálicos han atraido gran interés por parte de la comunidad científica así como de carácter tecnológico. En este proyecto de tesis se pretende obtener un mayor conocimiento sobre aleaciones metálicas amorfas, para lo cual se propusieron tres familias diferentes de vidrios metálicos. Primero, se utilizó una aleación de base Ce para analizar transiciones poliamórficas, entre un estado de baja densidad hacia una estructura densamente empaquetada, por efecto de la presión. Los resultados obtenidos por difracción de rayos X y dispersión inelástica de rayos X muestran una transición en un rango de presiones de 2 a 10 GPa presentando además histéresis con respecto a los datos obtenidos en compresión y descompresión. El efecto de dicha transición en las propiedades mecánicas de la aleación es también evaluado. En segundo lugar se eligió una familia de aleaciones de base Fe, conocidos también como aceros amorfos. Las propiedades mecánicas y electroquímicas en función de la estructura y la composición fueron evaluadas mediante la introducción de itrio como elemento microaleante y la modificación de la estructura por medio de tratamientos térmicos con la obtención de estructuras compuestas nanocristal-amorfo hasta una completa cristalización. Finalmente, se diseñó y sintetizó una aleación completamente nueva con el propósito de evaluar biocompatibilidad. La caracterización estructural básica de esta nueva aleación de base Zr-Ti sin elementos tóxicos y/o alergénicos muestra que es posible obtener aleaciones amorfas con las composiciones propuestas.

Chapter 1

Introduction

Metallic glasses (MGs) are metallic alloys with a disordered structure. More precisely, they lack long-range order and can be considered as frozen atomic configurations of a liquid phase [1]. The glassy state is reached when cooled liquid solidifies without crystallization by quenching, which is associated with the glass transition phenomena. Due to the nature of the metallic bonding, the formation of a non-crystalline metallic system would not be expected. However, this special phase of metals observed in the sixties [2] has been shown to combine some properties of the usual metals and the formability of usual oxide glasses. This makes research on MGs very attractive both for fundamental understanding of the glassy state and the development of tailored technological materials in metallurgy. The absence of microstructural features such as crystal plains, grain and phase boundaries or dislocations, contributes to their special structural, electric, magnetic and chemical properties [3, 4, 5, 6, 7].

Specially, with the synthesis of Bulk Metallic Glasses (BMGs), these materials have gained the attention of the scientific community. Different methods for MGs preparation are used such as ionic radiation, mechanical alloying, physical or chemical vapor deposition, solid reactions, among others. However the most widely used methods correspond to fast cooling and the $arc-melting$ and $melt-spinning$ processes used in this work are among them. The obtained alloys are non-equilibrium phases or meta-stable phases.

Unlike materials made for specific purposes, MGs are new-born materials, product of

pure scientific research, looking for applications. This can be done by: [8] (1) identifying their strengths, (2) their weaknesses and (3) exploring the applications based on (1) and sensitive to (2). Because of the lack of knowledge and information about their formation and properties, a deep theoretical and experimental study is needed to recognize the potential applications of these new materials.

The systems that usually present good glass forming ability (GFA) and retain a glassy state in bulk are multicomponent alloys mainly based on Zr, Ti, Cu, Fe, Ni, La, Pd, Pt, Co and Mg [9]. However, the wealth of possible metallic glass compositions and the lack of knowledge on the general trends in the dependence of various properties with composition, poses a challenge to industrial application and calls for a combined theoretical and experimental approach to investigate these materials. For this thesis project different families of metallic glasses were selected in order to evaluate the influence of some parameters, such as pressure and temperature, on structural, mechanical and electrochemical properties. To achieve this goal, production of the selected metallic alloys by using two of the conventional methods: melt-spinner and arc-melter processes is proposed. These methods of fast cooling rate, allow manufacturing ribbons of few micrometers thick and rods from 1 to several mm diameters of amorphous materials. Basic characterization of the samples obtained, in order to know the properties and initial state of the materials as produced, is also needed.

The different projects proposed in this work have the goal to achieve a better understanding in metallic glasses at different stages with the available tools. First, fabrication and optimization of metallic glasses with the specific knowledge of phase diagrams and thermodynamic parameters. Second, fundamental knowledge of some of the mechanical and structural properties of metallic glasses as function of applied external driving forces, such as pressure or temperature. Finally, practical knowledge of important properties for industrial applications such as mechanical and electrochemical properties.

1.1 Metallic glasses

One of the main challenges in the BGMs production is to get samples of bigger size. Nowadays, it has been possible to produce materials with a size bigger than 1 cm, for systems with at least three components. To understand the MGs formation, two main characteristics are under study: the glass-forming ability (GFA)and the glass forming range (GFR). The former is related to the critical cooling rate necessary to achieve the amorphous phase and the second is expressed in terms of the composition range where the amorphous phase is stable.

Thermodynamic and kinetic parameters determine if a material has good GFA characteristics. These parameters are: low entropy and low enthalpy and thus, low thermodynamic driving force for crystallization. Kinetic parameters such as low atomic mobility, associated with a high viscosity nearly independent of the temperature, suppress nucleation and/or growth of eutectic phases, solid solutions and crystalline intermetallics that correspond to stable or metastable phases. The low atomic mobility is favored in dense structures with random ordering. Such compact structure is more efficient in multicomponent systems, with different sizes, reducing the average free atomic volume [10].

In the cooling stage of an alloy, it is kinetically preferred the forming phase with the higher growth temperature and this phase is the one observed in the final microstructure. Therefore, a glass is formed if the isothermal of its glass transition temperature is higher than the growth temperature of any possible crystalline phase. Due to this fact, two different zones, where the MGs forming is possible, are under consideration. In regular eutectic systems, the best composition range for glass formation includes the eutectic composition. In the other hand, when an irregular eutectic system is considered, the best composition range is shifted with respect the eutectic composition. In both cases, the region where MGs forming is possible, lies between two composite formation zones, one vitreous region and one crystalline zone.

The region which promotes the glass formation can be defined by monitoring the amorphous and crystalline phases as a function of concentration. Examples of this

methodology have been implemented in binary Cu-Zr [11] and ternary Zr-Al-Cu [12] systems. In the case of larger systems, this methodology becomes more complex since the GFA has an strong dependence on the composition. Other method to identify the most favorable compositions for glass formation, is by centrifugal process at high temperatures [13]. This process consists in melting multicomponent alloys in a centrifugal machine. The melted alloy is slowly cooled at gravitational accelerations over 100,000 G. At the end of the process, several and distinct solidified phases appear. With these phases, it is possible to observe the crystallization sequence and the eutectic composition which solidifies with a lower rate. This information is useful to determine the most favorable region for glass forming.

1.2 Properties and applications

Due to the absence of grain boundaries in glassy alloys, these materials have special mechanical, electrical, magnetic and chemical properties. Ashby and Greer [3] show a table which summarizes some of their general properties, related with possible applications.

The microstructural properties, associated with the absence on grain boundaries, give to the material its corrosion resistance, its high dimensional precision in melted materials and a polished finish. BMGs have been shown excellent mechanical properties: low damping modes, high hardness, yielding limits, fracture resistance, and resilience per unit of mass and volume. Moreover, BMGs have shown up to 2% elastic limit which is one order of magnitude higher than in crystals where this value varies around 0.2% [4]. Co-based BMGs may reach excellent fracture resistance during compression, over 5 GPa [5, 6].

Among these properties, it is their soft magnetism that has led to the most significant applications. The microstructural homogeneity and the absence of magnetocrystalline anisotropy can give very low coercivity and low hysteretic losses [14]. The amorphous structure also results in high magnetic permeability and electrical resistivity almost independent of the temperature [15].

As a result, metallic glasses have found their way into common applications including iron-based soft magnetic material for the cores of distribution transformers, magnetic security strips, choke coils, high-frequency magnetic-shielding sheets, linear actuators and other small magnetic devices [16, 17].

Some other suggested properties include the use of MGs in precision tools, particularly, knife blades due to their high hardness. Regarding to their low damping modes and elastic properties, BMGs can be used as springs for automotive applications, or sporting goods such as racket frames or golf club heads. By combining hardness and absence of grain boundaries, these materials are suitable for digital applications and storage information. Given their polished finish and abrasion resistance, they can be used in fashion items where the mechanical properties are important. Other structural applications are precision optical items, precision gears for micro engines, diaphragms for pressure sensors and aircraft parts. Finally, their use in micro electrical-mechanical systems (MEMS) is proposed due to their high yielding limit, low loss-coefficients and high resistance.
At present, marketing for BMGs products have been successful in areas as defense applications, sports, cases for electronic devices, medical and bio-medical applications and fine jewelry [7].

Objectives

As the present thesis is focused on the response of different sort of metallic glasses to a change of one variable, which is composition or pressure, the main goals are summarized as follows:

- To establish the optimal conditions of synthesis evaluating the different concentrations, cooling rates, pressures in the chamber, among others, to obtain the desired metallic glasses.
- To achieve a better understanding of pressure-induced polyamorphic transitions in Ce-based metallic glasses.
- To unveil the dependence of corrosion resistance behaviour on structure of amorphous and devitrified Fe-base alloys.
- To analyse the microalloying effects of Y in stability of amorphous phase, mechanical and electrochemical properties of an amorphous steel.
- To develop a new composition of metallic glasses with biocompatible properties.

All the particular goals presented formerly are intended to guide us to a better understanding on the leading factors for the formation, structure and properties of the prior metallic glasses. Finally, it would be interesting to evaluate the potential applications of the produced materials that could improve some properties of the conventional ones.

Chapter 2

Structural and high frequency mechanical response upon application of pressure on a Ce-based metallic glass

Since the development of the diamond anvil cells during the late fifties, the high pressure research expanded quite a lot. Being the structural phase transitions of single crystals between the first systems to be characterized. However, the study of similar transitions in liquids and amorphous solids has been undertaken much later, due to the limited structural information available via X-ray and neutron diffraction techniques. Such transitions have been observed in liquid phosphorus [18] and sulfur [19], by X-ray diffraction (XRD) and inelastic X-ray scattering (IXS), accounting for static and dynamic signatures, respectively. More recently, the potential of metallic glasses for applications as structural materials has arose interest in the scientific community. The mixture of metallic binding with partial covalent bonds created by non-metals such as boron, carbon and phosphorous makes the study of polyamorphic transitions very appealing as a source of information about the role of the electronic structure on the transition. In this Thesis we report pressure dependent studies of the amorphous alloy $Ce_{70}Al_{10}Ni_{10}Cu_{10}$ by XRD and IXS using synchrotron radiation in the 0-25 GPa pressure range. A polyamorphic phase transition upon application of pressure is observed in the range of 2-15 GPa.

2.1 Background

2.1.1 Polyamorphic transitions

Phase transitions in materials, usually correlated to changes in electrical, magnetic, optical and many other physical properties are issues of novel and present scientific and technological interest. Those changes are now largely understood for crystalline system but less comprehended is the case of amorphous or glassy systems. A large effort has been given in the last few years in order to understand the changes in the quasi-disordered system and how pressure can affect its properties. For example, the term polyamorphism [20] refers to a transition between different amorphous phases or states, sometimes involving structural changes but also some other physical property. This phenomena happens to be quite analogous to the case of crystalline polymorphism. The density and entropy drive the phase transition and the system response due to changes in pressure and/or temperature.

In the past, there was a natural expectation that the disordered structure of liquids or glasses would have only one disordered phase. The lack of clear experimental evidence of a discontinuous change in the system volume in a given amorphous material, delayed the study of the amorphous polymorphism or polyamorphism. The evidence of a transition in amorphous ice from a low-density state, when compressed at 77 K, to a high-density amorphous ice at 0.6 GPa [21], changed the point of view concerning to polyamorphism. Nowadays the existence of more than one amorphous state in disordered systems is being increasingly observed in several materials. For liquids, for example, a liquid-liquid phase transition has been observed in phosphorus [18]. *In-situ* X-ray diffraction observations at high-pressure and high-temperature conditions suggest the formation of a polymeric phase at pressures above 1 GPa in addition to the known molecular liquid form of phosphorus.

In the case of glasses, pressure is usually the thermodynamic variable used to induce polyamorphism and is commonly correlated to changes in the system density. Other examples of this phenomena include Si, [22, 23, 24] binary liquids such as Y_2O_3-Al_2O_3, [25, 26] vitreous SiO_2 [27, 28] and GeAsS chalcogenide glasses [29]. In these cases, the

structural polyamorphic transitions often result from an increase in atomic coordination from the low density amorphous to a high density amorphous state. A model showing the different phase relations in Silicon is presented in Figure 2.1, which has been taken from reference [22]. The red arrows represent the transformation processes. The thick solid line is the melting temperature of the crystal Si. The thick dashed line is a speculated boundary between the low density amorphous (LDA) and the high density amorphous (HDA) phases. The thick dash-dotted line is the approximate location of the vitrification from a high density liquid (HDL) to a HDA phase. The thin dotted line is the boundary between diamond and β-tin structures of crystalline forms. The filled circle represent a second hypothetical critical point that could exist in water.

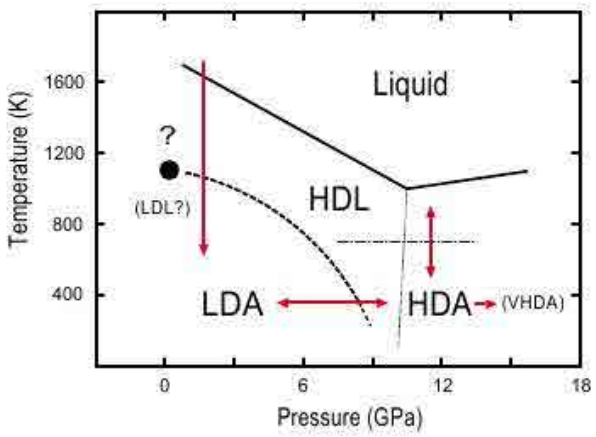

Figure 2.1: Schematic phase relations of amorphous and liquid Si proposed by Tetsuya Morishita [22].

Recently, polyamorphic transitions have been evidenced in nondirectional, densely-packed metallic glasses [9]. Using a combination of *in-situ* X-ray diffraction and theoretical calculations, a polyamorphic transition upon application of pressure in the 2-13.5 GPa range was stated in $Ce_{55}Al_{45}$ metallic glass [9]. *In-situ* X-ray diffraction patterns showed hysteresis in the pressure dependence of the specific volume upon compression and decompression, with 14% density difference between the two amorphous states of the metallic glass at ambient pressure. Those results were compared with *ab-initio* calculations and discussed in terms of a pressure-driven change in the localization of $4f$

Ce electronic states, similar to the behavior observed in the γ–α phase transformation in crystalline cerium [30, 31]. These results are depicted in Figure 2.2, where the open symbols are for compression and the solid symbols for decompression. The upper line represent the equation of states, predicted by first-principles calculations, for the case of localized $4f$ electrons while the lower line assumes $4f$ delocalization.

A similar case was reported in $Ce_{75}Al_{25}$ metallic glass [32]. *In-situ* high pressure synchrotron x-ray absorption spectroscopy and diffraction techniques were used to observe the origin of the pressure-induced polyamorphism from a low-density amorphous state to high-density amorphous state. They observed the Ce $4f$ electrons transform from their ambient condition localized state to an itinerant state at high pressure. There is an associated volume collapse of about 8.6 %, coinciding with the electronic $4f$ delocalization.

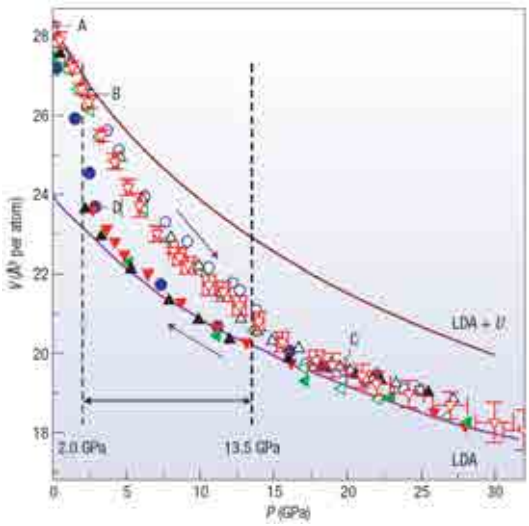

Figure 2.2: Specific volume versus pressure for amorphous $Ce_{55}Al_{45}$ [9]. Open symbols are for compression and the solid symbols are for decompression.

Crystalline Ce exhibits a polymorphic transition originated by the $4f$ electrons strong correlation [30, 31]. Experimentally, the fcc α phase of Ce transforms into a fcc γ phase when temperature is increased and the transformation is linked to a large increase in the volume. When pressure is applied at room temperature, the isostructural γ - α phase transition is observed at around 0.7 GPa pressure accompanied with a decrease in volume

of 15 %. This structural behavior has been correlated to the electronic behavior of the $4f$ electrons of Ce were pressure induced delocalization was observed. Therefore, one would expect a similar behavior for the glassy systems previously discussed.

The entanglement of structural polyamorphism with the specific electronic properties of Cerium makes the case for the recent research efforts devoted to investigate Ce-based MGs under pressure. Despite the extant evidences of structural changes and the role of $4f$ Ce electrons reported for these alloys, essential questions still remain unanswered, such as how these polyamorphism phenomena affect other material properties and to which extent the Ce-content and its peculiar electronic behavior upon application of pressure drive the polyamorphic transition, namely volume collapse, transition pressure, and other parameters. Only recently, Zeng et.al. reported a clear change in thermodynamic and electronic transport properties of $Ce_{75}Al_{25}$ as a result of the transition at 1.5 GPa [33]. The electronic delocalization may be anticipated to certainly affect Ce-based MGs mechanical properties, however, no direct observation has been achieved so far, partly due to the challenge of using traditional ultrasonic methods to reach the required high pressures. Inelastic x-ray scattering (IXS) provides a unique access to this pressure range and, coupled with high resolution X-ray diffraction (XRD), allows one to shed light on the correlations between structural and mechanical changes.

A polyamorphic phase transition upon application of pressure on a Ce-based metallic glass (MG), $Ce_{70}Al_{10}Ni_{10}Cu_{10}$, investigated by X-ray diffraction (XRD) and inelastic X-ray scattering (IXS) is reported in this work. This alloy is found to display a strong hysteresis in the volume per atom upon application and subsequent release of pressure. The observed structural changes are correlated with changes observed by IXS in the elastic constants, acoustic mode frequencies and sound speed. The results reported here point towards three different amorphous phases for this allow existing in the 0 - 25 GPa pressure region: a low and a high density states and an intermediate mixed state that displays a hysteresis behavior. Finally, we discuss the impact of Ce concentration on the polyamorphic transition for a series of Ce-based metallic glasses alloys and link it to the phase transformation between γ-Ce and α-Ce under pressure.

2.1.2 Inelastic X-ray scattering

The study of phonons dispersion using inelastic X-ray scattering (IXS) was proposed in the eighties [34] followed by the construction of the first IXS spectrometer at HASYLAB in Hamburg, Germany [35]. At present, five facilities in the world are intended to do these kind of experiments: two at the European Synchrotron Radiation Facility (ESRF) in Grenoble, France [36], two at the Advanced Photon Source (APS) in Argone, Illinois, USA [37] and one more in SPring-8, located in Harima Science Park City, Hyogo Prefecture, Japan [38].

When the energy and momentum transfer of inelastically scattered X-rays are monitored, scattering techniques can be used to resolve the electronic band structure of materials. The most common technique used for this purpose is the Inelastic Neutron Scattering (INS). However, IXS can be considered a complementing INS technique and in few cases a extending one. The experimental observable is the dynamic structure factor $S(q, E)$, where E represents the energy exchanged in the scattering process and $\mathbf{q}$ the momentum transfer. Formally, $S(q, E)$ is the space and time Fourier transform of the time dependent density-density correlation function. In fact, for energies up to some hundreds of meV the energy spectrum measured in an off-resonance x-ray scattering process is proportional to $S(q, E)$.

In an IXS experiment, a beam of photons is monochromatized and then focused onto the sample. The radiation scattered is collected and analyzed in energy by a spectrometer at a given angle. The energy $\hbar\omega = \hbar\omega_i - \hbar\omega_f$ and momentum $\hbar q = \hbar\mathbf{k}_i - \hbar\mathbf{k}_f$ exchanged of the scattered photons are characteristic of the spectrum of the excitations. Here, $\hbar\omega$ is the energy and $\hbar\mathbf{k}$ corresponds to the momentum. The i and f subscripts are for the initial and final states, respectively.

The double differential scattering cross-section $\partial^2\sigma/\partial\omega\partial\Omega$ is proportional to the number of incident probe particles scattered within an energy range ΔE and momentum variation into a solid angle $\Delta\Omega$. This differential cross-section per unit of frequency ω and unit solid angle Ω, is determined by a perturbation treatment of the electron-photon interaction Hamiltonian. The Hamiltonian describing the process by neglecting reso-

nance and the much weaker magnetic couplings, with photons in the ∼10 keV range, considering energies in the range of the acoustic photon energies <100 meV, is reduced to the Thomson interaction term:

$$H_{int} = \frac{1}{2} r_0 \sum_j \mathbf{A}^2(r_j, t) \tag{2.1}$$

where $r_0 = e^2/m_e c^2$ is the classical electron radius, m_e is the electron mass, e is the electron charge and $\mathbf{A}(r_j, t)$ is the electromagnetic field vector potential in the r_j coordinate of the jth electron. The sum extends over all the electrons in the system.

Using first-order perturbation theory (the Fermi golden rule) and the adiabatic approximation (the factorization of the electronic and nuclear eigenstates), one gets:

$$\frac{\partial^2 \sigma}{\partial \omega \partial \Omega} = r_0^2 (\epsilon_i \cdot \epsilon_f)^2 \frac{k_i}{k_f} \sum_{l_n, F_n} P_{I_n} |\langle F_n| \sum_j f_j(q) \mathrm{e}^{iq \cdot R_j} |I_n\rangle|^2 \delta(\omega - \omega_f - \omega_i). \tag{2.2}$$

The sum over the initial and final nuclear states, $\langle F_n|$ and $|I_n\rangle$, is the thermodynamic average, and P_{I_n} corresponds to the thermal population of the initial state. $f_j(\mathbf{q})$ is the form factor of the particle j and $\mathbf{R}_j$ its position vector. This expression contains the dynamical structure factor. The form factor is the space Fourier transform of the electron-density distribution. For a monoatomic system, with N atoms, $f_j(\mathbf{q}) = f(q)$ independently of the jth atom, and the expression can be simplified by the factorization of the form factor:

$$S(q, E) = \frac{1}{N} \sum_{l_n, F_n} P_{I_n} |\langle F_n| \sum_j \mathrm{e}^{iq \cdot R_j} |I_n\rangle|^2 \delta(\omega - \omega_f - \omega_i) \tag{2.3}$$

or

$$S(q, E) = |f(\mathbf{q})|^2 \frac{1}{2\pi} \frac{1}{N} \int dt \, e^{iEt/\hbar} \sum_{jl} \langle \mathrm{e}^{i\mathbf{q} \cdot R_l(t)} \mathrm{e}^{-i\mathbf{q} \cdot R_j(0)} \rangle. \tag{2.4}$$

The brackets indicate the thermal average. In this representation, $S(q, E)$ is the space and time Fourier transform of the pair correlation function $G(R, t)$, which gives the probability to find two different particles at positions $R_j(0)$ and $R_l(t)$, separated by

a distance r at time t. Finally, the double differential cross-section can be written as:

$$\frac{\partial^2\sigma}{\partial\omega\partial\Omega} = Nr_0^2(\epsilon_i \cdot \epsilon_f)^2 \frac{k_i}{k_f}|f(\mathbf{q})|^2 S(q,E). \tag{2.5}$$

The cross-section derived in this way, is valid for monoatomic systems. However, the equation can be generalized to molecular or crystalline systems by substituting the atomic form factor for the molecular or the elementary cell forms factors, respectively. For a multicomponent and disordered system, the factorization of the form factor is still possible by assuming some distribution among the different atoms. If such distribution is completely random, in the limit case, an incoherent contribution appears in the X-ray scattering cross-section. The functional form of the structure factor depends on whether the system is crystalline or amorphous.

For amorphous systems it is necessary to extend the microscopic hydrodynamic theory in order to take into account that the wavelength of the probing particle approaches interatomic distances a and to include relaxation processes with characteristic relaxation times τ. One method to derive the generalized hydrodynamic theory is using memory functions.

By using the generalized Langevin equation, it is possible to derive an expression for $S(q,E)$ based on the density-fluctuation correlation function $F(q,t) = \langle \delta\rho_{\overline{q}}(t)\delta\rho^*_{\overline{q}}(0)\rangle$:

$$\ddot{F}(q,t) + \omega_0^2 F(q,t) + \int_t^0 m(q,t-t')\dot{F}(q,t')dt' = 0 \tag{2.6}$$

where $S(q)$ is the static structure factor and $m(q,t)$ is the memory function.

The first two sum rules for $S(q,t)$ are satisfied as follows:

$$\int d\omega\, S(q,\omega) = F(q,t=0) = S(q) \tag{2.7}$$

$$\int d\omega\, \omega^2 S(q,\omega) = -\ddot{F}(q,t=0) = \frac{\kappa_B T}{M} q^2. \tag{2.8}$$

The classical thermal speed v_0 defined in terms of the atomic mass M and the tem-

perature T is then introduced in the second sum rule:

$$v_0 = \frac{\kappa_B T}{M} \tag{2.9}$$

By Fourier transformation of equation 2.6, it is possible to obtain a formal expression for $S(q, E)$:

$$S(q,\omega) = \frac{1}{\pi} S(q) \frac{\omega_0^2 m'(q,\omega)}{[\omega - \omega_0^2 + \omega m''(q,\omega)]^2 + [\omega m'(q,\omega)]^2} \tag{2.10}$$

where $m'(q,\omega)$ and $m''(q,\omega)$ are the real and imaginary parts of the time Fourier transform of the memory function. Different models are used to calculate the memory function. For the case of glassy samples, where $\omega\tau \gg 1$ and $qa \leqslant 1$, one enters in the molecular hydrodynamics region. Here, the atomic dynamics is influenced by structural and relaxational effects. In this limit, the memory function is considered as the sum of two contributions. The first one is related to the atomic vibrations in the local atomic environment, which induces a very fast decay usually on the 10^{-13}s time scale and it is called the microscopic or instantaneous decay. The second one corresponds to the structural relaxation and it is represented by a delta function. This process describes the relaxation of the intensity fluctuations at longer times characterized by τ and it is usually temperature dependent. In our case of study of undercooled liquids, the minimal expression for the memory function is approximated by:

$$m(q,t) = 2\Gamma(q)\delta(t) + \Delta^2(q), \tag{2.11}$$

$\Gamma(q)$ represents the instantaneous contribution and $\Delta^2(q)$ is the relaxation strength which is related to the q dependent generalizations of the usual limiting frequency and adiabatic sound speeds, $c_\infty(q)$ and $c_0(q)$:

$$\Delta^2(q) = c_\infty^2(q) - c_0^2(q) \tag{2.12}$$

This term describes the classical phenomenology of the dispersion and absorption of the sound waves. For example, the transition of the sound speed from its low frequency, adiabatic value, $c_0(q)$, to the high frequency, limiting value $c_\infty(q)$. Finally, the dynamic

structure factor reduces to

$$S(q,\omega) = S(q)\left[f_q\delta(\omega) + (1-f_q)\frac{1}{\pi}\frac{\Omega^2(q)\Gamma(q)}{(\omega^2-\Omega^2(q))^2+\omega^2\Gamma^2(q)}\right], \tag{2.13}$$

where

$$\Omega(q) = qc_\infty(q)fq = 1-\omega_0^2(q)/\omega_\infty^2(q). \tag{2.14}$$

f_q is known as the non-ergodicity factor or the Debye-Waller parameter. The equation 2.13 is the sum of an elastic line (the relaxation process) and an inelastic feature which is formally identical to a damped harmonic oscillator (DHO) function. The central line accounts for a fraction f_q of the total intensity. It is important to notice that the derivation presented is only a generalization of the formalism at low q, and it does not take into account the contribution of transverse excitations which appear at higher q values. (For this text refer [39] to [40]).

2.2 Methodology

In-situ high-pressure synchrotron experiments where performed in a $Ce_{70}Al_{10}Ni_{10}Cu_{10}$ metallic glass to obtain information on structural and high frequency dynamical changes. In particular, X-ray diffraction data allow us to identify different density changes under pressure (mainly an increase). While inelastic x-ray scattering measures are focused on changes in the phonon dispersion relations and sound velocities. All experiments were conducted at room temperature on the same batch of ribbons, thus ensuring the reliability and allowing for a direct comparison of structural and mechanical properties. The particular experimental conditions for the different measurements are presented below.

2.2.1 Material

The samples for both XRD and IXS experiments stemmed from melt spun ribbons obtained from a 4 mm diameter bar of $Ce_{70}Al_{10}Ni_{10}Cu_{10}$ produced by mold cast. Ribbons of 30 to 50 μm and $\sim$3 mm wide were prepared using the melt-spinning technique in a controlled argon atmosphere. The spinning speed of the copper wheel was 40 m/s. The resulting ribbons were cut in small pieces of few micrometers in order to mount them into diamond anvil cells (DAC).

2.2.2 *In-situ* synchrotron high-pressure X-ray diffraction

The X-ray diffraction (XRD) experiments were conducted in beam-line ID27 at the European Synchrotron Radiation Facility (ESRF). Incident energy of 33 keV was focused on the sample by using the highly focalized micrometric sized X-ray beam available at ID27 (3×2 μm^2). A small piece of about 60 micron diameter and 30-50 μm was cut from the melt spun ribbons of amorphous $Ce_{70}Al_{10}Ni_{10}Cu_{10}$. This sample was loaded into a diamond anvil cell (DAC) together with ruby pieces to calibrate and measure pressure using the ruby fluorescence levels [41, 42]. Liquid Helium was loaded in the DAC as pressure transmitting medium by means of a *LTC07-250um-STST*-He loading machine. XRD patterns were acquired in the 0–25 GPa pressure range upon both compression and decompression ramps in transmission mode through the diamonds. In the proximity of

the sample, a diffraction pattern of the DAC solely was recorded at each pressure point. These spectra were used as background and subtracted to the sample signals after intensity normalization. Diffraction patterns were recorded as 2-D images on the image plate and then integrated using the *FIT2D* program [43].

Additional XRD data up to 22 GPa were acquired during the Inelastic X-ray Scattering experiment at the same IXS and additional pressure points. The methodology followed in this case is explained in the next section.

2.2.3 Inelastic x-ray scattering

The IXS experiment was performed in beamline ID28 at the ESRF. The instrument was operated using the Si 999 Bragg reflection of the main monochromator, with an incident energy of 17.794 keV. This configuration yields a momentum transfer resolution of 0.27 nm^{-1} and energy transfer resolution of 3 meV. Beam-line ID28 also has coupled a $S(Q)$ detector. During the IXS experiment, XRD data were obtained at the same pressure points and additional ones. IXS energy scans were performed in the range of -25 to 25 meV with an energy step of 0.5 meV for momentum transfers between 2 and 12 nm^{-1}. Spectra corresponding to eight different momentum transfers were recorded simultaneously using a multi-analizer setup. The corresponding angles and momentum transfer evaluated are presented in Table 2.1. It is important to note that Detector 4 was not working during the experiment and Detector 3 deflected some signals towards other detectors, mainly Detector 1.

In order to optimize the IXS signal, 30–50 μm thick ribbons were selected and two samples of 170×150 and 95×95 μm^2 were cut and mounted on DACs, as shown in Figure 2.3. Liquid Neon and Helium were loaded in the DACs together with the first and second samples, respectively, as pressure transmitting mediums. All experiments were performed at room temperature. Pressure was measured using the ruby fluorescence method and ruby pieces were loaded together with the sample for this purpose. The image of the mounted sample was taken using an optical microscope. The square sample is in the middle of the rounded hole of the steel gasket. The black dot, located to the left of the

Table 2.1: Positions of detectors used for the Si (9 9 9) configuration.

Detector	Angle	Q (nm^{-1})
1	1.27	2
6	2.01	3.16
2	2.79	4.39
7	3.54	5.57
3	4.32	6.8
8	5.06	7.96
9	6.57	10.33
5	7.36	11.58

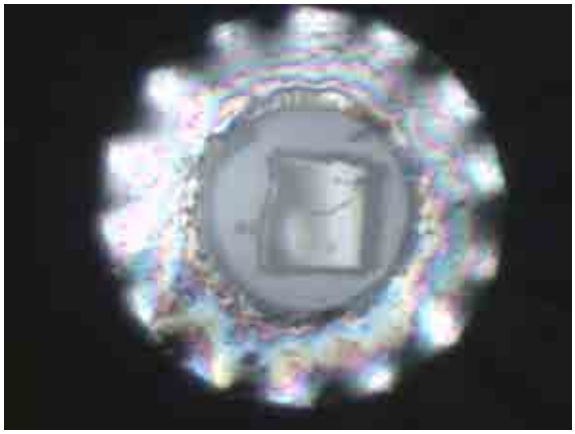

Figure 2.3: Image of the Sample-2 mounted on a DAC.

sample, corresponds to the ruby used for pressure measurements. The dimensions of the two samples and the elements used as pressure transmitting mediums are listed below.

Sample-1

Sample dimensions	170 x 150 x ∼50 micrometers
Hole diameter	∼300 micrometers
Beam size	150 x 150 micrometers
Pressure transmitting medium	Neon

Sample-2	
Sample dimensions	95 x 95 x ∼25 micrometers
Hole diameter	180 micrometers
Beam size	100 x 100 micrometers
Pressure transmitting medium	Helium

The DAC used for Sample-1 was filled with Neon. Due to the sample size, it could be possible that the diamonds compress directly on the sample getting away of the desired hydrostatic pressure. Neon seems to be a good option to avoid an uniaxial compression because is less compressible than Helium. Sample-1 was used to obtain data up to 12.5 GPa, pressure at which the DAC failed. Sample-2 was employed to obtain the highest pressure data and the data upon decompression. Sample-2 was loaded with Helium and then pressurized to 5GPa. A $S(Q)$ scan was performed at these conditions in order to ensure reliability. IXS and XRD experiments were conducted on the same batch of ribbons. Both data sets display a similar behavior at low pressure, which ensure the reliability and the hydrostatic conditions obtained with both pressure transmitting media. Additional XRD data were acquired during the IXS experiment, in agreement with those taken at ID27.

2.3 Results

The XRD results display a different behavior upon application of pressure and decompression. In particular, it shows a hysteresis cycle with respect to pressure and volume per atom, similar to that reported on a $Ce_{55}Al_{45}$ metallic glass [9]. The IXS results show rather small change in the acoustic sound velocity related to the hysteresis cycle, and a significant change in acoustic frequencies at half the wavenumber corresponding to the first band in the static structure factor. Both signatures are compatible with the polyamorphic transition.

2.3.1 Structural properties

Figure 2.4 shows integrated XRD patterns obtained in beamline ID27 in the 0 to 25 GPa pressure range, upon both compression and decompression. The lower panels display intensity plots to highlight the spectral weight redistribution in momentum transfer as a function of pressure. The samples remain amorphous in the whole pressure range, showing no signs of crystallization. A main peak is observed at 22.6 nm^{-1}, followed by broader features at 38.2 and 55.2 nm^{-1}. Upon compression, the main peak shifts to higher momentum transfer, displaying a distinct behavior at the lowest pressures: Below nearly 3 GPa, the peak shift occurs faster than at higher pressures, thus indicating the possible onset of the first amorphous–amorphous transformation. This shift is accompanied with a redistribution of the spectral weight corresponding to the second diffraction peak: it broadens and at pressures larger than 2 GPa a satellite structure appears at 50 nm^{-1}. This redistribution is more apparent in the lower panels. At higher pressure, the satellite also shifts to higher Q values with increasing pressure, and both features decrease in relative intensity with respect to the main peak.

Upon decompression, the same change in the intensity distribution is apparent at pressures lower than 4 GPa, and a sudden shift to lower momentum transfer of the main peak is observed below 2 GPa. The XRD patterns thus seem to reveal 3 distinct density regions, corresponding to the 0–2 GPa, 2–10 GPa and higher pressure ranges, pointing to the presence of phase transformations between amorphous structures for

$Ce_{70}Al_{10}Ni_{10}Cu_{10}$. The approximate values where the transition occurs are more evident when the volume change is plotted as seen in the inset of Fig. 2.5.

Table 2.2: Values of Q_{max} and the relative volume as function of pressure obtained from the structure factors during compression

P (GPa)	P_{error} (GPa)	Q_{max} (nm^{-1})	V_P/V_0
0.24	0.00	22.604	1.000
1.29	0.03	22.960	0.954
2.65	0.11	23.714	0.866
4.12	0.18	24.158	0.819
6.21	0.12	24.562	0.779
7.58	0.31	24.750	0.762
10.03	0.11	25.054	0.734
11.36	0.12	25.206	0.721
12.40	0.24	25.301	0.713
13.97	0.16	25.470	0.699
16.61	0.05	25.715	0.679
17.92	0.17	25.802	0.672
20.14	0.21	25.959	0.660
21.89	0.16	26.084	0.651
23.34	0.14	26.198	0.642
24.52	0.06	26.302	0.635
25.22	0.05	26.361	0.631

Figure 2.5 displays the specific volume as a function of pressure for both compression and decompression processes. The volume ratio was determined using the values of the momentum transfer at the main diffraction peak observed in Fig. 2.4 and the specific volume estimated for the $Ce_{70}Al_{10}Ni_{10}Cu_{10}$ alloy at ambient pressure and temperature. Solid and open symbols correspond to data obtained during compression and decompression, respectively.

Upon application of pressure, two distinct regimes are clearly observed: The upper black dashed line at low pressure displays the equation of state (EOS) calculated from results up to 0.5GPa reported by B. Zhang et al. [44], thus showing a reasonable agreement with our low pressure data. Specific volume decreases faster between 0 to 4 GPa

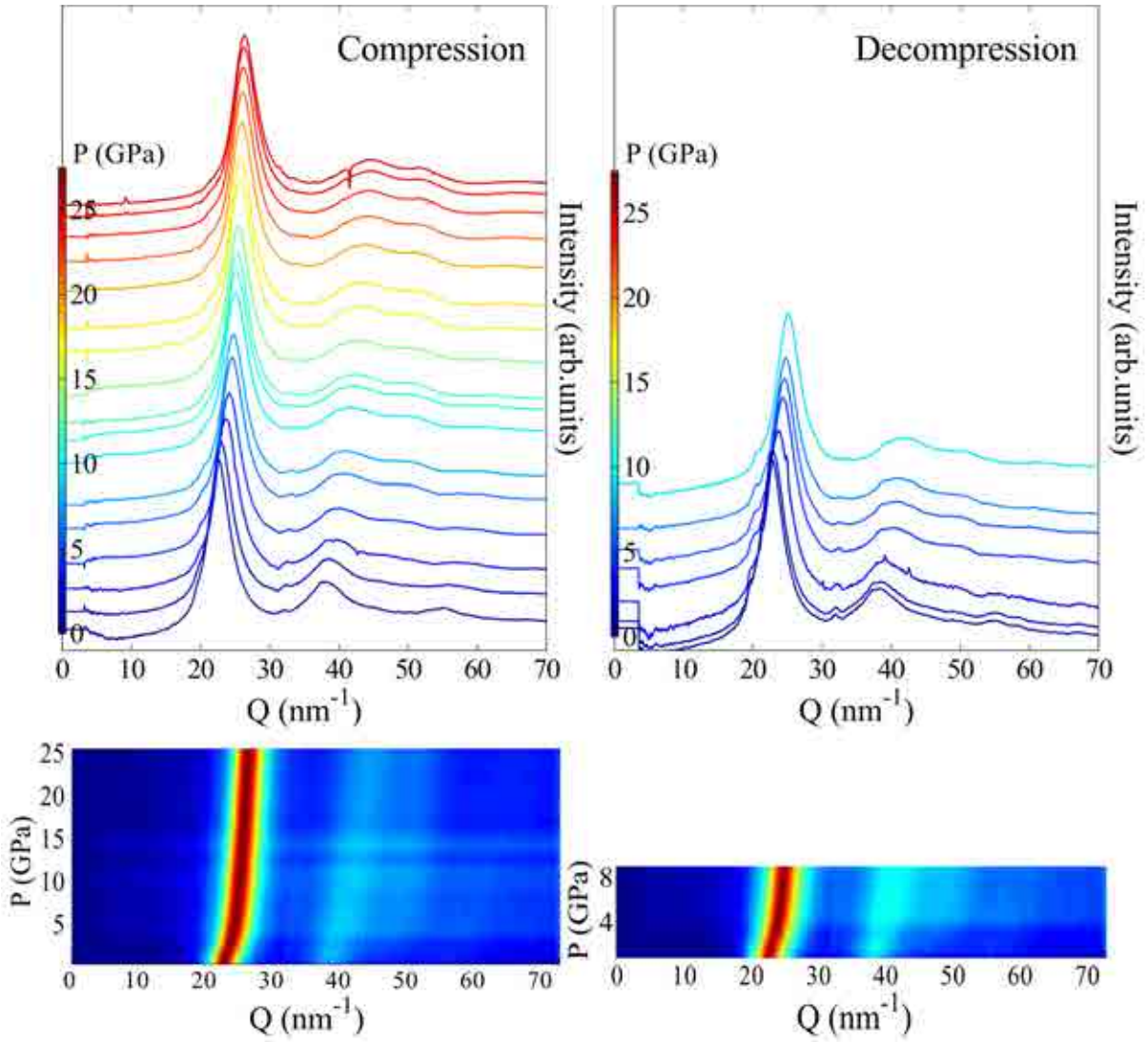

Figure 2.4: XRD integrated intensity patterns of $Ce_{70}Al_{10}Ni_{10}Cu_{10}$ metallic glass obtained during compression and decompression. The lower panels display the intensity plot normalized to the intensity of the main diffraction peak, in order to highlight the spectral weight redistribution.

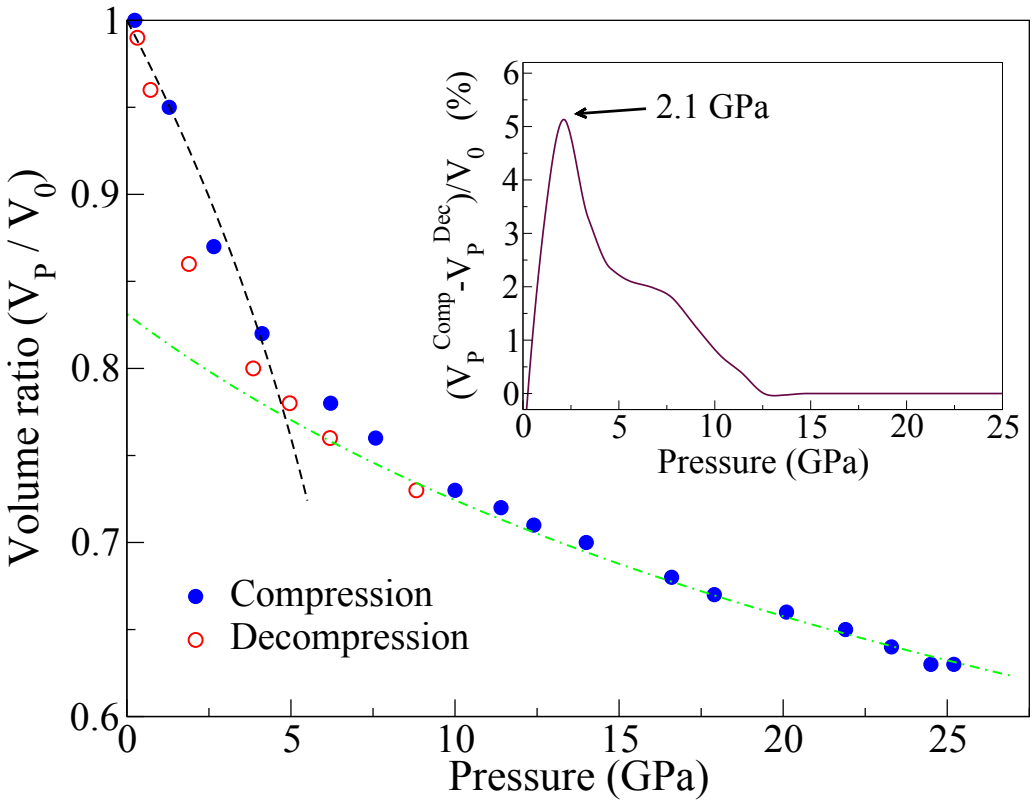

Figure 2.5: Relative specific volume versus pressure. Solid and open symbols correspond to data taken during compression and decompression, respectively. Dashed lines represent estimated EOS drawn as guides-to-the-eyes to highlight the low (black) and high (green) density states observed at ambient and high pressure, respectively. The EOS corresponding to the low density state, upper black dashed line, was obtained from data up to 0.5 GPa reported in Ref. [44]. The inset shows the pressure dependence of the hysteresis by displaying the difference in volume ratio upon compression and decompression as a function of pressure.

Table 2.3: Values of Q_{max} and the relative volume as function of pressure obtained from the structure factors during decompression

P (GPa)	P_{error} (GPa)	Q_{max} (nm^{-1})	V_P/V_0
8.82	0.14	25.119	0.729
6.19	0.01	24.783	0.759
4.96	0.01	24.587	0.777
3.85	0.01	24.374	0.798
1.89	0.01	23.736	0.864
0.72	0.00	22.895	0.962
0.32	0.03	22.699	0.988

in agreement with the shift in the main peak of the structure factor evidenced in Fig. 2.4. At pressures larger than 10 GPa, the specific volume displays a pressure dependence that can be fitted to a general Murnaghan [45] type EOS (lower green dashed line). The latter fit was actually performed taking into account only pressure points above 15 GPa. These two regimes represent, hence, the low and high density states.

Between 4 and 10 GPa, the specific volume displays a non-linear pressure dependence. Note the different convexity displayed by both EOS, which point out to either an anomalous pressure dependence of the specific volume or to the existence of a third region where the convexity gradually changes. The latter might be the underlying reason for the hysteresis evidenced between compression and decompression processes. In order to ascertain more clearly the pressure range of this mixed density region, in the inset of Fig. 2.5 the change in specific volume between compression and decompression, as function of pressure, was plotted. To obtain this figure, polynomial interpolation curves of both up-load and down-load specific volume data sets were subtracted. The data set for decompression was completed with those pressure points taken at pressures higher than 15 GPa, i.e. the high pressure limit. This inset shows a peak change in volume ratio at nearly 2 GPa, with a maximum difference in volume ratio of nearly 5.5%, followed with a decrease in hysteresis up to 12 GPa. Despite the wiggles due to the reduced number of data points, an abrupt change in hysteresis is observed at 2 GPa, which make us assign this pressure value to the onset of the intermediate density region.

Hence, these results suggest that the $Ce_{70}Al_{10}Ni_{10}Cu_{10}$ metallic glass exhibits three different amorphous regions upon application of pressure. A low-density state is observed at ambient conditions, which becomes a higher-density state while increasing pressure, with an intermediate region that shows a gradual transition linking both density states and displays hysteresis through compression and decompression stages. Between both density states there is a volume collapse of $\sim$16% extrapolated at ambient pressure. This hysteresis cycle and large volume collapse are in agreement with previous works [9, 30, 46], where the transition was assigned to be carried out by means of pressure induced delocalizaton of Ce $4f$ electrons. A similar behavior was reported for $Ce_{75}Al_{25}$ MG, where an 8.6% volume collapse was observed at the same pressure as a transformation of Ce $4f$ electrons from a localized state at ambient pressure to an itinerant state at high pressure [32]. The origin of this polyamorphism can be attributed to a similar electronic transformation observed in crystalline Cerium accompanying a phase transformation between γ-Ce and α-Ce, at 0.9 GPa [30, 31]. We will resume this point later in the discussion.

2.3.2 Mechanical properties

Given the large electron-phonon coupling in Ce and the substantial amount of this element in the alloy [47, 48], changes in the electronic band structure should be followed by changes in the phonon dispersion relations and sound velocities.

High pressure IXS experiments were performed to unveil the effect of the polyamorphic transition on the mechanical properties of Ce-based alloys at a microscopic level. In order to cover the full pressure range up to a complete transition, IXS spectra were acquired from 0 to 22 GPa upon increase of pressure, and then at 10 GPa upon pressure decrease. Unfortunately, the beam time allocated limited the acquisitions upon release of pressure. This pressure point revealed a minor hysteresis effect as well on the mechanical properties and the acoustic frequencies, as it will be shown later in this chapter.

Figures 2.6 and 2.7 display representative IXS spectra for the eight values of the momentum transfer obtained simultaneously at 0 and 21.9 GPa, respectively, upon increase of pressure. For a complete overview on the experimental spectra and analysis at the different pressure points, please refer to Appendix A.

The spectra consist in a central elastic peak at zero energy transfer followed by additional peaks at positive and negative energies that correspond to longitudinal acoustic excitations of $Ce_{70}Al_{10}Ni_{10}Cu_{10}$ metallic glass. The elastic peak has been truncated in order to enhance the features corresponding to the acoustic waves.

The IXS spectra is proportional to the dynamic structure factor, $S(Q, w)$, and can be fitted using as model function a damped harmonic oscillator (DHO) for each excitation and a delta function for the elastic line, convoluted both with the experimental resolution function [49]

$$S\left(Q,\omega\right) = S\left(Q\right)\left[A(Q)\delta(\omega) + \frac{1-A(Q)}{\pi} \times \frac{\Omega^2(Q)\Gamma(Q)}{\left[\omega^2 - \Omega^2(Q)\right]^2 + \omega^2\Gamma^2(Q)}\right] \tag{2.15}$$

where, at a given momentum transfer Q, $S(Q)$ is the static structure factor measured using standard x-ray diffraction, $A(Q)$ is the intensity of the elastic scattering relative to the spectrum total intensity, $\Omega(Q)$ is the characteristic frequency of the acoustic mode and corresponds to the maximum of the longitudinal current spectra $C_L(Q,\omega) = (\omega/Q)^2 S(Q,\omega)$, and $\Gamma(Q)$, denoted as phonon damping, is a parameter related to the sound attenuation and the full-width-at-half-maximum (FWHM) of the excitation signal [49]. Dashed lines represent the elastic (green) and inelastic (blue) contributions derived from the model after convolution to the experimental instrumental function, which is analyzer-dependent. At the lowest momentum transfer, a transverse acoustic phonon of diamond from the anvil cell appears and is marked with a red asterisk. Due to the higher sound speed of this mode, 11 km/s, it goes out of the region-of-interest with increasing momentum transfer.

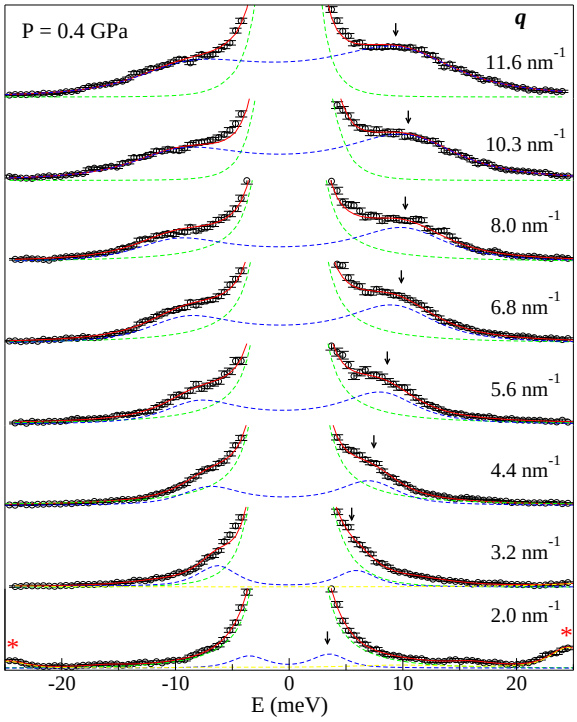

Figure 2.6: IXS spectra of the $Ce_{70}Al_{10}Ni_{10}Cu_{10}$ metallic glass for $P = 0.39$ GPa and Q between 2 and 12 nm^{-1} under compression. Open circles correspond to experimental data and solid lines to the best fit obtained using Eq.2.15. The individual components of the excitation and elastic line are displayed with dashed lines.

Table 2.4: Data obtained from the IXS spectra at 0.39 GPa under compression. The error bars are given in parentheses.

Detector #	θ (deg)	q (nm^{-1})	E (meV)	Γ (meV)	A_{In}	A_{Ph}
1	1.27	2	3.27(22)	0.9(1)	21049.7	1408.5
6	2.01	3.2	5.50(2)	1.6(9)	32910.1	1880.3
2	2.79	4.4	7.50(10)	3.2(3)	27453.6	4352.0
7	3.54	5.6	8.89(11)	5.3(3)	11840.1	2826.3
3	4.32	6.8	10.30(8)	7.0(2)	21787.1	7114.5
8	5.06	8	11.21(9)	7.5(3)	15112.0	4763.8
9	6.57	10.3	11.32(9)	8.2(3)		
5	7.36	11.6	11.63(7)	11.0(3)	25546.1	14774.4

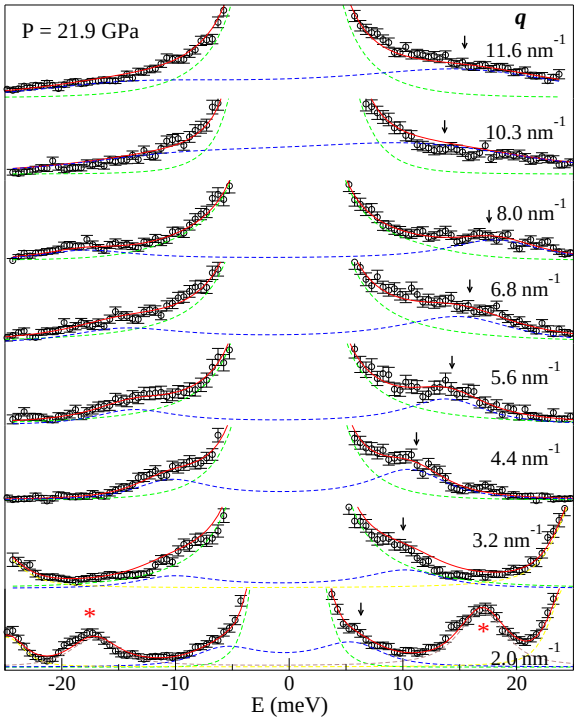

Figure 2.7: IXS spectra of the $Ce_{70}Al_{10}Ni_{10}Cu_{10}$ metallic glass for $P = 21.87$ GPa and Q between 2 and 12 nm^{-1} under compression. Open circles correspond to experimental data and solid lines to the best fit obtained using Eq.2.15. The individual components of the excitation and elastic line are displayed with dashed lines.

Table 2.5: Data obtained from the IXS spectra at 21.87 GPa under compression. The error bars are given in parentheses.

Detector #	θ (deg)	q (nm^{-1})	E (meV)	Γ (meV)	A_{In}	A_{Ph}
1	1.27	2	6.40(27)	4.1(8)	6262.6	957.4
6	2.01	3.2	10.51(-)	0.1(-)		
2	2.79	4.4	11.21(25)	5.1(11)	10397.2	1375.3
7	3.54	5.6	14.32(33)	5.2(13)	5930.8	474.1
3	4.32	6.8	15.63(45)	12.6(11)	10491.0	1497.0
8	5.06	8	18.76(41)	7.2(12)	9580.6	592.5
9	6.57	10.3	19.56(58)	11.1(-)		
5	7.36	11.6	19.91(68)	20.8(23)	18243.1	2675.5

In Figs. 2.6, 2.7 and 2.8 open circles correspond to experimental data and solid lines to the best fit obtained using Eq.2.15. The individual components of the excitation and elastic line are displayed with dashed lines.

Note that the quality fitting is diminished for $q = 3.2nm^{-1}$ and $q = 10.3nm^{-1}$. At these momentum transfers, the resolution functions are not able to describe properly the tails of the elastic peak. Due to this fact, these momentum transfers are not further considered in the analysis. For more details refer to Appendix A. Additionally, it is possible to notice that the spectra correspond to momentum transfers spaced by 1.2 nm^{-1}, with the exception of the gap between 8 and 10.3 nm^{-1}. This gap results from the ill-functioning of the analyzer set at $q = 9.2nm^{-1}$, as mentioned in the Methodology section.

The broadening of acoustic excitations with increasing momentum transfer indicates an increase in the sound attenuation, up to a point where the broadening becomes so large that it is no longer valid the term of propagating excitations to refer the modes [50].

The energy of these acoustic-like excitations has a typical behavior of acoustic modes: it firstly increases with the increasing momentum transfer at low Q values and then starts to decrease when the highest Q values are reached, as displayed by the arrows in Figs. 2.6 and 2.7. The excitation intensity increases as well with Q, due to both the increase of broadening and the energy.

Figure 2.8 shows selected IXS spectra corresponding to a momentum transfer of 6.8 nm^{-1} upon compression up to 22 GPa, and at 10.2 GPa in decompression. A blue-shift of the excitation energy occurs with increasing pressure. This corresponds to a stiffening of the amorphous medium upon application of pressure, similarly to what is observed in their crystalline counterpart. The energy of the excitations increases while increasing pressure following an almost linear relation. On the other hand, the intensity decreases when higher pressure is applied, which might be attributed to changes in the pressure transmitting medium. The reduced intensity makes more challenging the fit procedure of the excitation energies, which therefore display a larger error bar.

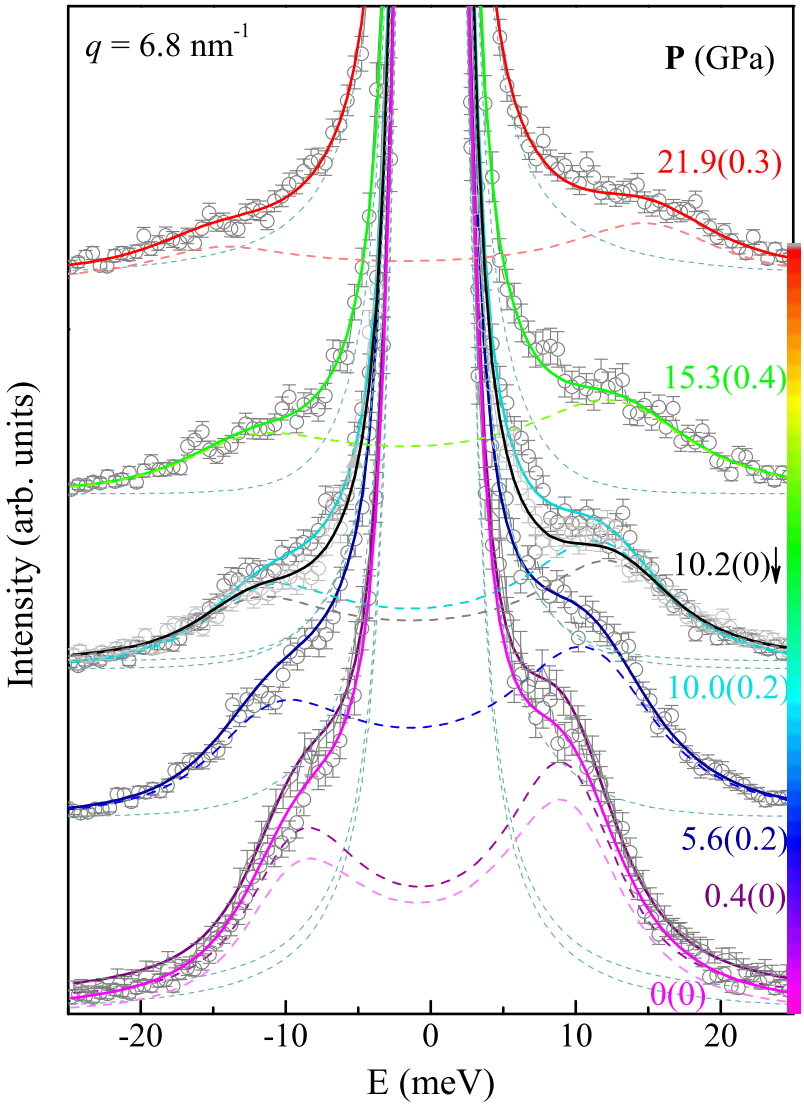

Figure 2.8: Selected IXS spectra of the $Ce_{70}Al_{10}Ni_{10}Cu_{10}$ metallic glass for $q = 6.8$ nm^{-1} and pressures up to 22 GPa. Open circles correspond to experimental data and solid lines to the best fit obtained using a DHO model of Eq.2.15. The individual components of the excitation and elastic line are displayed with dashed lines.

A close-up on the IXS curves during compression and decompression at $Q = 6.8$ nm^{-1} is presented in Fig. 2.9. The lower intensity of the excitation during decompression suggests an hysteresis effect on the mechanical properties of the $Ce_{70}Al_{10}Ni_{10}Cu_{10}$ metallic glass going upwards and downwards the structural polyamorphic transition. This hysteresis is further emphasized by the 0.5 meV energy increase observed at the excitation energy from compression to decompression. At lower momentum transfers, the IXS spectra taken during the pressure increase and decrease processes almost retrace on each other and the energy shift becomes negligible. At 11.6 nm^{-1}, however, the energy shift becomes more than double, thus evidencing that the hysteresis in structural properties also create an hysteresis in the mechanical properties.

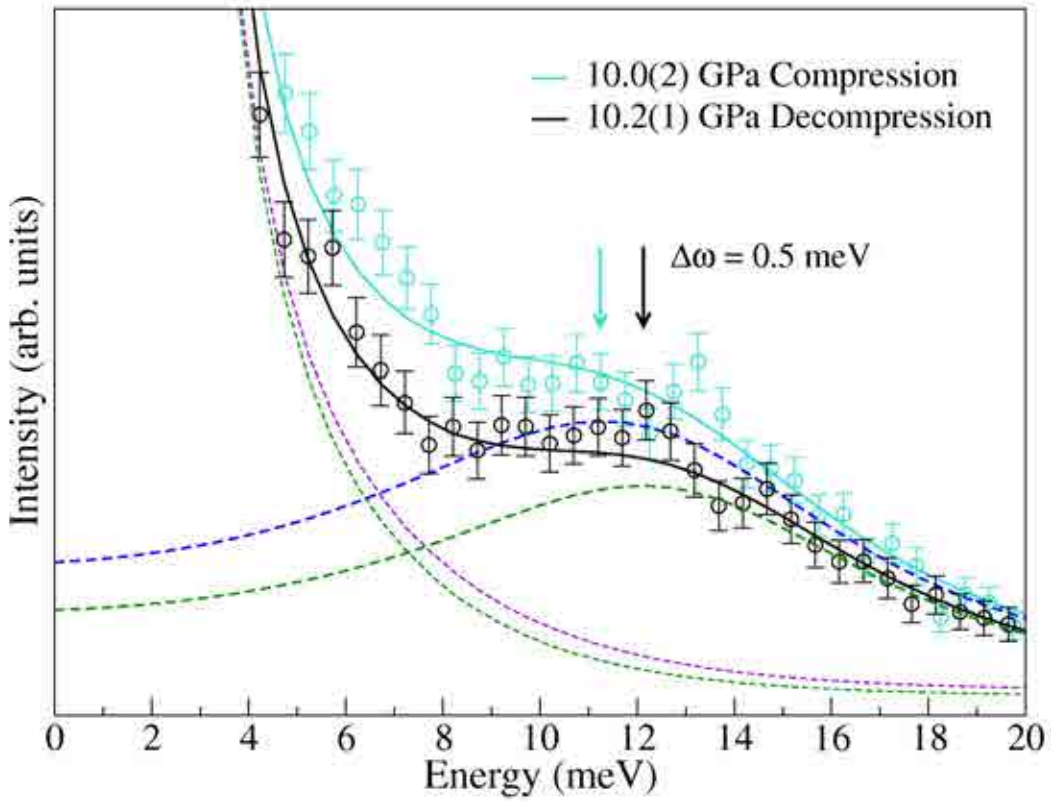

Figure 2.9: Example of the different behavior of the IXS intensity band shift during compression and decompression at around 10 GPa and 6.8 nm^{-1}.

Similarly to what happens in single crystals, at a given pressure, the dependence of the acoustic excitation energy on momentum transfer can be plotted in a diagram and follows a dispersing curve, the so-called longitudinal acoustic dispersion relation for the amorphous material. The dispersion relation has an almost linear dependence on Q when Q tends to zero and its slope at this limit corresponds to the macroscopic longitudinal sound velocity [39]. Figure 2.10 displays such dispersion curves obtained at different pressures from the excitation energies shown in the previous figures.

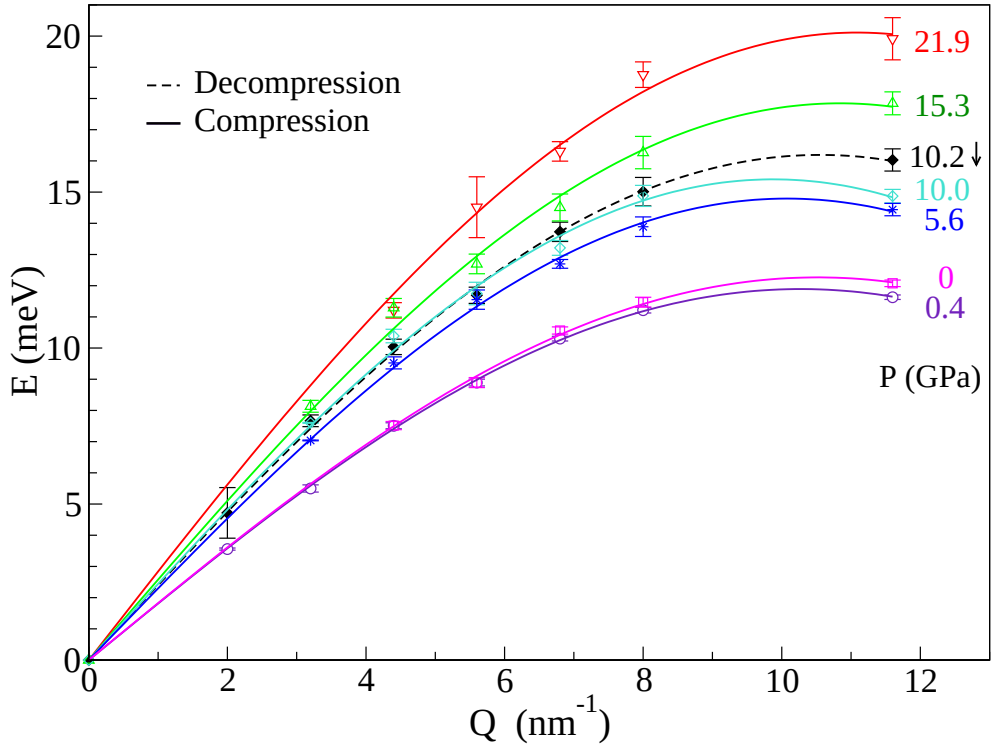

Figure 2.10: Dispersion relation of the inelastic excitations obtained from a damped harmonic oscillator model.

The dispersion curves behave like a typical sinusoidal function that peaks at momentum transfers between 10 and 12 nm^{-1}, depending on the applied pressure. This maximum turns out to be at the same momentum transfer Q_{max} as half that of the main peak of the static structure factor determined with XRD, which allows to understand the

amorphous material as presenting a pseudo-Brillouin zone of characteristic length equal to $2Q_{max}$. Note the different value of Q_{max} observed at 10 GPa for pressure increasing and decreasing processes. This again reflects the structural hysteresis observed in the polyamorphic transition. An anomalous behavior is observed at low pressures were a softening of the longitudinal acoustic mode upon increase of pressure between 0 and 0.4 GPa is clearly evidenced in Fig. 2.10.

The longitudinal sound velocity was obtained by extrapolating a sinusoidal fit of the dispersion relations to zero momentum transfer and taking the slope at this limit for each pressure. The calculated velocities are displayed in Fig. 2.11. By following this procedure, a longitudinal sound speed of 2.78 km/s is obtained at ambient pressure. Different symbols are used to represent data stemming from different samples upon compression and decompression. A pressure induced decrease in sound velocity of $\sim$1.4% is observed at low pressure. This decrease correlates with the softening of the mode observed in Fig. 2.10.

It is worthwhile to notice that a negative slope in the change of acoustic velocities as function of pressure is characteristic of glasses with covalent bonds. The followed behavior is in agreement with the negative change in the acoustic longitudinal velocity shown by Zhang et al. [44], where measurements up to 0.5 GPa were reported. At higher pressures, a sudden increase in sound velocity is observed between 0.4 and 5 GPa, followed by a linear rise at a smaller rate up to the highest applied pressure, of 22 GPa. This last behavior is expected from other bulk MGs [11]. Results presented in Fig. 2.11 show then the presence of a transition from a more covalent phase at low pressure to a metallic one when pressure is increased. Unfortunately, more data points would be required to reveal at which pressure the change in slope occurs and whether this change is abrupt or smooth. However, 5 GPa is a higher limit pressure value for the transition, which agrees well with the changes in the static structure factor obtained from XRD and shown in Figs. 2.4 and 2.5. The fact that the pressure dependence of the sound velocity changes twice its slope between 0 and 25 GPa point to at least three phases of distinct mechanical behaviors displayed by amorphous $Ce_{70}Al_{10}Ni_{10}Cu_{10}$, in line with the three pressure ranges of different density defined solely from analysis of the XRD data. Upon decrease of pressure, the sound velocity becomes slightly smaller than that obtained in

the upload process, thus evidencing again the non-reversible character of the polyamorphic transition.

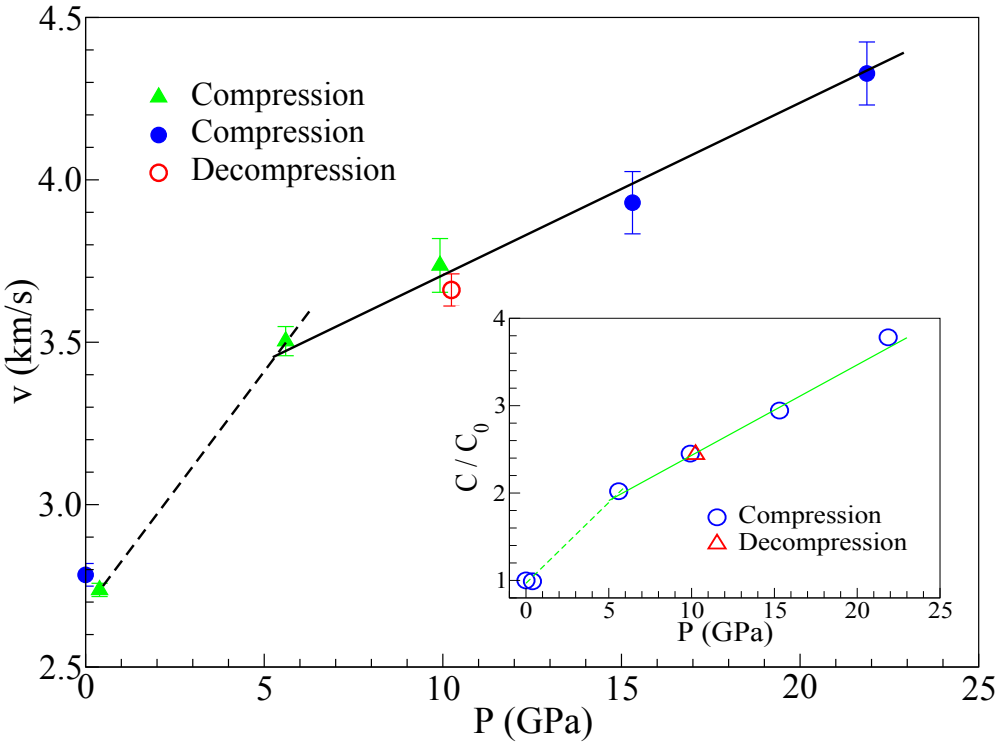

Figure 2.11: Sound velocities dependence of hydrostatic pressure. The inset displays the change with pressure of the relative longitudinal elastic constant.

The sound velocity, v, is related to the longitudinal elastic constant of $Ce_{70}Al_{10}Ni_{10}Cu_{10}$, C, by the following expression: $C = v^2\rho$, where ρ is the mass density, i.e. inversely proportional to the specific volume. The inset of Fig. 2.11 displays the combination of both static and dynamic effects of the polyamorphic transition by showing the pressure dependence of C relative to its value at ambient pressure, C_0. Two changes are again observed: A softening of C from 0 to 0.4 GPa is followed by a sudden stiffening of the elastic constant up to 5 GPa, followed then by a linear behavior up to the applied highest pressure, 22 GPa. The three regions displayed by the pressure dependence of C further strengthen the three density domains described in Section 2.3.2. Since the sound velocity decreases from compression to decompression, and the specific volume also decreases

from one to the other, a partial cancellation of both effects is to be expected for the elastic constant. In agreement with this, no hysteresis can be assigned so far to the elastic constant, within the experimental resolution, although more IXS data upon decompression would be required to make a firm statement. The extrapolation of the elastic constant of the high density state to ambient pressure reveals a stiffening of 20% with respect to the low density state, at 0 GPa, as a consequence of the polyamorphic transition.

The IXS data therefore confirm the existence of three different mechanical behaviors of amorphous $Ce_{70}Al_{10}Ni_{10}Cu_{10}$ in the 0 to 22 GPa pressure range. The negative slope of both longitudinal sound velocity and elastic constant at low pressure corresponds with a softening of the mode energies typical of glasses with covalent bonds. The intermediate pressure range thus correspond to a change from covalent-like to metallic-like bonding behavior in glasses under pressure, which then stabilizes at higher pressures. More IXS pressure points are required to establish the transition between these three regions.

2.4 Discussion

The combination of both XRD and IXS point out to a gradual non-reversible transition between a low density and a high density state. The origins of this transition can be retraced back to crystalline Cerium, which exhibits a polymorphic transition stemming from the $4f$ electrons strong correlation [30, 31]. Experimentally, the fcc α phase of Ce transforms into a fcc γ phase when temperature is increased and the transformation is linked to a large change in the volume. When pressure is applied at room temperature, the isostructural $\gamma - \alpha$ phase transition is observed at around 0.9 GPa accompanied with a decrease in volume of 15 %. This structural behavior has been linked to the electronic behavior of the $4f$ electrons of Ce and pressure induced delocalization was observed. This delocalization has been recently reported to induce strong changes in both phonon dispersions and a strong electron phonon coupling [51].

Unlike crystalline Ce, in which the transition occurs sharply, polyamorphic transitions in Ce-based metallic glasses are smooth and continuous over a pressure range and present a hysteresis cycle by decreasing pressure. It is therefore expected that changing the Ce concentration will allow for a detailed study of the interplay between electronic and lattice roles in the polyamorphic transformation.

Figure 2.12 summarizes the volume reduction estimated and the pressure range at which the transition takes place in different Ce-based alloys including also the results obtained in this work. The value of the starting pressure of the transition for the lowest Ce concentration MG is not reported in the literature. A larger pressure range is observed when Ce concentration decreases, with a saturation for the final pressure at 50% Ce atom concentration. This can be explained by considering the local environments in each alloy. Crystalline Ce owns a unique and identical structure throughout the material and the transformation occurs at the same time for all atoms. Adding foreign atoms increases the disorder in the alloy and modifies the local environment of Ce. Therefore, a change in the coordination as well as the electronic properties is also observed. In Ce-based metallic glasses, the smallest pressure range and volume collapse for the transformation occurs for $Ce_{75}Al_{25}$ metallic glass [32], which shares the stoichiometric concentration of

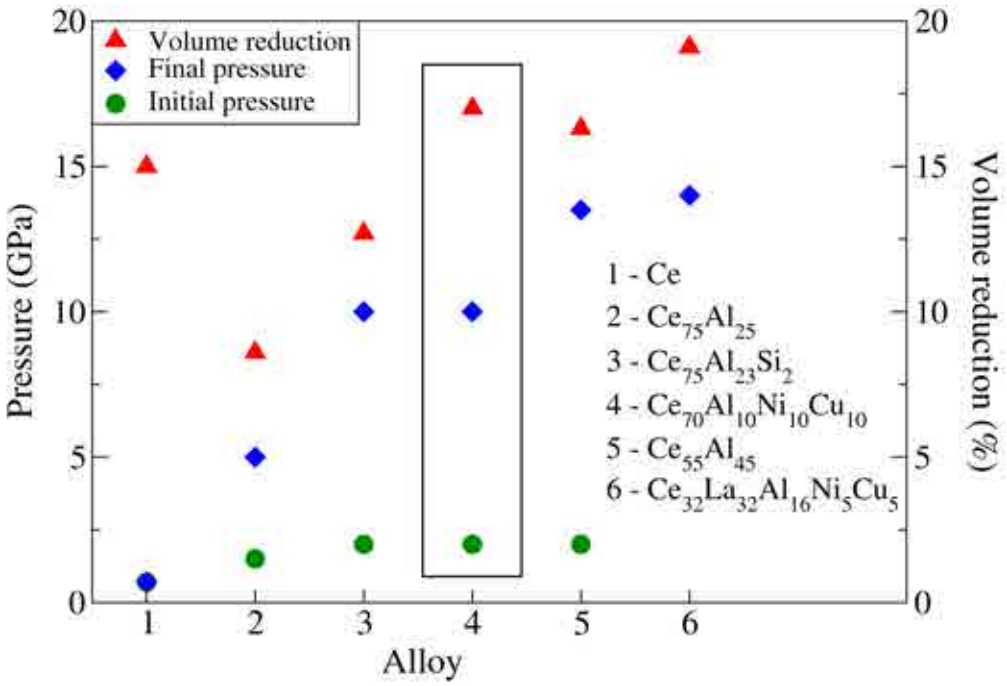

Figure 2.12: Pressure range of the polyamorphic transition and volume reduction observed in different Ce-based metallic glasses. Data were taken from Refs. [9, 32, 52], and [53] except for the $Ce_{70}Al_{10}Ni_{10}Cu_{10}$ metallic glass.

$AlCe_3$ intermetallic phase. When a small concentration of aluminum is substituted by a more covalent atom, such as silicon, as in $Ce_{75}Al_{23}Si_2$ metallic glass [52], the transition pressure is modified displaying a transition pressure range twice as large as for the parent compound. With the incorporation of more foreign atoms and the consequent reduction of Ce concentration in $Ce_{70}Al_{10}Ni_{10}Cu_{10}$, $Ce_{55}Al_{45}$ [9] and $Ce_{32}La_{32}Al_{16}Ni_5Cu_5$ [53] the alloys transform at different rate and the pressure range of the transformation as well as the volume reduction increase as the Ce-Ce coordination decreases. Below a certain critical Ce atomic concentration, the $4f$ electron correlation effects are expected to decrease dramatically and, therefore, further dilution of Cerium does not alter the final pressure of the transformation. Finally, note that the transformation starts for all reported values around 2 GPa, independently of the Ce concentration, and at pressures relatively close to that of the polymorphic transformation of crystalline Cerium.

A step further in the investigation of polyamorphic transitions in Ce-based alloys would require to ascertain the specific changes in the electronic structure and bonding driven by Ce $4f$ localization, and can be accessed by inelastic X-ray scattering in the eV energy range, which was not undertaken at this stage. Further information can be obtained by means of X-ray absorption experiments under pressure, which would uncover the local atomic rearrangements taking place at the electronic delocalization and the polyamorphic macroscopic transition.

2.5 Conclusions and Perspectives

A thorough investigation of the behavior of structural and mechanical properties of $Ce_{70}Al_{10}Ni_{10}Cu_{10}$ metallic glass by X-ray diffraction and inelastic X-ray scattering upon application of pressure up to 25 GPa is reported in this work. A low and a high density amorphous phase were found at different pressure ranges, with an intermediate density region which could be a mixture of both phases between 2 and 10 GPa. Decompression from the high density phase results into a reversible change to the ambient pressure phase, though hysteresis is observed in the static structure factor for the intermediate density region. The XRD results correlate well with changes with pressure in the longitudinal acoustic sound speed and the associated elastic constant as revealed by IXS experiments. The hysteresis in structural changes affects the acoustic sound speed and becomes more apparent in the comparison of acoustic mode energies at high momentum transfers. Both structural and dynamical hysteresis effects seem to cancel each other in the estimate of the longitudinal elastic constant.

The observed polyamorphic transition in $Ce_{70}Al_{10}Ni_{10}Cu_{10}$ upon application of pressure is attributed to a change in Ce $4f$ electrons from a localized electronic structure to an itinerant one, similarly to the results reported for other Ce-based MGs and for crystalline Ce. The analysis of reported data on similar polyamorphic transitions for other Ce-based amorphous alloys reveals a broadening of the intermediate density region with increasing atomic alloying and reducing Ce content related to higher diversity of local environments in the more complex Ce-based metallic glasses. This broadening seems to saturate upon decrease of Ce concentrations below 55%. The lower limit for the polyamorphic transformation remains nearly unchanged, at 2 GPa, i.e. double the $\gamma - \alpha$ transition in crystalline Cerium, up to a concentration of 55% atomic Cerium. Further IXS experiments on intermediate Ce-content amorphous alloys are required to fully uncouple the role of $4f$ Ce electrons from lattice degrees of freedom and achieve a better comprehension of polyamorphic transformations in these alloys.

Chapter 3

Microalloying effects of Yttrium in a Fe-based metallic glass and the effect of heat treatment on structural properties and corrosion behavior

Iron-based metallic glasses, also called amorphous steels exhibit valuable properties including excellent corrosion resistance, high specific strength and elastic limit [54, 55, 10, 56]. It has been observed that GFA in amorphous steels increases when large size yttrium or lanthanide atoms are incorporated to the alloy in low atomic percent [57, 58]. In addition, devitrification processes modify the properties of amorphous alloys when thermodynamically stable phases evolve from the metastable amorphous phase.

The Fe-based alloy with the nominal composition $Fe_{50}Cr_{15}Mo_{14}C_{15}B_6$ [59] has demonstrated good mechanical properties and GFA that make it suitable for further studies. Moreover, this composition has been used as starting point for the development of new alloys that present high corrosion resistance [60]. A structural and thermal stability study is realized in this investigation to unveil the role of Y in the physical and electrochemical properties of the system $Fe_{50-x}Cr_{15}Mo_{14}C_{15}B_6Y_x$, with x=0, 1, 2 and 3 (at. %). Several heat treatments for the x=0 alloy were made to follow the crystallization process and correlate different properties with the structure of the former alloys.

3.1 Background

Development and manipulation of metallic glasses as an emerging class of alloys has risen interest within the scientific community due to their special characteristics. The absence of grain boundaries and crystalline phases, common in crystalline materials, often improves the corrosion resistance, mechanical, chemical and magnetic properties which make them appealing for tailored applications [7]. Among metallic glasses, amorphous steels, i.e. Fe-based alloys, own valuable properties, including excellent corrosion resistance, high specific strength and, probably they are among the amorphous materials with the best thermal stability properties [61, 62, 63] . In particular, the Fe-based alloy with the nominal composition $Fe_{50}Cr_{15}Mo_{14}C_{15}B_6$ developed by Ponambalam [59] has demonstrated good mechanical properties and high glass forming ability (GFA) that make it suitable for further studies to evaluate its possible applications. Moreover, this composition has been used as starting point for the development of new alloys, by yttirum and lanthanides addition, that present high corrosion resistance [64].

One of the challenges for fabricating amorphous alloys is the need of high cooling rates to avoid crystallization. It has been observed that bulk metallic glasses (BMGs) with high GFA follow three empirical component rules [1]:

1. Multicomponent systems consisting of more than three elements.
2. Significant difference in atomic size above 12% among the main three constituent elements.
3. Large negative heats of mixing among the constituent elements.

The applicability of such scheme is therefore limited to very well defined range of compositions that allow to form the amorphous structure under very high cooling rate. With the introduction of the concept of multicomponent alloy systems is possible to extend the supercooled liquid region and to reduce the cooling rate to reach the amorphous phase. Furthermore, it has been observed that GFA in amorphous steels increases when large size yttrium or lanthanides atoms are incorporated to the alloy in low atomic percent [11, 58]. It is proposed that the inclusion of these elements introduces atomic-level stresses, which destabilizes the forming crystallites during nucleation. Additionally

segregation of slow diffusing atoms inhibits the growth process once nucleation has been achieved. The size ratio of yttrium and lanthanides respect to iron are among the largest values attainable for Fe-based MGs (see Figure 3.1) [65]. Moreover, this concept has been applied in a significant number of works, including non-ferrous alloys, showing a large improvement on GFA and modification of other properties such as mechanical properties in Cu-Zr-based alloys [66, 67].

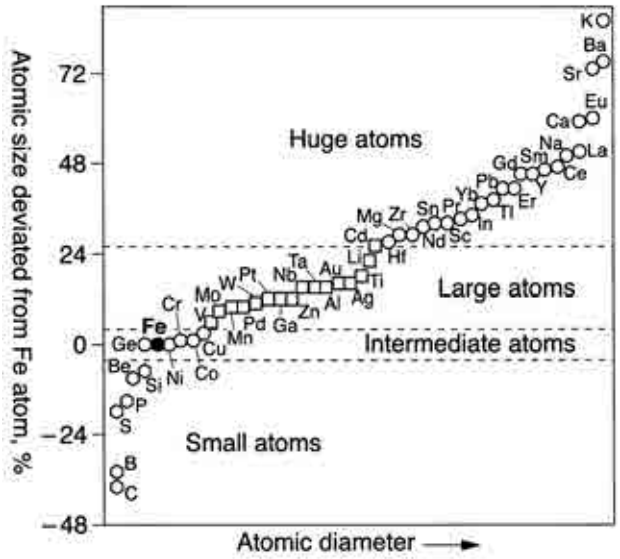

Figure 3.1: Size ratio of the different elements with respect to Fe atom [65].

Besides microalloying, the effect of devitrification processes on nano and microstructure of amorphous alloys represent a field worth exploring. The role of every sort of atoms present in common steels during a heat treatment process has been extensively investigated for crystalline alloys. However, changes on the structure of metallic glasses during a devitrification process are still not well understood. During a crystallization process, nanocrystalline microstructures evolve from the amorphous phase leading to a consequent change in the properties of the original metallic glass. Some improvements on mechanical and magentic properties related to these nanocomposites have been observed, as it has been reported in soft magnetic materials, ultrahigh strength or superplastic alloys [68, 69, 70].

As it is known, the crystallization of amorphous alloys during heat treatments may follow different processes [71, 72]. Some of these processes include polymorphous, eutectoid or primary crystallization and phase separation. The different paths followed in the crystallization processes are summarized in Figure 3.2. In primary crystallization of a binary alloy, used as a model, devitrification takes place upon annealing when nanocrystalline microstructures are formed from a metastable amorphous alloy in a two stage process. First, a primary α phase precipitates from the amorphous matrix at a temperature T_{x1}. In the second stage, an intermetallic compound β appears at T_{x2}. These two crystallization temperatures T_{x1} and T_{x2} can be observed in curves obtained by differential scanning calorimetry (DSC). However, in multicomponent alloys as in the present work, more than one type of intermetallic phase is expected and the involved processes become more complicated. Hence, polymorphous crystallization, eutectoid crystallization or phase separation could be included among the possible different routes followed in the devitrification process.

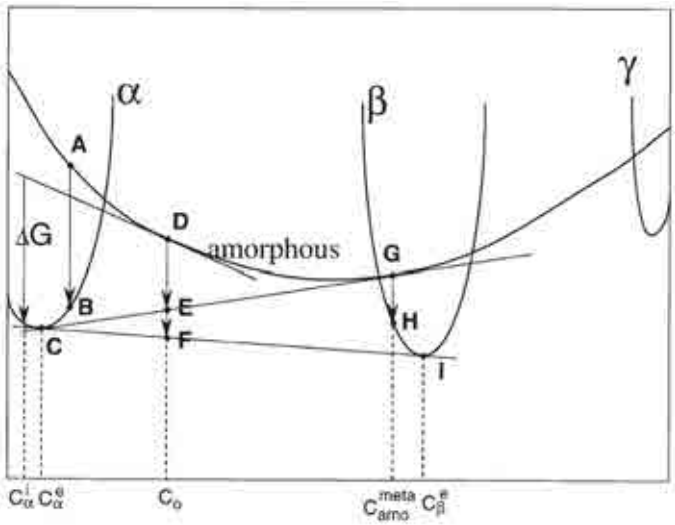

Figure 3.2: Schematic free-energy concentration diagram of a model amorphous binary alloy from Ref. [71] .

After annealing, generally a nanometer-sized structure evolves from the amorphous matrix. Conventional techniques such as energy dispersive X-ray spectroscopy are unable

to resolve chemical composition for small features or phases below 100 nm. On this stage, Scanning Auger Microscopy (SAM) becomes a very useful technique that enables images of the elements in the near surface layer and chemical composition with a magnification up to 50 kX corresponding to a lateral resolution below 10 nm. On the other side, Atom Probe Tomography (APT) is a technique able to provide chemical information near to atomic resolution, giving information about morphology, size and chemistry of the different precipitates. The combination of these two powerful techniques is then optimum for the study of small features in the nanometer range such as the nanocomposites and nanocrystalline microstructures formed after annealing of metallic glasses in this work.

Changes in the microstructure always lead to changes in the properties of the materials. Sometimes these changes are intended to improve characteristics of the initial material and sometimes they conduct to a detrimental effect of the expected behavior. Properties of metallic glasses modified by microalloying or crystallization processes are being studied for different applications or fundamental research. Particularly, corrosion behavior in metallic glasses makes them attractive for applications in aggressive environments. Corrosion resistance in Fe-based metallic glasses was studied for the first time in the seventies in Fe-Cr-P-C and Fe-Cr-Ni-P-C amorphous alloys [73]. Subsequent studies by Archer *et. al.* [74] demonstrated the potential of metallic glasses in the field of corrosion.

It has been proposed that the origin of high corrosion resistance in MGs is associated with the formation of a homogeneous single-phase solid solution that allows selection of easily passivating alloying elements as Cr [75]. In addition, corrosion resistance would be improved by the lack of defects such as grain boundaries, dislocations or chemical segregation that would originate localized corrosion and the subsequent failure of the passive film in those regions. Among the constituent elements of the selected alloys in this Thesis, chromium and molybdenum are well known for their use in conventional alloys because their positive effect on improving the corrosion resistance. Chromium is widely used in stainless steels due to its ability to form highly corrosion resistant chromium oxide and hydroxide passive films. In a similar way, it has been shown that chromium forms a very stable structure in passive films in metallic glasses [76, 77]. In addition, molybdenum is useful to prevent the dissolution of chromium during passivation and it would be expected

to act in a similar manner during dissolution of metallic glasses. Although large amount of works are being reported in this area, the passivation mechanisms, which are responsible for the higher corrosion resistance of metallic glasses, are still not well understood. Furthermore, electrochemical properties of the main alloy change as the microstructure does during devitrification, leading to an even more unfamiliar process.

The results in the present chapter are consequently divided in two sections. The effect of yttirum, as microalloying element, on the GFA is presented first. The superior glass forming ability when 2 at.% yttrium is added as microalloying element to the $Fe_{50-x}Cr_{15}Mo_{14}C_{15}B_6Y_x$ amorphous system is confirmed in Section 3.3.1. Mechanical properties are improved by increasing yttrium content to the main alloy in the same manner. The influence of the surface preparation for electrochemical measurements is also evaluated for the surface as produced and after ion milling process in the same system. Then, a thorough investigation on the structural properties of the $Fe_{50}Cr_{15}Mo_{14}C_{15}B_6$ alloy upon devitrification is reported in Section 3.3.3. Finally, the detrimental effect of heat treatments, and the consequent crystallization of the amorphous phase, on corrosion resistance is pointed out.

Generalities on Atom Probe Tomography and Scanning Auger Microscopy

Chemical composition is important for understanding the mechanisms of the microstructure evolution during crystallization. Conventional analytical techniques, such as energy dispersive X-ray spectroscopy, are not able to deconvolute information from the nanometersized particles in the matrix. Specific techniques like atom probe tomography (APT) and Scanning Auger Microscopy (SAM) may resolve this issue by means of using the field evaporation phenomena. With these methods is possible to sampling the atoms of the nanoparticles formed, as well as the atoms remaining in the matrix.

Atom Probe Tomography (APT) [78], is a technique that provides analytical information with 3D elemental mapping of materials with atomic scale, offering valuable qualita-

tive and quantitative information. The capability to obtain atomic resolution offers new insights on the materials structure and chemistry, and consequently their performance under different conditions. Even if the typical size of the analyzed probes have only few hundred nanometers length, APT compensates with the high chemical sensitivity. APT is nowadays widely used in the field of materials science to identify details of the atomic architecture within solid solutions, particles and their host matrix phase, interface chemistry and crystal misorientation, among others. APT is a technique derived from field ionization, field emission and field evaporation mechanisms and has its origin in the 30ś with the construction of the first field emission microscope. Since then, the technique has evolved and the LEAP (local electrode atom probe) used in this work is, in rough terms, a combination of a two-dimensional position-sensitive detector, which gives lateral information on the x,y positions, coupled to a time-of-flight mass spectrometer to identify each field-evaporated ion.

Essentially, in APT, a sharp needle shaped specimen is cooled to cryogenic temperature and biased with a very large electric field (20-40 V/nm) just below the evaporation point. These fields are only achieved by a geometric field enhancement obtained by preparing the specimen tip with a curvature between 50-100 nm in radius. The specimen is ionized by means of electrical or laser pulses. The electrical pulse is applied in steps from 1 kHz to 250 kHz and a detection rate up to 2×10^6 ion/min can be obtained. In laser evaporation, pulses of the order of picoseconds in the range of green light are used to sublime atoms as ions. The laser is operated in steps from 1 kHz to 500 kHz and a detection rate up to 5×10^6 ion/min can be achieved. Therefore, laser pulsing is 2.5 times faster than electrical pulsing. The time of flight (TOF) ion dispersion is smaller for laser pulsing. When the ions, in laser pulsing surmount the Schottky barrier they have a thermal energy $k_B T$, where k_B is the Boltzman constant and T the temperature. This additional thermal energy diminishes the spread in the momenta (TOF) resulting in larger values of $m/\Delta m$ than for electrical pulsing. The maximum cross section that can be analyzed for both methods is 200×200 nm at the minimum distance from the MCP detector which is 90 mm. By application of voltage or laser pulses the atoms on the surface field evaporate then one at a time and are projected towards a 2D position-sensitive detector, where the (x,y) positions are recorded. Additionally, the Time of Flight (TOF) of the atoms arriving to the detector gives information on the mass over charge ratio

(m/q). The final tridimensional image is then reconstructed from the combination of the 2D position and the field evaporation sequence of the atoms. The evaporation field is approximated as

$$F = \frac{V}{k * r} \tag{3.1}$$

where F represents the maximum field on the specimen, V the applied voltage, r the tip radius and k the field factor, whcich depends on the shape and chemistry of the specimen.

On the other hand, *Scanning Auger Microscopy* (SAM) is a very useful analytical technique in the analysis of surfaces [79, 80]. In general can be applied in elemental identification and quantification on surfaces of materials, depth profiling by sputtering with inner gas, determination of chemical states, adsorption, desorption and surface segregation from the bulk, chemical reactivity by in-situ analysis, and Auger electron elemental map. In general, the spatial resolution is of the order of 0.2 /micro m or less depending on the analysis time, the sampling depth is around three monolayers, and the sensitivity is of the order of 0.3 %.

The Auger effect is observed when an atom is excited by means of an electron or photon beam in the energy range of 2 to 50 keV and a core state electron is ejected creating a core hole. The vacant place is therefore occupied by an electron of a higher energy level releasing an energy equal to the difference in energy of the two interacting orbitals. The transition energy can be coupled to an outer shell electron which is emitted from the atom if the transferred energy is superior to the orbital binding energy. The kinetic energy of the emitted Auger electron corresponds to the difference of the first transition energy and the outer shell electron energy. Since orbital energies are specific for every element, information of the chemical composition of the specimen surface can be obtained with the analysis of the ejected electrons.

3.2 Methodology

3.2.1 Materials

Amorphous alloys with a nominal composition of $Fe_{50-x}Cr_{15}Mo_{14}C_{15}B_6Y_x$, with x=0, 1, 2 and 3 (at.%) were used for this study. The samples were prepared at the Universitat Politecnica de Catalunya (UPC-Campus Castelldefels) and the Universidad de Girona. The alloys were obtained by arc-melting a mixture of all the constituent metals which were entered into the system with a purity from 99.9% to 99.999%.

To obtain rods, Figure 3.3 left, the resultant homogeneous alloys were then re-melted onto the top of a copper mold in a Ti-gettered, argon atmosphere. Cylindrical molds of diameters of 3 and 5 mm were used. The molten liquids were thus drop-cast into the mold by opening a suction valve.

Figure 3.3: Some examples of 3 and 5 mm rods obtained.

In order to prepare ribbons, Figure 3.3 right, the homogeneous alloys obtained in the first step of the arc-melting procedure, were placed in a quartz crucible. The samples were melted by induction and then dropped into a copper wheel turning at 40 m/s. The wheel is refrigerated with water to increase the cooling rate of the samples. The size of the obtained ribbons is 1 to 3 mm width and 30 to 60 micrometers thick approximately. As a by-product of the melt-spinning process "needles" of the same compositions were

also obtained. The identification name and the corresponding composition of the different materials prepared are listed in Table 3.1.

Table 3.1: Identification of the produced $Fe_{50-x}Cr_{15}Mo_{14}C_{15}B_6Y_x$ alloys.

ID	x	Observations
AcY0	0	Bars of 3mm diameter
AcY0	0	Bars of 5mm diameter
AcY0	0	Ribbons
AcY1	1	Ribbons
AcY1	1	Bars of 5mm diameter
AcY2	2	Ribbons
AcY2	2	Bars of 5mm diameter
AcY3	3	Bar of 5mm diameter
AcY3	3	Ribbons

After the melt spinning process, the surface of the ribbons presents two sides: the first one is in contact with the copper wheel during the melt-spinning process and consequently may include some copper contaminations, and the second one is free to the Argon atmosphere, in this case, and presents in general a smother surface. For further references in this work, the first one will be called *back-side* or *opaque-side* and the second one *front-side* or *bright-side*.

3.2.2 X-ray diffraction (XRD)

The structural characterization was performed by X-ray diffraction (XRD) by using two different energies. Valuable information is obtained by XRD since this non-destructive technique is able to provide information on the material structure, either amorphous or crystalline, quantification and phase identification. XRD data used to determine whether a sample is amorphous or not were acquired on beamline BM-16 at the European Synchrotron Facility (ESRF) [81]. The beamline uses a nominal energy of 12.6 keV in the Se K edge. The synchrotron X-ray beam was monochromatized at a wavelength of 0.7748 nm. The samples were positioned at ∼100 and ∼150 mm away from the detector. The measurements were performed in a transmission mode (see Figure 3.4 left). Lanthanum

hexaboride is used for calibration and correction of detector distortions. As XRD data is obtained as a 2D image in the detector plate the *Fit-2D v12.081* program [43] is used to integrate the images.

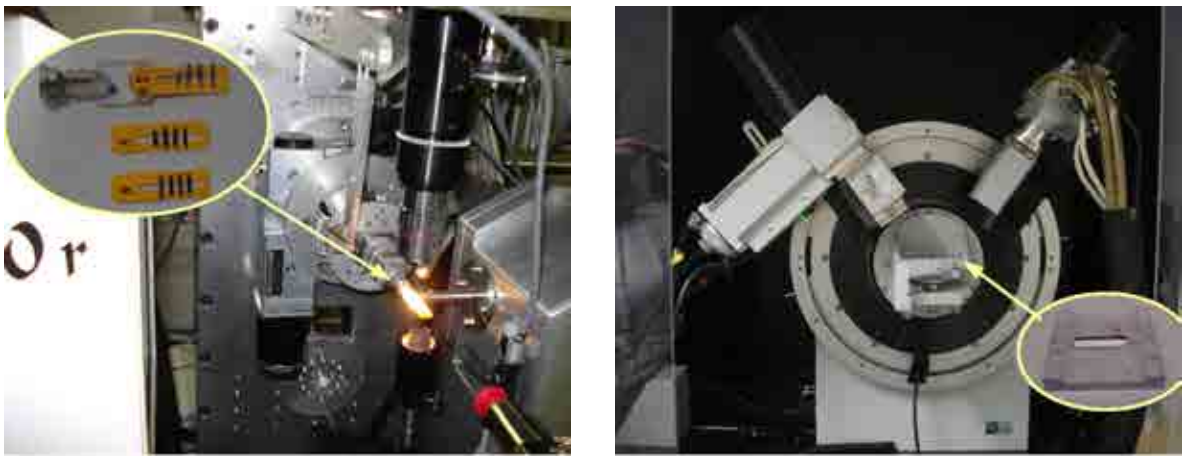

Figure 3.4: XRD experimental setup at the ESRF to the left and at the MPIE to the right.

Additional XRD measurements with monochromatic Cu Kα radiation were taken in a *Bruker AXS* diffractometer at the Max-Planck Institut für Eisenforschung (MPIE) in Düsseldorf, Germany (see Figure 3.4 right). These measurements were set up in 2θ angle in the range of 10 to 110 degrees. Step size of 0.05 degrees, step time of 3s and a slit of 600 μm for the collected data were used. This experimental set up was employed to determine if the $Fe_{50-x}Cr_{15}Mo_{14}C_{15}B_6Y_x$ bars were amorphous or crystalline as well as to follow the $Fe_{50}Cr_{15}Mo_{14}C_{15}B_6$ crystallization process and calculate the crystalline fraction in the annealed ribbons. The crystalline fraction was determined by dividing the peaks area (i.e. crystalline fraction) between the total area under the diffractogram (i.e. crystalline fraction + amorphous fraction). A Lorentzian fit multipeak was used for peaks evaluation as shown in Figure 3.5.

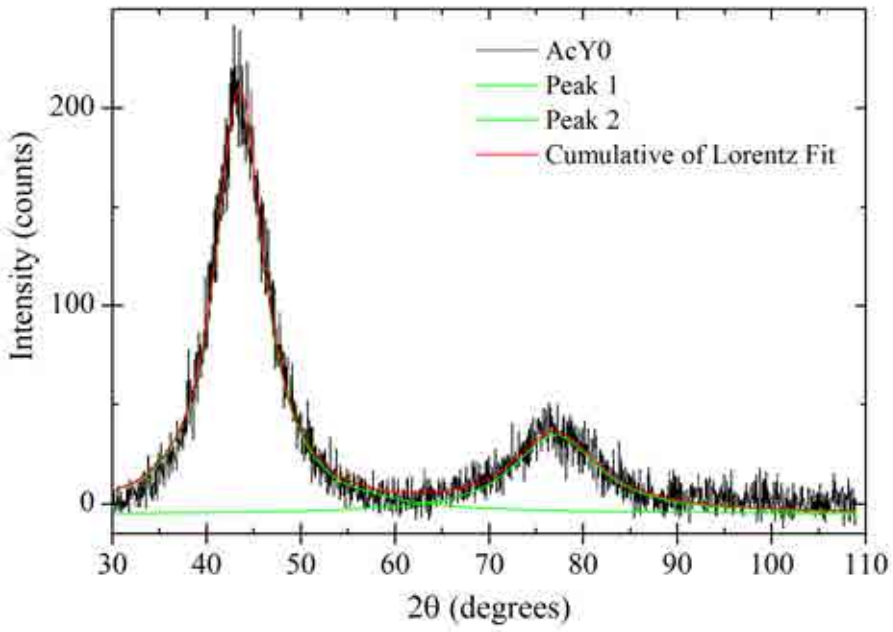

Figure 3.5: Lorentzian fit multipeak used to evaluate XRD measurements realized with the *Bruker AXS* instrument.

3.2.3 Differential scanning calorimetry (DSC)

Thermal stability and thermodynamic properties were studied with a *NETZSCH* differential scanning calorimeter (DSC), at a heating rate of 0.33 K/s, starting at ambient temperature and rising up to 750° C. In this range of temperatures is possible to observe the glass transition and the peaks corresponding to the first crystallization points. The measurements were done in alumina crucibles to avoid contamination during heating.

3.2.4 Scanning Electron Microscopy (SEM)

Scanning Electron Microscopy (SEM), with a FE-SEM (*LEO VP 1550*) coupled with an Energy Dispersive X-ray (EDX) detector (*Oxford*), was used to observe the morphology of the samples and to analyze their composition. The samples were rinsed with ethanol and dried using Nitrogen. Carbon tape was employed to place the samples on the aluminum holder. The working distance varies in a range from 3 to 10 mm. A beam energy

of 15 keV was used for taking the images. All the images were taken with secondary electrons by using an *InLens* detector which allows better resolution. The small size of the crystals formed during annealing and the inability to resolve the signatures of light elements such as C and B, make EDX a useful technique for a qualitative analysis, nevertheless chemical quantification is not possible. Future references in this manuscript to EDX are made just regarding qualitative aspects.

Figure 3.6: Image of the SEM at the MPIE.

3.2.5 Vickers microhardness

Hardness measurements were made using a Vickers microhardness tester. Three different samples of each composition were taken to perform these tests. Ten indentations on every sample were taken at different loads in a range from 0.1 N to 4 N. Finally, a statistical study for every applied load for the different compositions was done. The details about this work can be found in the *Trabajo de fin de carrera* of Guillaume Roinsol at the Universitat Politecnica de Catalunya. In the present Thesis, only the results obtained at 490.6 mN (500 gf) for ribbons of similar thickness are reported.

3.2.6 Heat treatments

Crystallization was induced by thermal annealing of the ribbons in an argon atmosphere inside quartz tubes. The samples were annealed at different temperatures in a range of 550° C to 800° C, during 20 minutes for each temperature. These temperatures were selected following the DSC results (see Figure 3.7 and Table 3.2) and based on the following physical features extracted from it: glass transition temperature T_g, beginning of the first and second crystallization temperatures T_{p1} and T_{p2}, and complete crystallization. It is important to notice that heating kinetics followed in a DSC do not correlate directly with the heat treatments performed, but DSC results can be used as a guide of the transformations undergone by the sample during heating.

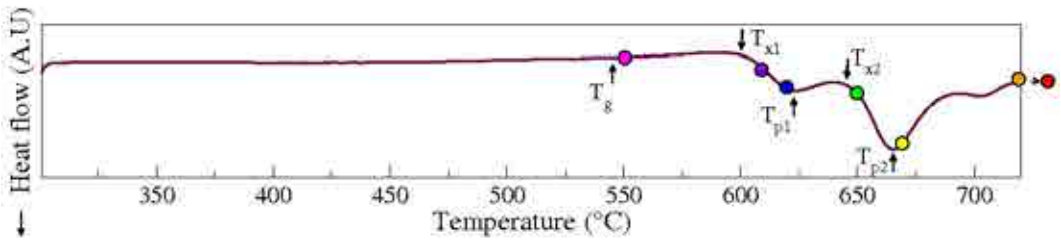

Figure 3.7: DSC curve obtained for the $Fe_{50}Cr_{15}Mo_{14}C_{15}B_6$ ribbons at 0.33 K/s.

Table 3.2: Thermal parameters of the $Fe_{50}Cr_{15}Mo_{14}C_{15}B_6$ metallic glass obtained by DSC at 0.33 K/s.

T_g (°C)	T_{x1} (°C)	T_{p1} (°C)	T_{x2} (°C)	T_{p2} (°C)
545	590	623	640	665

The specimens were then heat treated at 550° C, 610° C, 620° C, 650° C, 670° C, 720° C and 800° C during 20 min. An additional sample was treated at 800° C during 60 min to analyze the time dependence on the crystallization degree.

Heat-treatments were carried out in a furnace of *Heraeus Instruments* with the following procedure. The furnace temperature was ramped from 25° C (room temperature)

up to desired temperature. After the furnace temperature was stabilized, the specimens were introduced into the furnace and hold for the time mentioned before. The samples where taken out the furnace and cooled at room temperature.

3.2.7 Scanning Auger Microscopy (SAM)

As Scanning Auger Microscopy (SAM) enables images of the elements in the near surface layer of conducting samples, this technique was used to analyze the fully-crystalline sample surface, annealed at 800° C during 20 min. The samples were cleaned with isopropanol and dried with compressed air. Two maps were analyzed at different distances from the sample surface: an SAM map was taken at the sample surface after sputter cleaning, the second map was taken after removing a surface layer of ∼300 nm by sputtering at a magnification of 50 kX. 25 keV and $10x10^{-8}$ A electrons were incident upon the sample with a tilting angle of 30°, in ultrahigh vacuum conditions. Detailed scans were finally performed in the regions of interest to evaluate differences in chemical composition in the surface annealed at 800° C during 20 min.

3.2.8 Atom Probe Tomography

The structure before and after annealing of the $Fe_{50}Cr_{15}Mo_{14}C_{15}B_6$ metallic glass was observed by the Atom Probe Tomography (APT) technique. APT measurements were performed using an *Imago - 3D Atom Probe Microscope* of the *LEAP* series *3D-AP* [82] (see Figure 3.8). The measurements were taken in voltage mode at 200 kHz, with a pulse fraction of 15% for a target evaporation rate of 0.5% at a temperature of 60 K. This section of the work was done in a collaboration with Jinfei Chu at the Max-Planck Institut für Eisenforschung in Düsseldorf and part of the results are presented in her Master Thesis. $Fe_{50}Cr_{15}Mo_{14}C_{15}B_6$ samples with different heat treatments were cut by means of a *Helios Nanolab* focused ion beam (FIB), [83, 84] using an energy of 30 kV. A final cleanning process using an energy of 5 kV was performed on the tip surface to reduce Ga ions implantation. Tips with a radius in the range of 30 to 50 nm were obtained by this method. One example of the tips used is presented in Figure 3.9 .

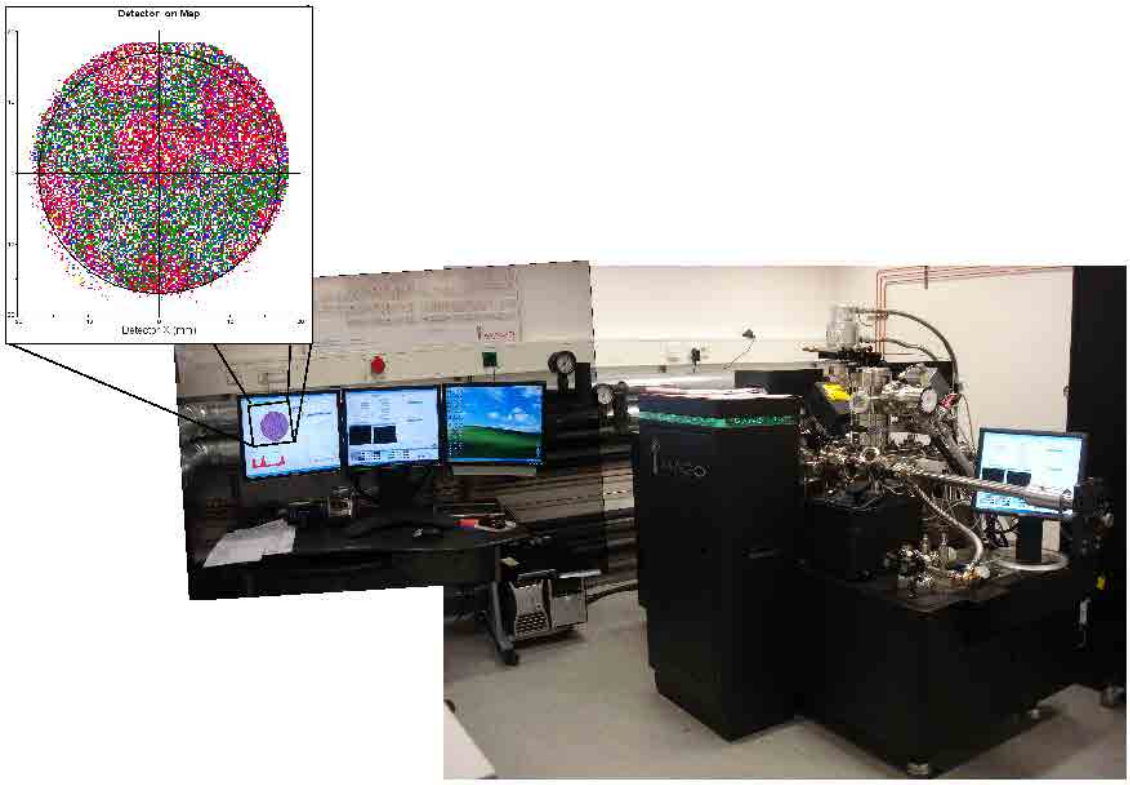

Figure 3.8: Image of the APT at the MPIE during $Fe_{50}Cr_{15}Mo_{14}C_{15}B_6$ measurements.

The number of collected ions used for the 3D reconstruction of the samples annealed at different temperatures are listed in Table 3.3. The tip radius used for the initial 3D reconstruction is measured by high-resolution SEM as shown in Figure 3.9. *IVAS 3.4.1* software was used to visualize and analyze the APT obtained data with the valuable advice of S. Gerstl and P. Choi at the MPIE. After the first reconstruction the size and shape of the precipitates were correlated with TEM images. The initial parameters used for the reconstruction were then adjusted in order to validate the final shape of the different phases formed. The final evaporation field was set between 42 to 46 V/nm, with a compression factor of 1.65.

Table 3.3: Number of collected ions and initial tip radius of the $Fe_{50}Cr_{15}Mo_{14}C_{15}B_6$ annealed samples used for atom probe tomography reconstruction.

Annealing T (°C)	0	550	610	620	650	670	720	800
Tip radius (nm)	18.1	15.0	22.6	20.0	22.0	23.5	14.0	17.5
Detected ions (millions)	1.2	16.1	16.8	12.0	24.6	3.2	10.5	41.4

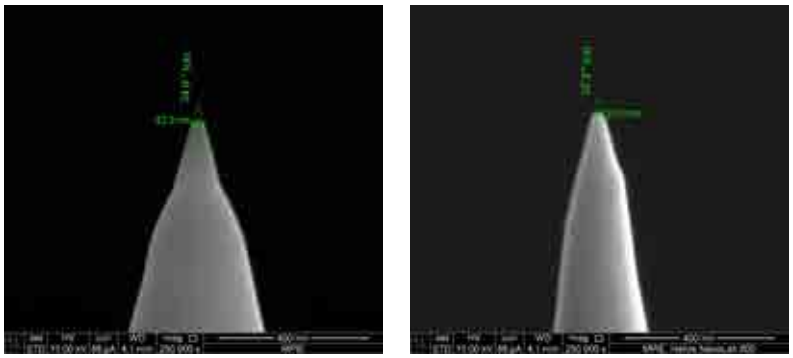

Figure 3.9: Examples of the $Fe_{50}Cr_{15}Mo_{14}C_{15}B_6$ cut tips by the FIB technique. Left: fully amorphous. Right: 550 °C.

A distribution analysis for every element in the alloy at the amorphous state and different annealing temperatures were done. The total volume is divided in small subgroups of 100 elements to calculate the binomial distribution. The statistical analysis is made by using the noncentral chi-square distribution with k independent variables. The chi-square distribution, calculated with the equation 3.2 represents the sum of the square of the independent variables:

$$\chi^2 = \sum_{i=1}^{k} \left(\frac{x_i - \mu_i}{\sigma_i} \right)^2 \tag{3.2}$$

where x_i are independent variables with a normal distribution having means μ_i, and σ_i^2 correspond to the variances for $i = 1, ..., n$. When analysis of categorical data (types of data which may be divided into groups) is concerned with more than one variable, contingency tables are employed. These tables provide a foundation for statistical inference, where statistical tests question the relationship between the variables on the basis of the data observed. The chi-square test in this case is based on a test statistic, X^2, that measures the divergence of the observed data from the values that would be expected

under the null hypothesis of no association.

$$X^2 = \sum \frac{(observed - expected)^2}{expected} \tag{3.3}$$

The χ^2 value is associated with the P-value which is a measure of how much evidence there is to reject a result of the data set. It can be considered to be the probability of obtaining a result at least as extreme as the one observed, given that the null hypothesis is true. The null hypothesis is considered to be the most plausible scenario that can explain a set of data. The smaller the P-value, the more evidence we have against null hypothesis. Generally, a P-value less than 0.05 is regarded as statistically significant, which means that the observed deviation from the null hypothesis is significant.

An iterative process based on the iso-concentration surfaces was used to evaluate the composition of the different phases formed in the annealed samples. In this method, a first guess of the interface is based on visual changes in composition. The region of interest is isolated and the mass-spectrum that provides the composition is evaluated. Additionally, a proximity histogram (proxigram) across the interface is calculated. A proximity histogram generates concentration profiles across complex interfaces [85]. In this method, the position and chemical information are integrated to generate an atomic fraction versus distance to the interface histogram. In practice, this approach can be useful to evaluate concentration profiles as well as interfacial excesses for all the internal interfaces in the analyzed volume. A second value for the iso-concentration surface is then chosen expected to be closer to the composition inside the selected volume according to the evaluated proxigram. This process is done iteratively until the composition inside the selected volume becomes constant in a plot of composition versus value of the isoconcentration surface.

3.2.9 Thermo-Calc

Thermo-Calc is an efficient software package able to calculate thermodynamic and phase diagram for multi-component systems. Databases are available for Steels, Ti-, Al-, Mg-, Ni-alloys, multi-component oxides and many other materials [86]. This software is based on thermodynamic databases obtained by evaluation of experimental data and statistical

thermodynamics using the *Calphad* method.

Thermo-Calc calculations were performed to determine the equilibrium phase distribution and composition of the individual phases at specific temperatures. The database *TCFE5* and the version *R* of Thermo-Calc [86] were used for thermodynamic calculations of the $Fe_{50}Cr_{15}Mo_{14}C_{15}B_6$ heat treated samples. This section forms also part of the work in collaboration with Jingfei Chu for the obtaining of her Master degree, at the Max-Planck Institut für Eisenforschung in Düsseldorf.

3.2.10 Linear polarization

Electrochemical measurements using a scanning flow cell (SFC) [87], were performed to evaluate the corrosion behavior. The SFC used is a three-electrode setup with a gold counter electrode and a micro Ag—AgCl reference electrode. All potentials are referred to SHE. The capillary area analyzed with this setup is 0.35-0.40 mm^2 approximately. The open circuit potential (OCP) was monitored during 1000s in 0.1 M HCl aqueous solution. After that time the OCP became steady. The linear polarization curves were measured then with a potential scan rate of 2 mV/s and an energy step of 0.25 V at ambient pressure. The scans were evaluated in the anodic and cathodic directions in independent sweeps.

All samples were rinsed with ultra pure water and ethanol and dried with nitrogen before using. As indicated in the results section, in some cases the native oxide layers were removed by means of the ion milling process in a *Precision Etching Coating System, Gatan model 682*. The procedure is carried out in vacuum around 5 Torr, with a tilting angle of 70-75°and rotation of the sample of 10 rpm. Argon ions are used with an energy of 5 keV and etching gun current of 300μ A during 7 min.

3.3 Results and discussion

In Section 3.3.1, a study of yttrium microalloying effects on structural and electrochemical properties of $Fe_{50-x}Cr_{15}Mo_{14}C_{15}B_6Y_x$ amorphous alloys, with x = 0, 1, 2, and 3 at. % is presented. Ribbons and bars were prepared by the melt-spinning and copper mold casting methods respectively. An improvement on glass forming ability upon yttrium addition in small concentration is observed. The maximum diameter attainable of amorphous $Fe_{50}Cr_{15}Mo_{14}C_{15}B_6$ was 3 mm. The addition up to 3 at.% Y allowed to prepare bars of 5 mm diameter. Although the maximum diameter reported for the $Fe_{48}C_{15}Mo_{14}Cr_{15}B_6Y2$ is 9 mm [59], the size of the bars reached in this work is also limited by the instruments used. Vickers micro-hardness was used to evaluate the GFA and yttrium influences on this mechanical property. Finally, linear polarization tests show that there is not a significant effect of yttrium in the final breakdown potential of the alloys studied.

The structural changes of $Fe_{50}Cr_{15}Mo_{14}C_{15}B_6$ glass upon heat treatment over a range of temperatures between the glass transition temperature and a fully crystalline state are presented in Section 3.3.3. Melt spun ribbons annealed at different temperatures were analyzed by XRD, SEM, APT, SAM, and thermodinamical calculations. The evolution of the microstructure is followed at the different stages of the primary crystallization through which two main phases are formed: $M_{23}(C,B)_6$ and M_6C. The composition of the formed carbides approaches to the predicted concentration of stable phases by ThermoCalc. The effect of the developed structure upon electrochemical properties is also reported. The material exhibits a detrimental effect on corrosion resistance as the crystallization process proceeds.

3.3.1 Yttrium concentration dependence on modification of local order and glass forming ability in $Fe_{50-x}C_{15}Mo_{14}Cr_{15}B_6Y_x$ metallic glasses

Figure 3.10 shows X-ray patterns of ribbons with different yttrium content. The measurements were taken using synchrotron radiation at the ESRF, in Grenoble, France, as explained in Section 3.2.2. The results are presented as function of the wave number, $Q = 4\pi \sin(\theta)/\lambda$, where θ is the scattering angle and λ the wavelength of the X-rays used during the measurements.

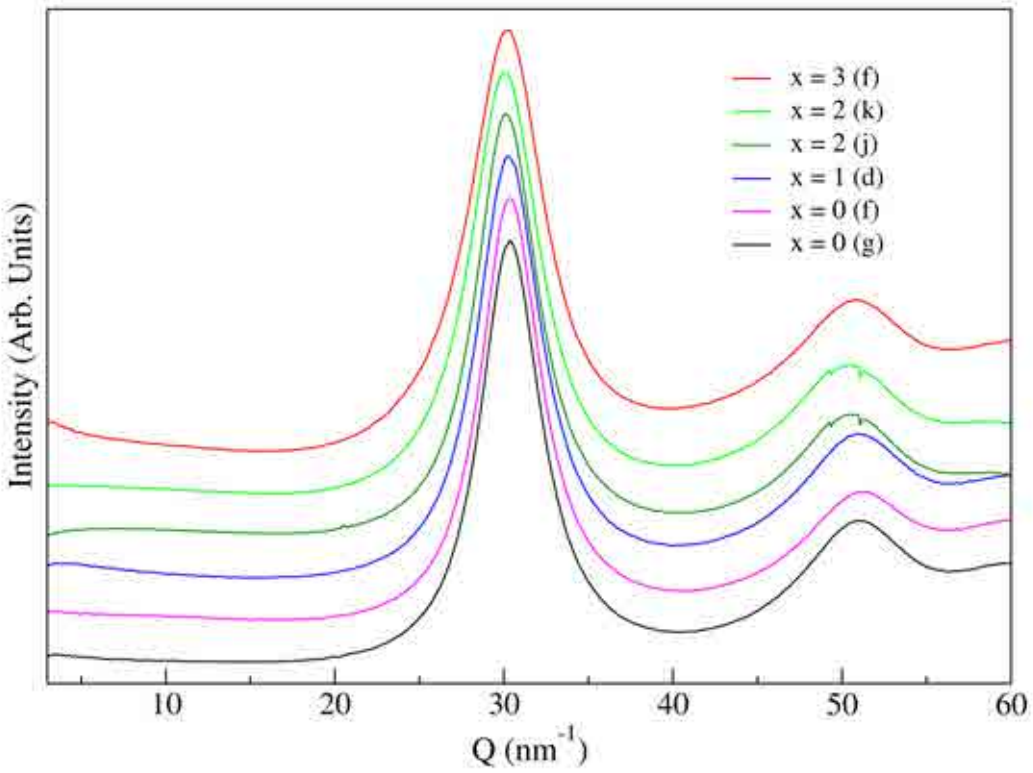

Figure 3.10: X-ray diffractograms of the of the $Fe_{50-x}Cr_{15}Mo_{14}C_{15}B_6Y_x$ ribbons, with different yttrium concentrations, x, (letters in parentheses indicate only different productions of samples).

Table 3.4: Thickness of the ribbons and position of Q_{max} for the different $Fe_{50-x}Cr_{15}Mo_{14}C_{15}B_6Y_x$ alloys as function of the Yttrium concentration.

x (at. %)	Thickness (μ m)	Q_{max} (nm^{-1})
0	$\sim$ 30	30.35
1	$\sim$ 30	30.20
2	$\sim$ 30	30.08
3	$\sim$ 50	30.28

The static structure factor, $S(Q)$, of the as produced $Fe_{50-x}Cr_{15}Mo_{14}C_{15}B_6Y_x$ ribbons, with x=0, 1, 2, 3 at. %, shows broad diffuse peaks and no signals of Bragg peaks which are characteristic of crystalline phases. Therefore, it is possible to prepare fully amorphous ribbons at all studied compositions range. The thickness of the ribbons used and the position of the main peak (Q_{max}) are presented in Table 3.4. Q_{max} values for different samples production but the same composition are equal and just the general value is presented in the table. The static structure factor, as explained in Chapter 2, provides information related to the atomic arrangement and the interference patterns in the measured materials. The reduction of the Q_{max} values as the yttrium concentration increases from 0 to 2 at.% is a signal that larger atoms are being incorporated into the random arrangement in the alloy. Contradictorily, when 3 at.% Y is added the Q_{max} value increases again which indicates a more compact atomic arrangement.

XRD patterns of the obtained bars, with different yttrium content, were acquired with monochromatic Cu Kα radiation in a *Bruker AXS* instrument as explained in Section 3.2.2. The results are reported in terms of the diffraction angle θ. From Figure 3.11 is observed that is possible to prepare 5 mm diameter bars with x=1, 2 and 3 at. %. Diffractograms for these compositions do not show Bragg peaks, as indicator of the amorphous state. On the other hand, when no yttrium is added to the composition (*i.e.* x=0 at. %) is only possible to prepare fully amorphous rods of 3 mm diameter while 5 mm diameter rods are partially crystalline. It is important to recall that the critical size obtained for a specific composition depends on the glass forming ability and the cooling rate. For similar casting systems with small differences in the design different cooling rates are expected and therefore differences on the critical size of the amorphous probes

obtained. The results presented here, correspond to ribbons and rods prepared always under the same conditions. The main phases observed in the partially crystalline rods without Yttrium are $M_{23}C_6$ and M_6C. These two carbides correspond to the same phases obtained after the devitrification process presented in Section 3.3.3 for ribbons with the same composition.

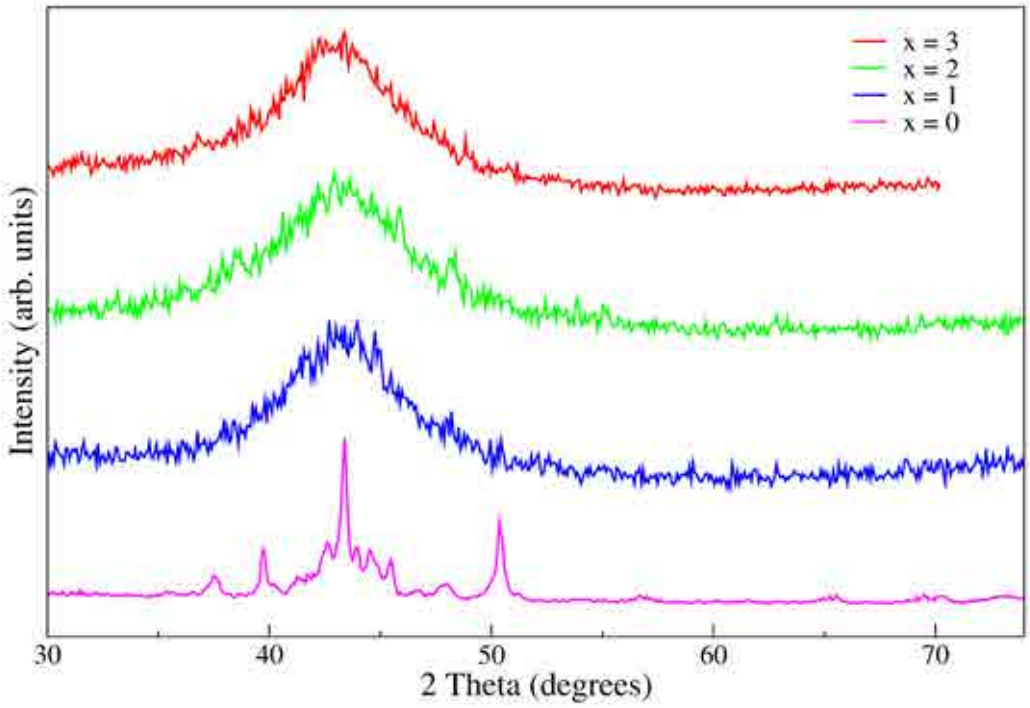

Figure 3.11: X-ray diffractograms of the of the $Fe_{50-x}Cr_{15}Mo_{14}C_{15}B_6Y_x$ 5 mm diameter rods, for different Yttrium concentrations.

Table 3.5: Position of θ for the different $Fe_{50-x}Cr_{15}Mo_{14}C_{15}B_6Y_x$ 5mm rods as function of the Yttrium concentration.

x (at. %)	θ (degrees)	Width (degrees)
0	41.72	-
1	43.402(3)	5.342(11)
2	43.342(2)	5.777(8)
3	43.087(2)	6.276(7)

As expected for amorphous alloys, the system $Fe_{50-x}Cr_{15}Mo_{14}C_{15}B_6Y_x$ (x= 0, 1, 2, 3 at. %) presents a smooth surface with metallic luster. Figure 3.12 shows SEM images of the as produced ribbons with different yttrium concentration at a low magnification of 10 kX. Here it is possible to observe that the prepared ribbons are in general homogeneous and no signals of pores or roughness are observed. It is worth to recall that no polishing was performed on the samples surface and they were only rinsed with water and ethanol and dried with nitrogen before the SEM measurements. Figure 3.13 shows SEM images of the as produced ribbons at a higher magnification of 100 kX. In this new set of images, no contrast of crystalline phases was observed over the surface for any of the ribbons as produced.

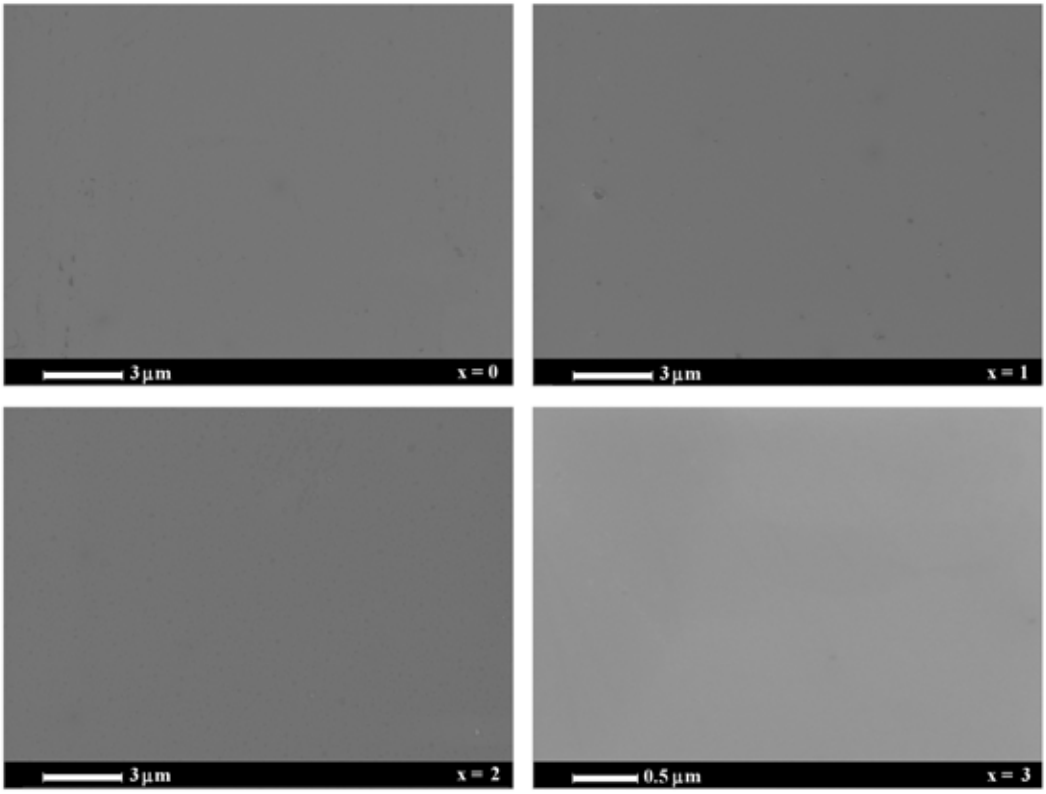

Figure 3.12: SEM surface pictures of the $Fe_{50-x}Cr_{15}Mo_{14}C_{15}B_6Y_x$ (x=0,1,2,3 at. %) fully amorphous samples at a magnification of 10 kX (x=0,1,2) and 50 kX (x=3).

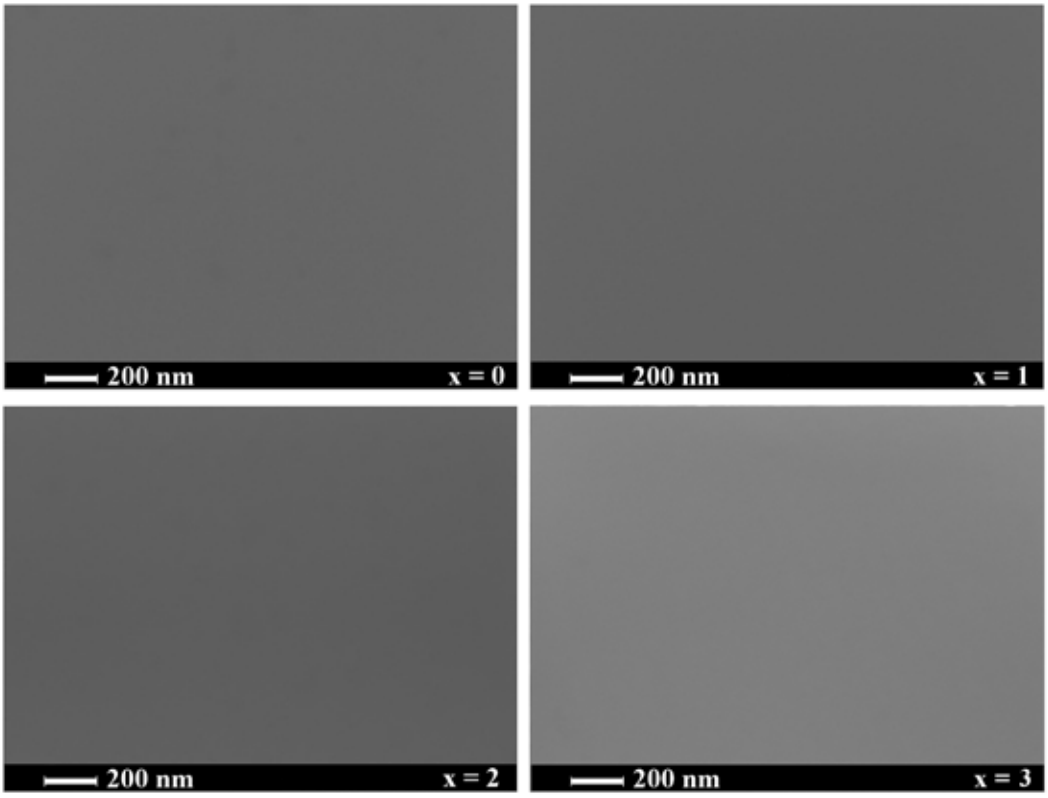

Figure 3.13: SEM surface pictures of the $Fe_{50-x}Cr_{15}Mo_{14}C_{15}B_6Y_x$ (x=0,1,2,3 at. %) fully amorphous samples at a magnification of 100 kX.

Figure 3.14 shows typical DSC curves of the $Fe_{50-x}Cr_{15}Mo_{14}C_{15}B_6Y_x$ (x= 0, 1, 2, 3 at. %) amorphous ribbons. T_g, T_x, and T_p correspond to the glass transition temperature, the first crystallization temperature, and the peak of the crystallization, respectively. The crystallization temperature, T_x, is defined as the onset temperature of the crystallization reaction. The values of the thermodynamical properties, T_g, T_x and T_p, increase with the Yttrium content as shown in Table 3.6. The interval of the supercooled liquid region, $\Delta T_x = T_x - T_g$, is used as an indicator of the thermal stability of the supercooled liquid in metallic glasses. The higher the ΔT_x value, the higher is the thermal stability of the supercooled liquid against crystallization. From Table 3.6 is possible to observe that the larger ΔT_x value corresponds to the introduction of 2 at. % Yttrium. This alloy presents a high glass forming ability (GFA) and a high diameter of the glassy alloy up to 9 mm according to the results reported by Ponnambalam *et.al.* [59]

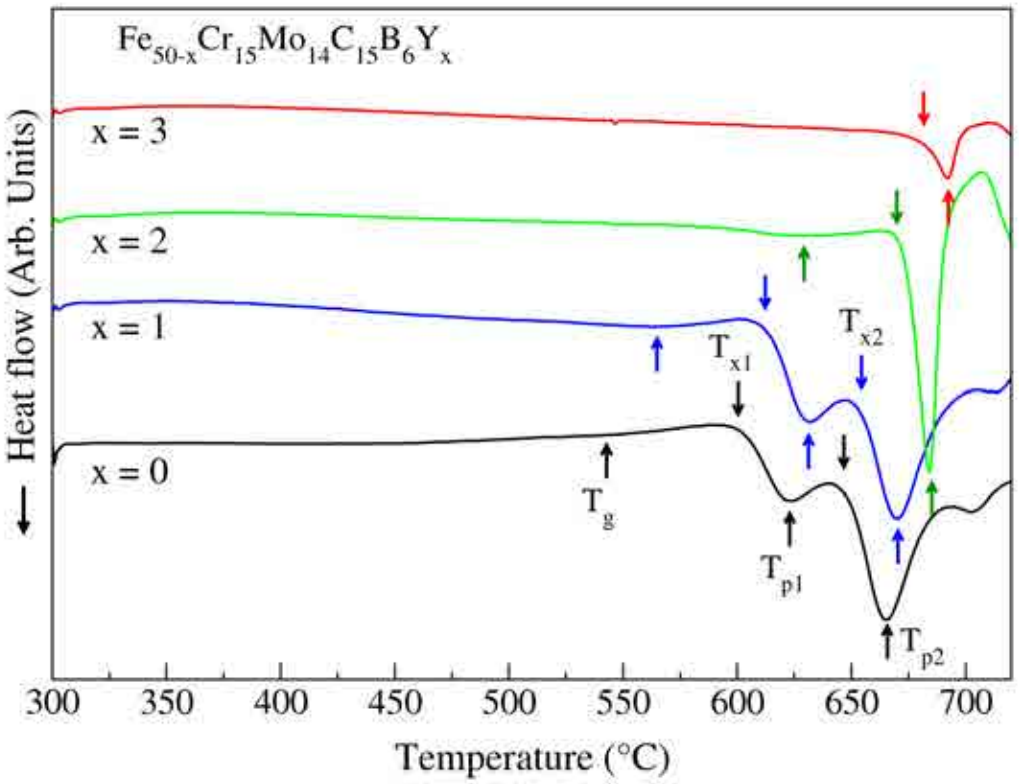

Figure 3.14: DSC of the $Fe_{50-x}Cr_{15}Mo_{14}C_{15}B_6Y_x$ (x=0,1,2,3 at. %) fully amorphous samples. The curves were obtained at 0.33 K/s.

It is proposed that the improvement on GFA is related with a reduced stability of the metastable $Fe_{23}C_6$ phase in presence of yttrium atoms. $M_{23}C_6$ is the first phase formed in a devitrification process of the $Fe_{50}Cr_{15}Mo_{14}C_{15}B_6$ amorphous alloy as will be presented in section 3.3.3. Upon yttrium alloying the growth of this phase is limited by the slow diffusion of yttrium atoms outward of the forming crystals. As the yttrium content increases, more atoms randomly accommodated in the amorphous alloy they have to migrate to permit the crystal formation. As a result, the stability of the $M_{23}C_6$ phase decreases, enabling the formation of larger bulk metallic alloys for this composition.

On the other hand, although it has been suggested that extrinsic effects of Y may

Table 3.6: Thermal parameters of the $Fe_{50-x}Cr_{15}Mo_{14}C_{15}B_6Y_x$ system as function of the Yttrium concentration.

x (at. %)	T_g (° C)	T_{x1} (° C)	T_{p1} (° C)	ΔT_x (° C)
0	545	590	665	45
1	561	603	670	42
2	614	664	684	50
3	624	671	692	47

contribute to GFA enhancement, it is reported that they play a negligible role in this regard. It has been proposed that Y acts as oxygen scavenger in some Fe-based MGs [88]. Heterogeneous nucleation is then suppressed and in consequence an improvement on the GFA is observed. However, quantification of the oxygen concentration in $Fe_{50-x}Cr_{15}Mo_{14}C_{15}B_6Y_x$ as cast amorphous samples with different Er content and 2 at. % Y content has demonstrated that the very low oxygen concentration can not lead to an heterogeneous nucleation [59]. Then the role of the molten carbides in this high-carbon alloys as fluxing agent to eliminate oxygen inclusions during the melting process is proposed in the same work.

Finally, the effect of Y on glass forming ability is corroborated in this work by showing that the addition of 2 at.% Y in the $Fe_{50-x}Cr_{15}Mo_{14}C_{15}B_6Y_x$ system, stabilizes the glassy state, presenting the highest supercooled liquid region of the studied compositions. The retarded formation of the $Fe_{23}C_6$ phase as consequence of small concentrations of yttrium, even 1 at.%, allows the fabrication of larger bulk metallic glasses. Technical limitations in this work for samples preparation allow the fabrication of bars with a maximum diameter of 5 mm. However, the production of larger alloys by Y microalloying has been shown in other studies.

As it has been pointed out, Yttrium is widely used to improve glass forming ability, but its effects on the alloy properties go beyond the stabilization of the amorphous phase. It has been reported that yttrium additions in amorphous alloys also improves their mechanical properties. Mechanical measurements to evaluate microhardness in the $Fe_{50-x}Cr_{15}Mo_{14}C_{15}B_6Y_x$ system were performed using a Vickers microhardness

tester. Usually Vickers microhardness is expressed as a number only (without the units kgf/mm^2), indicating the applied load (in gf) as subindex (*e.g.* 753 HV_{900}). However, the recent use of of SI units (MPa or GPa) in academic papers makes the units conversion necessary. To convert a Vickers hardness number to force units the applied force is converted from kgf to Newtons and the area from mm^2 to m^2.

The microhardness measured for the samples with different yttrium concentration are presented in Table 3.7. The results are reported in HV units and in SI units (GPa). Thickness is a relevant factor when measuring microhardness in ribbons. To ensure a good measurement, ribbons must be at least three times thicker than the penetration depth, otherwise the final values may correspond to a combination of the sample and the holder hardness. To reduce the penetration depth in thin samples a low load must be applied. However, by decreasing the applied load, the size of the indentation is also reduced and the measurement error increases. A good compromise between applied load and error on indentation measures was found in this work for an applied load of 250 gf and the use of samples with similar thickness.

Table 3.7: Vickers microhardness of the $Fe_{50-x}Cr_{15}Mo_{14}C_{15}B_6Y_x$ ribbons as function of the concentration for an applied load of 250 gf (245.3 mN).

X (at. %) =	0	1	2	3
Thickness (μm) =	∼40	∼40	∼30	∼25
HV_{250} =	1144(23)	1194(35)	1232(29)	1246(37)
Hardness (GPa) =	11.22(22)	11.71(34)	12.08(28)	12.22(36)

Hardness dependence on yttrium concentration is presented in Figure 3.15. Even if error bars of the measures for the different compositions overlap, as shown in the figure, it is possible to observe a trend in this property. Results show that ribbons hardness increases as the yttrium content does. The superior bulk modulus of yttrium with respect to the elements of the main composition and his contribution on the strengthening of the lattice are the suggested properties that contribute to this characteristic. Superior mechanical properties of the alloy with higher GFA was reported in Zr-based alloys. In this study is not possible to define a similar behavior due to the small difference found between hardness values for x = 2 and 3 at. % and the high overlap in their error bars.

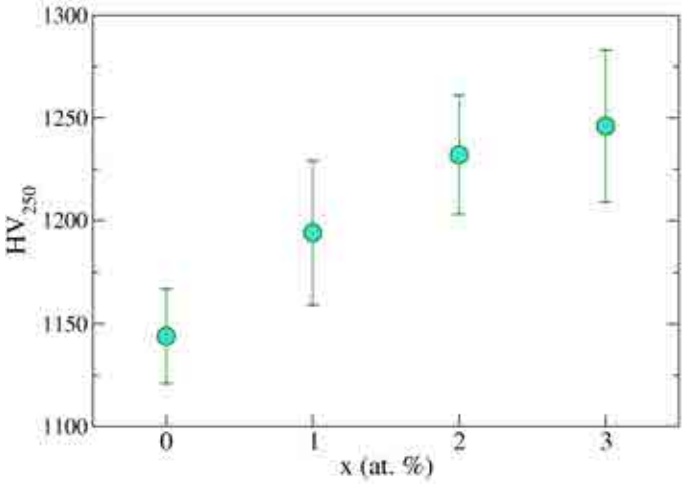

Figure 3.15: Vickers microhardness of the $Fe_{50-x}Cr_{15}Mo_{14}C_{15}B_6Y_x$ (x=0,1,2,3 at. %) fully amorphous samples for different applied loads.

Nevertheless, it is possible to observe a slight increase in the hardness related to the higher yttrium content in the alloy with 3 at. % with respect to the one that posses the highest GFA. Finally, microhardness values reported above in this work are in the range of the reported values for the Fe-based alloys proposed as structural steels which lies between 1200 to 1300 HV_{300} [58]. In order to obtain a better knowledge related to the yttrium effect on mechanical properties, nanoindentation might be considered for further studies.

Besides hardness and mechanical properties, electrochemical properties may be also affected by yttrium microalloying. Among the elements in the alloy, Mo and Cr have a favorable effect on corrosion properties and their effects have been studied since the late 80´s. In Fe-based alloys, molybdenum assists the formation of the passive hydrated chromium oxyhydroxide film. However, passive molybdenum films are less stable than the chromium ones and Mo suffers transpassive dissolution at high potentials in the passive region. Large amounts of Mo in the alloy generate a passive film whose content of molybdenum in an unstable valence state is high. In consequence, Mo has a beneficial effect on corrosion resistance when is not added in excess.

Figure 3.16 presents the results obtained by potentiodynamic polarization for the $Fe_{50-x}Cr_{15}Mo_{14}C_{15}B_6Y_x$ MGs in HCl 0.1 M: (a) as produced ribbons just cleaned with ethanol, (b) after polishing by using the ion milling process. From the plots is possible to observe that all alloys passivate at a low current density. Samples analyzed without removing the native oxide layer passivate in two ranges of current density. $Fe_{50-x}Cr_{15}Mo_{14}C_{15}B_6Y_x$ with low yttrium content, x = 0,1 present passivity at the lowest current density, around 1×10^{-5} A/cm^2. Alloys with higher yttrium content passivate around 2×10^{-5} A/cm^2. When the surface is completely removed before polarization the samples passivate at a higher current density of approximately 4×10^{-5} A/cm^2. In all cases a large passive region is observed up to 1.1 V. The corresponding rise in the current density to the transpassive dissolution of molybdenum [89] above 0.7 V is more pronounced for the yttrium containing ion milled samples. When any initial sample preparation is carried out (*i.e.* no polishing), the current density increases continuously until transpassive dissolution of chromium above 1.1 V is observed [90].

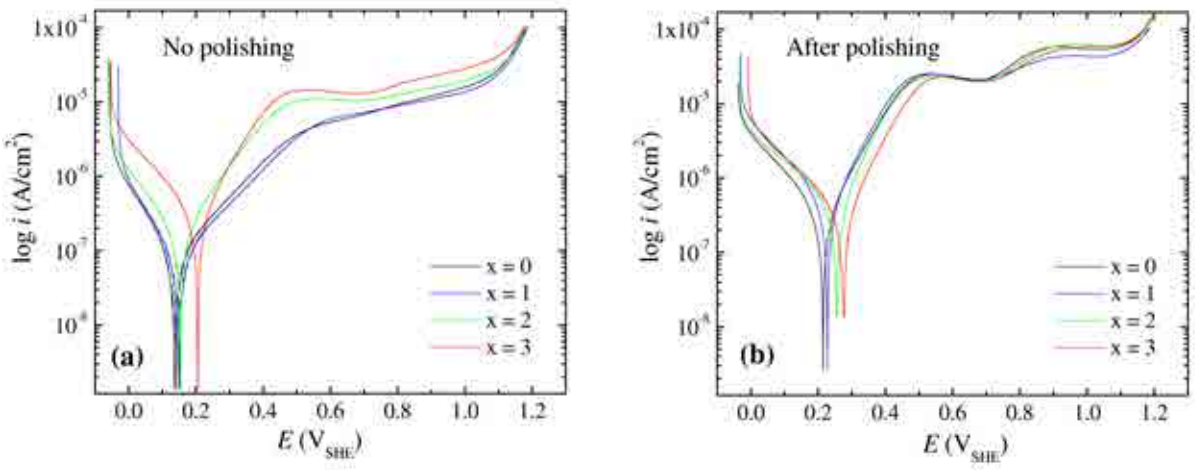

Figure 3.16: Potentiodynamic polarization curves of the $Fe_{50-x}Cr_{15}Mo_{14}C_{15}B_6Y_x$ (x=0,1,2,3 at. %) fully amorphous samples in HCl 0.1 M.

Some electrochemical parameters as function of the yttrium content and the starting state of the surface in HCl 0.1M were calculated from the polarization curves and summarized in Table 3.8. The corrosion potential, E_{corr}, and the corrosion current density,

Table 3.8: Electrochemical parameters obtained from the polarization curves of the amorphous $Fe_{50-x}Cr_{15}Mo_{14}C_{15}B_6Y_x$ as function of the yttrium content.

Without polishing			
x (at. %)	E_{corr} (V_{SHE})	i_{corr} $\times 10^{-7}$ (A/cm^2)	i_{pass} $\times 10^{-5}$ (A/cm^2)
0	0.132	0.886	1.356
1	0.143	0.844	1.290
2	0.148	1.664	1.651
3	0.206	2.771	2.538
After polishing			
x (at. %)	E_{corr} (V_{SHE})	i_{corr} $\times 10^{-7}$ (A/cm^2)	i_{pass} $\times 10^{-5}$ (A/cm^2)
0	0.207	3.446	1.475
1	0.246	4.614	4.234
2	0.261	4.236	5.792
3	0.278	3.872	5.872

i_{corr}, were calculated from the linear fitting of weak polarization region. The passive current density, i_{pass}, was obtained as average of the current densities in the passivation range between 0.5 and 1 V. The open circuit potential (OCP) is reported after 1000 s of immersion in the electrolyte, after this period of time, the OCP becomes stable.

Two different observations can be derived from the plots: first, the influence of yttrium concentration added as a microalloying element to the main alloy, and second, the effect of sample preparation prior to the polarization tests, both affecting in a separate way the electrochemical properties of the studied alloys. The biggest influence of yttrium is considered in the corrosion potential E_{corr} were a constant shift to more anodic potentials is observed as the yttrium concentration increases. i_{corr} and i_{pass} slowly increase with yttrium concentration when the samples present their original surface whilst for the polished samples this properties exhibit a slight increment from 0 to 1 at.% yttrium and then they remain stable up to 3 at.% Y. The OCP of the passive films shows an increment for the lower yttrium content and decreases at 2 at.% yttrium, contradictorily to expectations, to finally increase again at 3 at.%.

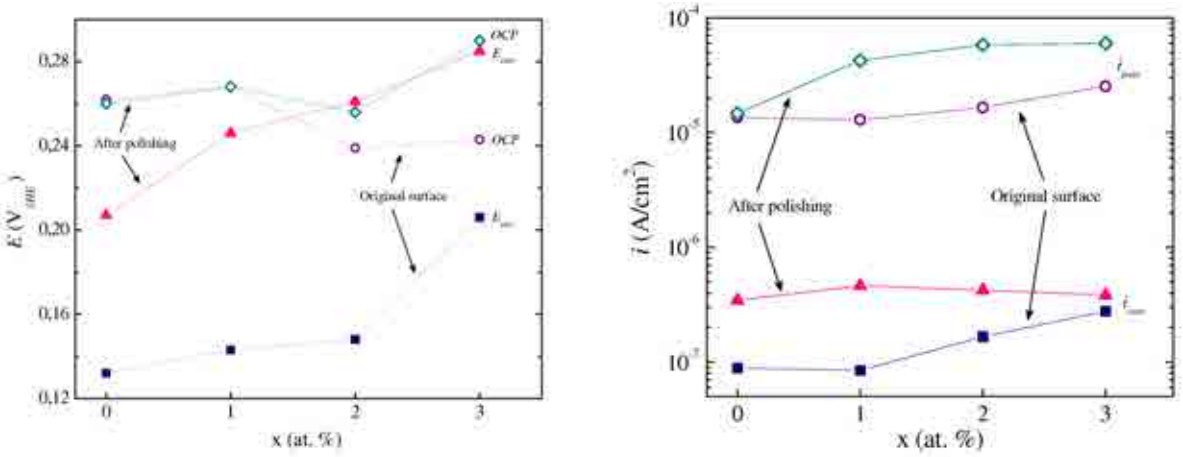

Figure 3.17: Analysis of the parameters obtained from potentiodynamic polarization curves of the $Fe_{50-x}Cr_{15}Mo_{14}C_{15}B_6Y_x$ (x=0,1,2,3 at.%) fully amorphous samples in HCl 0.1 M.

On the other hand, a more significant result is related to the initial surface preparation for the electrochemical measurements. In general, higher values in corrosion and passivation current densities are observed in the polished samples. The OCP and the corrosion potential shift to the anodic direction when the original passive layer is freshly removed by polishing. Even if a native oxide layer would be formed immediately after the polishing process by exposing the samples to air, the initial oxides and impurities formed during the melt spinning process proved to provide an extra protection against acid environments. However, in order to ensure reproducibility, freshly polished samples would be desirable, since the dispersion in the curves becomes negligible after this process. At last, the final breakdown of the corrosion resistance is similar for all the alloys, with and without yttrium content, and before and after the surface polishing. The high corrosion resistance is then ensured by the high amount of passivating elements and the homogeneity of the amorphous film.

3.3.2 Conclusions and perspectives

The effect of Y on glass forming ability is corroborated in this work by showing that the addition of 2 at.% Y in the $Fe_{50-x}Cr_{15}Mo_{14}C_{15}B_6Y_x$ system, stabilizes the glassy state, presenting the highest supercooled liquid region of the studied compositions. The retarded formation of the $Fe_{23}C_6$ phase as consequence of small concentrations of yttrium, even 1 at.%, allows the fabrication of larger bulk metallic glasses. The slow diffusion of yttrium retards the formation of the first nuclei and slows down the growth of the formed crystals as suggested by other authors. Technical limitations in this work for samples preparation allow the fabrication of bars with a maximum diameter of 5 mm. However, the production of even larger alloys by Y microalloying would be expected. Mechanical properties are also increased by yttrium incorporation into the alloy. The large size of yttrium atoms that contributes to strengthening the lattice and its superior bulk modulus contribute to a higher hardness than the base alloy. Nanoindentation and tension tests would be then advised to further understand the role of yttrium in the mechanical properties of amorphous steels and the formation of shear bands in similar alloys.

The study on the corrosion propeties shows that all the composition of the amorphous system $Fe_{50-x}Cr_{15}Mo_{14}C_{15}B_6Y_x$ for x = 0,1,2,3 at.% passivate spontaneously in HCl 0.1M. The large amount of passivating elements together with the uniformity of the amorphous phase provide the alloy with an excellent corrosion resistance. The final breakdown potential is similar for all the compositions, indicating that there is not a remarked influence on the corrosion behavior by addition of small amounts of yttrium and only small changes in the general behavior can be pointed out. The anodic current density in the active region slightly increases when yttrium is added. The small increase of the passive current density indicates the formation of a slightly lower protective quality of the passive film. Nevertheless, these small differences do not compromise the general stability of the material or the macroscopic behavior. The surface preparation of the alloy prior to the measurements proved to be a key aspect to ensure reproducibility of the data. Surface impurities and initial oxides formed during the melt spinning process provide an extra protection to the alloy, however, as the film is at the end not homogeneous, a prior preparation by ion-milling to remove these impurities would be advised.

3.3.3 Phase segregation and crystallization in a $Fe_{50}Cr_{15}Mo_{14}C_{15}B_6$ metallic glass

The general composition of the $Fe_{50}Cr_{15}Mo_{14}C_{15}B_6$ alloy was determined by inductively coupled plasma mass spectrometry (ICP) and is presented in Table 3.9. A slight deviation of the nominal composition is observed. These variations in composition are generally originated during sample preparation. Small fractions of material may be ejected from the melt during the arc melting process thus changing the final concentration.

Table 3.9: General composition obtained by ICP of the $Fe_{50}Cr_{15}Mo_{14}C_{15}B_6$ amorphous alloy.

Element	Fe	Cr	Mo	C	B
Concentration (at. %)	53.72	13.35	13.07	14.92	4.94

Crystallization process may be followed according to the signals observed by X-ray diffraction upon annealing. X-ray diffractograms for the $Fe_{50}Cr_{15}Mo_{14}C_{15}B_6$ fully amorphous sample and the partially crystalline ones are presented in Figure 3.18 (a). Figure 3.18 (b) corresponds to the DSC curve at a heating rate of 20 K/min used to follow the crystallization process of the sample during annealing. Colors in the diffractograms correspond to the same dot colors in the calorimetry plot.

The X-ray diffraction pattern of the sample as produced, *i.e.* without heat treatment, shows a broad diffuse peak at 43.5°, which is characteristic of the amorphous state. This feature is also observed at the same angle in the sample treated near to the glass transition temperature at 550° C, where no crystalline peaks develop. However, the reduction of the mean width of the first diffraction peak, as in this case, is related to the structural relaxation due to the annealing process close to the glass transition. Strong signals of a crystalline phase appear in the sample treated at 610° C. This temperature corresponds to the inset of the first crystallization temperature. According to the XRD database used, this formed former phase corresponds to the $M_{23}C_6$ carbide with M = Fe, Cr. Later, by atom probe tomography, it will be demonstrated that the boron present in the

alloy partially replaces carbon to form the phase $M_{23}(C,B)_6$ instead of a pure carbide. This phase continues to develop and more and stronger signals of the $M_{23}C_6$ carbide are evident at 620° C and 650° C. The second crystalline signatures appear near to the inset of the second crystallization temperature at 670° C. These signals correspond to a Mo-rich carbide of the form η-Fe_3Mo_3C, refered as M_6C in the rest of this manuscript. This new carbide and the initial one continue developing until 800° C where the crystallization process is almost finished.

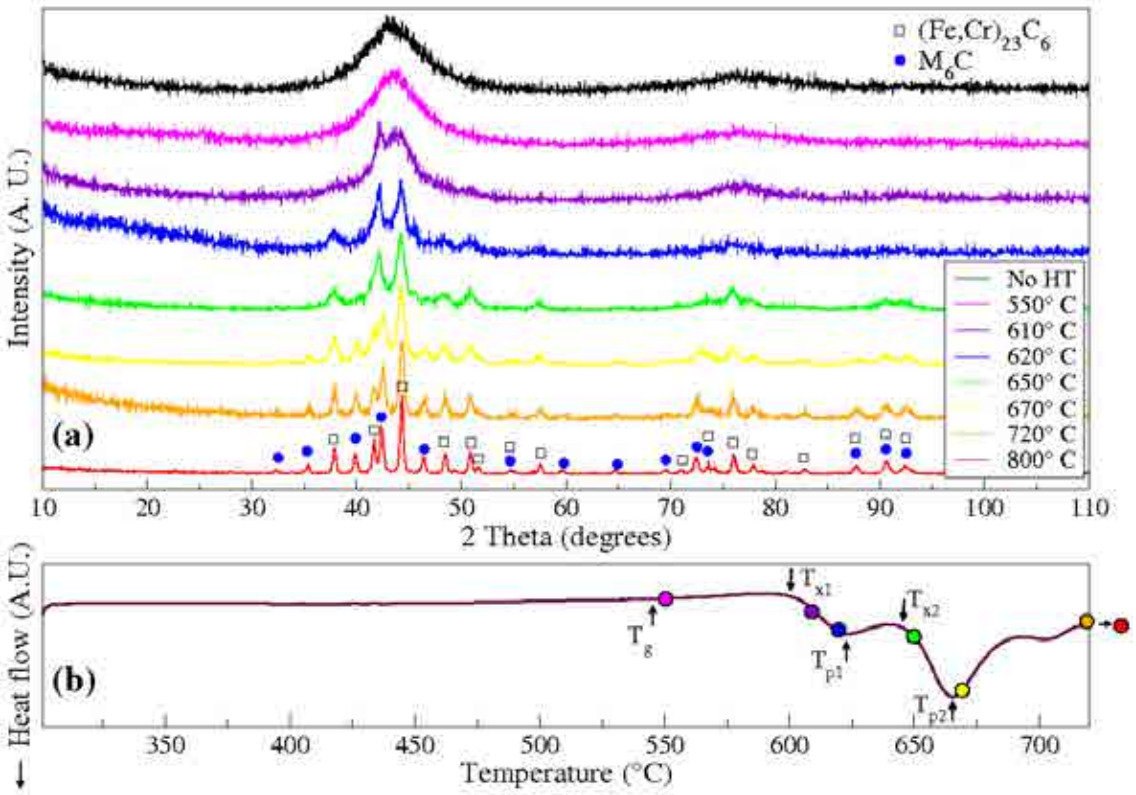

Figure 3.18: X-ray diffractograms of the annealed samples of $Fe_{50}Cr_{15}Mo_{14}C_{15}B_6$ (a), and DSC analysis of the sample as produced (b).

A negligible fraction of amorphous phase still remains after annealing during 20 min at the highest temperature studied, as can be observed in Figure 3.19. One more sample was then annealed at this same temperature during 60 min. As the annealing time increases from 20 min to 60 min the crystalline signals appear stronger and more defined,

which indicates that the process was not complete in 20 min and longer annealing times are needed to stabilize the forming crystals.

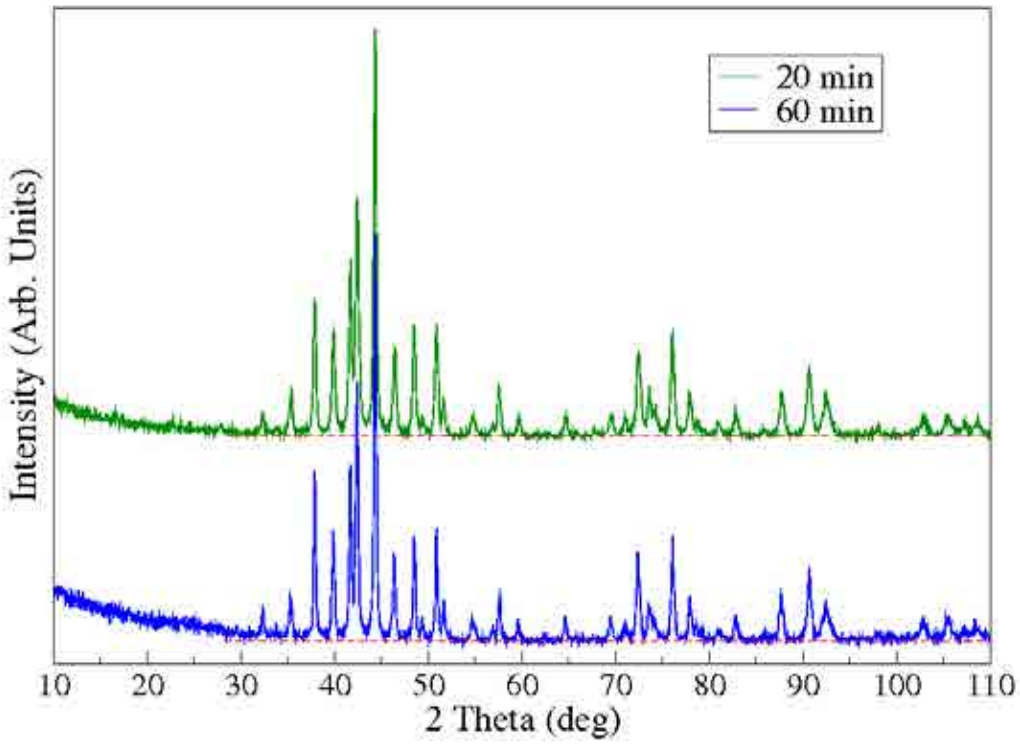

Figure 3.19: X-ray diffractograms comparison of the annealed samples of $Fe_{50}Cr_{15}Mo_{14}C_{15}B_6$ at 800° C during 20 min and 60 min.

The crystalline fraction was estimated by integration of the area under the curves. In summary, the estimated crystalline fraction corresponds to the area of the crystalline signals (sharp peaks) divided by the total area (amorphous plus crystalline signals). The crystalline fractions obtained by this process and the main peak position at the different annealing temperatures are presented in Table 3.10 and Figure 3.20. As the annealing temperature increases a shift of the main diffraction peak to a higher angle in the 2θ plot of the diffracted signals is observed. This shift corresponds to a more compact structure according to Bragg's law. Almost complete crystallization is observed at 800° C and we will refer to this last state as the fully crystalline one for further references in this work.

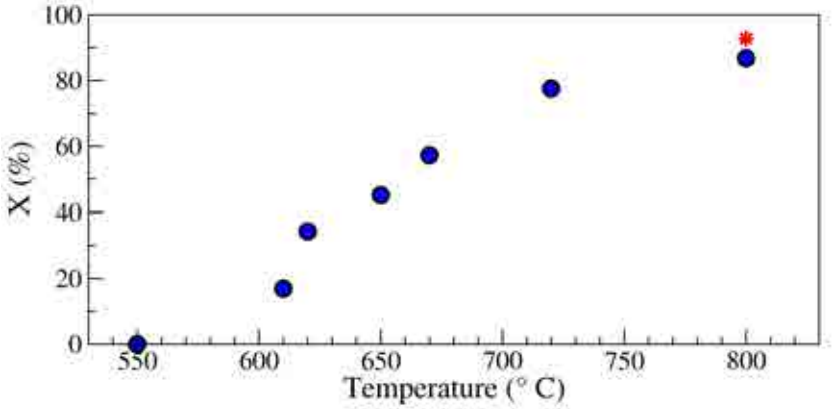

Figure 3.20: Crystalline fraction obtained after annealing at the different temperatures selected.

Table 3.10: Crystalline fraction and main peak position data obtained at the different annealing temperatures.

Annealing temperature (°C)	Crystalline fraction (%)	Main peak position (degrees)
0	0	43.5
550	0	43.5
610	16.9	43.8
620	34.3	44.2
650	45.1	44.2
670	57.2	44.2
720	77.6	44.3
800	86.8	44.3
800 (60 min)	92.8	44.3

As a first approach of the samples structure, SEM images of the sample surface were taken using an InLens detector. Even if the main signals correspond to secondary electrons, the InLens detector also provide hints on the chemical inhomogeneities related to differences in the atomic number due to Z-contrast. Therefore, elements with higher atomic number are observed in lighter regions and on the contrary, elements of lower atomic number are present in darker areas. In general, the as produced samples show a

smooth surface in the front side while the back side presents a rougher surface, as it is observed in Figure 3.21 left and right, respectively. In addition, copper contamination due to the wheel contact during the melt-spinning process may appear in the back side as it was observed by energy dispersive X-ray spectroscopy (EDX) during SEM imaging. In consequence, in order to obtain more reproducible and reliable results, for further studies only the front side is considered.

Clear areas that presumably correspond to the M_6C carbides are observed since the first crystallization stage at 610°C and then continue growing when temperature is increased, see Figure 3.22. However, although the heat treatments were performed in inert atmosphere, a superficial oxide layer was detected by EDX, and the SEM images correspond to this oxide layer. The nature of these oxides is evaluated later by Scanning Auger Spectroscopy due to the layer thickness, usually few nanometers, and the limited resolution of EDX. After partial crystallization and complete crystallization the alloy becomes brittle. Therefore, combined with the ribbons thickness the brittle structure of devitrified samples render mechanical polishing an inappropriate technique to eliminate these oxides and plasma ion-milling process with Ar ions was used instead when necessary.

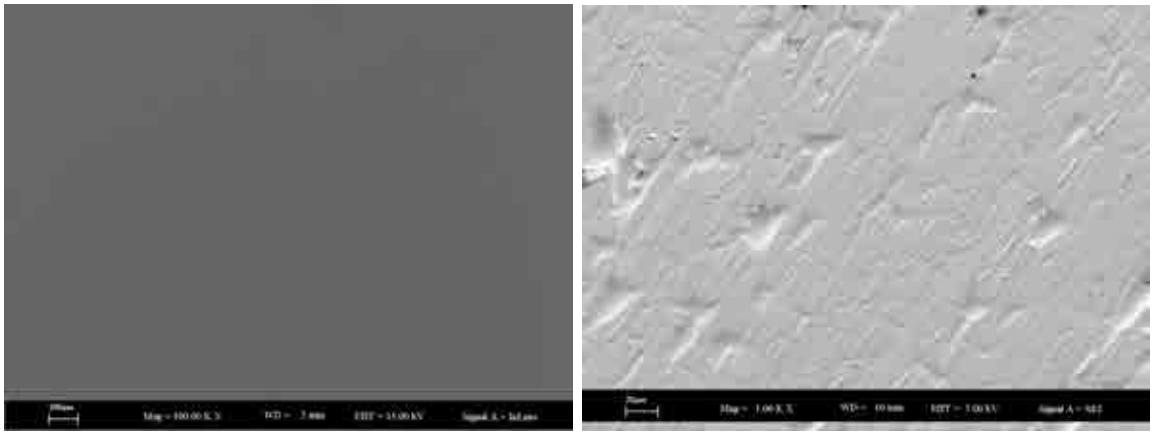

Figure 3.21: SEM micrographs of the $Fe_{50}Cr_{15}Mo_{14}C_{15}B_6$ ribbons as produced (left) front side (right) back side.

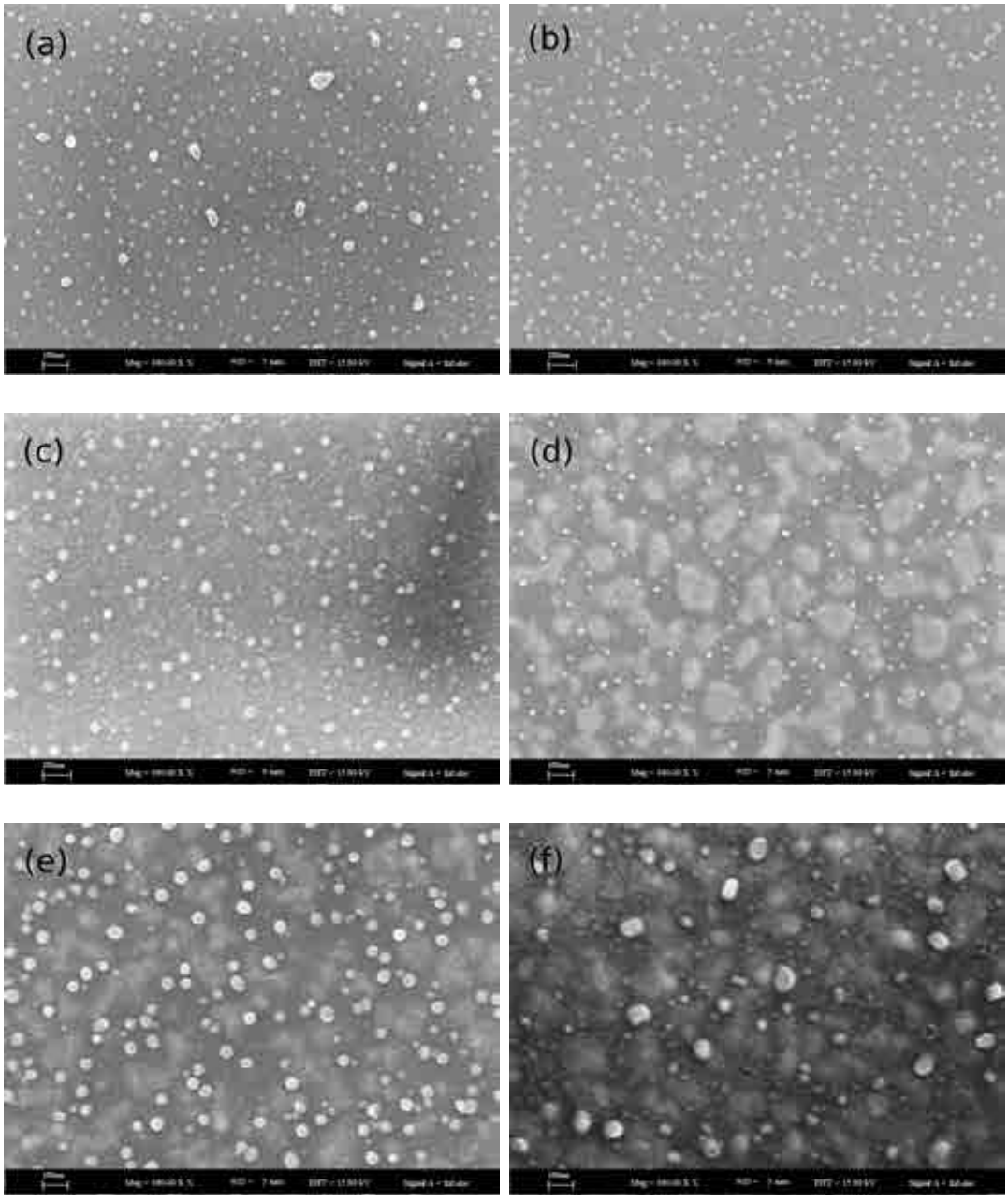

Figure 3.22: SEM micrographs of the $Fe_{50}Cr_{15}Mo_{14}C_{15}B_6$ ribbons annealed during 20min at (a) 550°C, (b) 610°C, (c) 620°C, (d) 670°C, (e) 720°C and (f) 800°C.

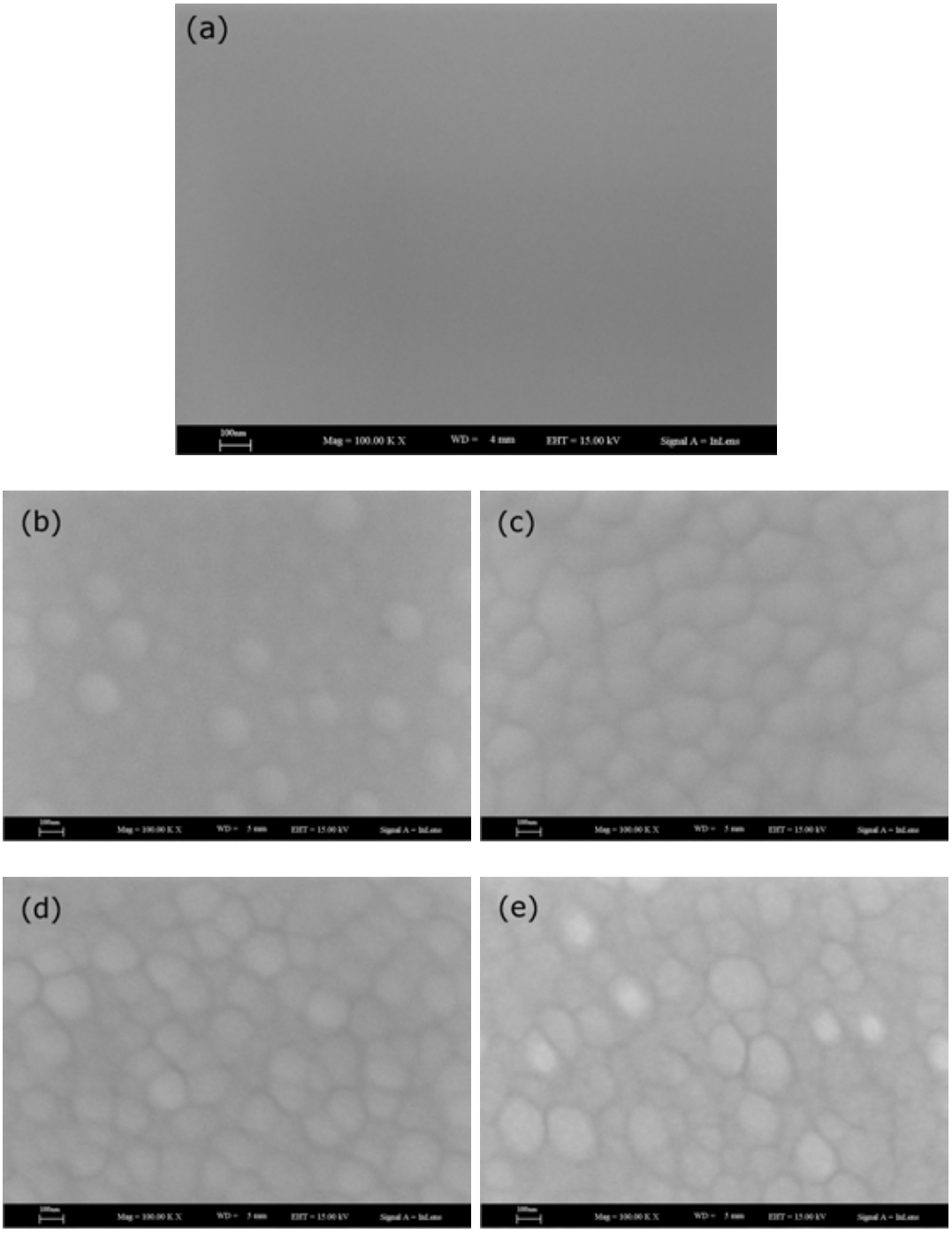

Figure 3.23: SEM micrographs of the $Fe_{50}Cr_{15}Mo_{14}C_{15}B_6$ ribbons after 5 min of ion milling (a) as-produced (b) annealed during 20min at 550°C, (c) 670°C, (d) 720°C and (e) 800°C.

After the ion milling process, Figure 3.23 (a), the as-produced sample shows anew a smooth surface and no signals of chemical or structural homogeneity. However, selective etching is observed for the alloys annealed at any temperature, which is an indication of changes in the microstructure and chemical segregation, since not all different phases can be milled at the same rate. The still amorphous sample annealded close to the glass transition, shows already this selective milling, Figure 3.23 (b). However, this is not homogeneous over all the surface, and still smooth regions can be perceived. This effect becomes stronger in the partially and fully crystallized alloys, Figure 3.23 (c,d,e).

It is evident that after annealing, a nanometer-sized structure evolves from the amorphous matrix. Chemical characterization is important for understanding the mechanisms of the microstructure evolution during crystallization. Conventional analytical techniques such as energy dispersive X-ray spectroscopy (EDX) are unable to resolve chemical composition for nanometersized features or phases immersed in the matrix. X-ray diffraction at that scale provides information of all phases found as a whole, while it is not possible to identify which areas correspond to each one of the found phases. On this stage, Scanning Auger Microscopy (SAM) becomes a very useful technique which enables images of the elements in the near surface layer and chemical composition with a magnification up to 50 kX corresponding to a lateral resolution below 10 nm.

SAM maps were taken at two different distances from the surface of the fully crystalline $Fe_{50}Cr_{15}Mo_{14}C_{15}B_6$ alloy (annealed at 800°C during 20 min). The first results correspond to the native oxide surface of the sample, after only sputter cleaning. The second maps were taken after removing a surface layer of approximately 300 nm by sputtering with Ar ions. The maps show the distribution of the individual elements Fe, Cr, Mo, C, B, N and O in the alloy. Brighter contrast indicates higher concentration of the element in the analyzed area. In addition, SAM enables the determination of light non-metallic elements such as C, N and O. Though B determination is not easy as its signal overlaps with low energy signals of Mo.

The area analyzed by Auger microscopy is shown in the SEM image of Fig. 3.24. This area corresponds to the native surface after cleaning. SAM maps of the metallic elements (Fe, Cr and Mo) present in the alloy show a heterogeneous distribution of

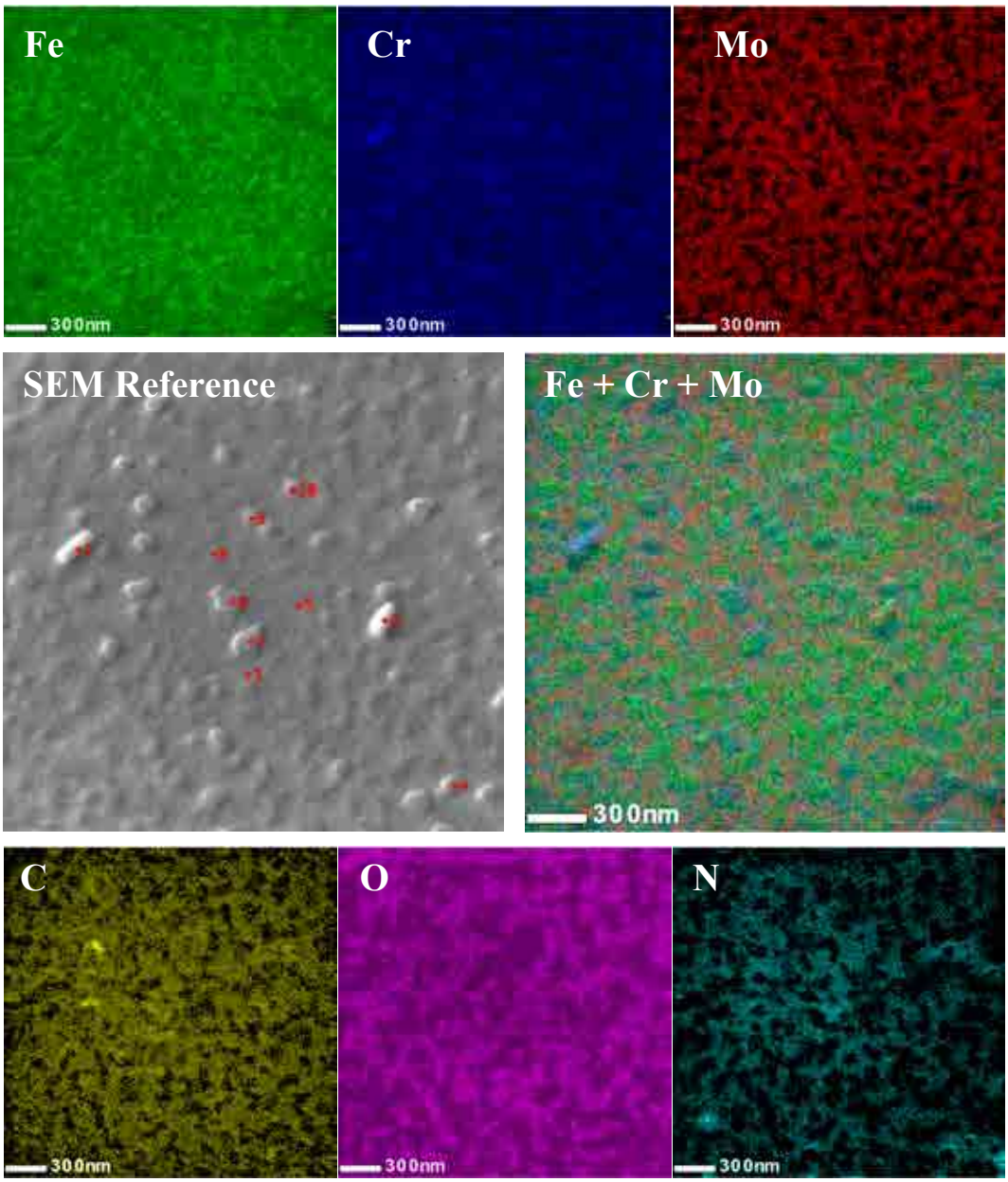

Figure 3.24: SAM maps of the crystallized $Fe_{50}Cr_{15}Mo_{14}C_{15}B_6$ alloy (800° C during 20 min) after cleaning (*i.e.* native surface). *Upper panels*: metallic elements in the alloy. *Left central panel*: SEM Reference image (red numbers represent specific zones where Auger scans were taken). *Right central panel*: Distribution of the three metallic elements on the surface. *Lower panels*: non-metallic elements found on the surface.

these elements on the surface. Moreover, a correspondence is observed between iron and chromium, while molybdenum forms small Mo-rich islands as observed when the three different maps overlay (Fe+Cr+Mo). A large amount of oxygen was also found on the ribbons surface that agrees with the native oxide layer formed after air exposure of the samples. Nitrogen in a small concentration is also observed on the surface after heat treatment.

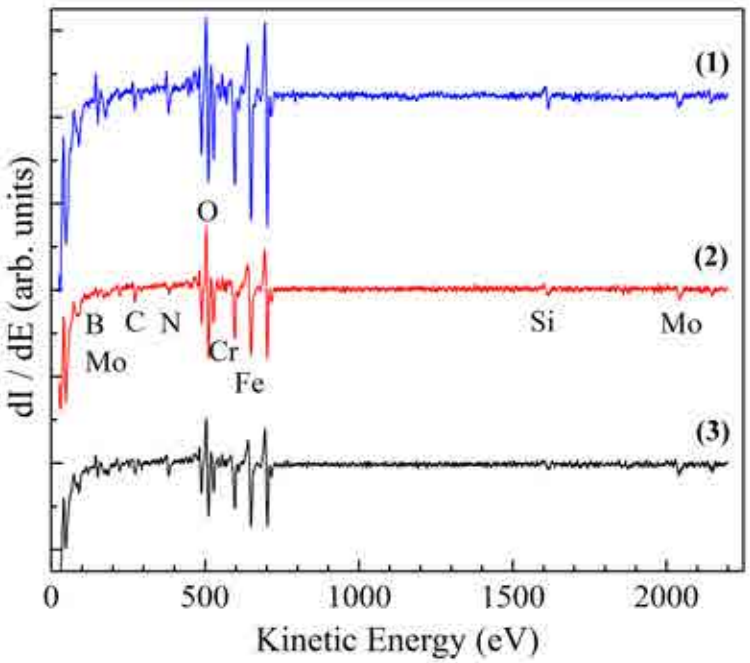

Figure 3.25: Auger scans showing differences in composition of the phases and particles of the native surface of the crystallized $Fe_{50}Cr_{15}Mo_{14}C_{15}B_6$ alloy. (1) brighter particles, (2) darker regions and (3) regions in high relief for SEM Reference in Figure 3.24.

Auger scans were recorded at different positions on the sample surface. Locations of the Auger scans are indicated with red dots in the SEM image. The differences on the scans recorded are summarized in Figure 3.25. The scan referred as (1) corresponds to the brighter particles (+1 and +2 in Figure 3.24), (2) to the darker regions with low relief (+3, +5, +8), and (3) to the grey "particles"with high relief (+6, +7, +4). Some of the stronger Auger electron energies for transitions of the different elements found in the alloy are shown in Table 3.11, taken from [91]. Moreover, the shape of the signatures corresponding to Fe and Cr, agree with those of iron and chromium oxides.

Table 3.11: Main Auger signals for the elements present in the $Fe_{50}Cr_{15}Mo_{14}C_{15}B_6$ alloy (data taken from [91]).

Element	Energy (eV)	Transition	Chemical Bonding	Element	Energy (eV)	Transition	Chemical Bonding
Fe LMM	591.6	L2,3 M2,3 M2,3	Fe^0	Mo LMM	2030.5	L3 M4,5 M4,5	MoOx
Fe LMM	651.6	L2,3 M2,3 M4,5	Fe^0	Mo LMM	2038.8	L3 M4,5 M4,5	Mo^0
Fe LMM	703	L M M	FeCr	Mo LMM	2039	L3 M4,5 M4,5	$MoSi_2$
Fe LMM	703.1	L3 M4,5 M4,5	Fe^0	Mo MVV	2039.2	M V V	$MoSi_2$
Fe LVV	702	L3 V V	Fe_2O_3	Mo MVV	2039.6	M V V	$MoSi_x$
Fe LVV	702.4	L3 V V	Fe^0	Mo MVV	222.8	M4,5 V V	Mo^0
Fe LVV	703.1	L3 V V	Fe_2O_3	B KLL	181.6	K L2,3 L2,3	FeB
Cr LMM	484.2	L M M	Cr_2O_3	B KLL	182.6	K L2,3 L2,3	Fe_2B
Cr LMM	485.7	L M M	Cr^0	N KLL	380	K L L	SiNx
Cr LMM	528	L M M	FeCr	O KLL	503	K L L	FeCr
Cr LMV	527.2	L3 M2,3 V	Cr^0	O KVV	506.9	K V V	SiOx
C KLL	265	K L L	C amorph.	Si KLL	1609	K L L	SiOx
C KLL	273	K L L	FeCr	Si KLL	1617.6	K L L	MoSix

Traces of silicon were found in Auger scans. Those correspond to the white particles observed in the SEM image and presented with the number (1) in Auger scans. These particles rich in silicon and oxygen, presumably silicon oxyde, were found only in the sample surface. Two possible sources of silicon may explain its presence on the sample surface: firstly, in order to prepare ribbons, the alloys were melted in quartz crucibles and small quantities of this element may diffuse into the alloy; second, heat treatments were realized inside quartz crucibles and diffusion of silicon to the sample may happen. The thermodynamic and kinetic parameters, 800° C during 20 min (in Ar atmosphere), are not favorable for silicon diffusion during heat treatment. However, small quantities of silicon, below 1 at.% were detected by EDX in preliminary compositional studies by this technique. Therefore, diffusion of silicon to the sample surface is suggested. When scans were performed after removing 300 nm approximately no silicon was detected on the new resurfaced alloy.

The correspondence between the different metallic elements is best visualized in Figure 3.26. In comparison with the other metallic elements, Fe is more homogeneously dispersed over the surface, forming compounds with Cr and Mo. Meanwhile, Mo and Cr distribute in different areas forming Cr-rich zones depleted in Mo and in counterpart,

Mo-rich zones depleted in Cr.

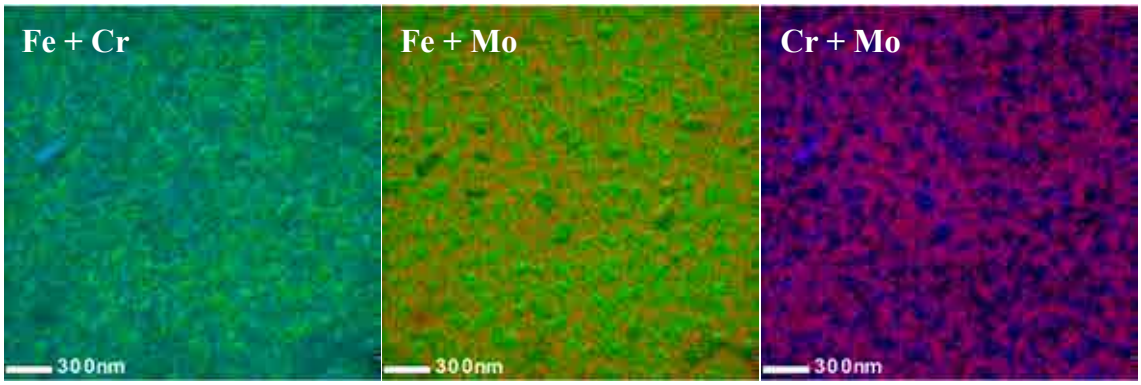

Figure 3.26: Distribution of the metallic elements (SAM maps of the native surface on the crystallized $Fe_{50}Cr_{15}Mo_{14}C_{15}B_6$ alloy).

On the other hand, the non metallic elements found in the surface are presented in Figure 3.27. From these images, formation of oxides is suggested in areas CN-depleted. Correspondence of these two elements with Mo rich areas is also observed.

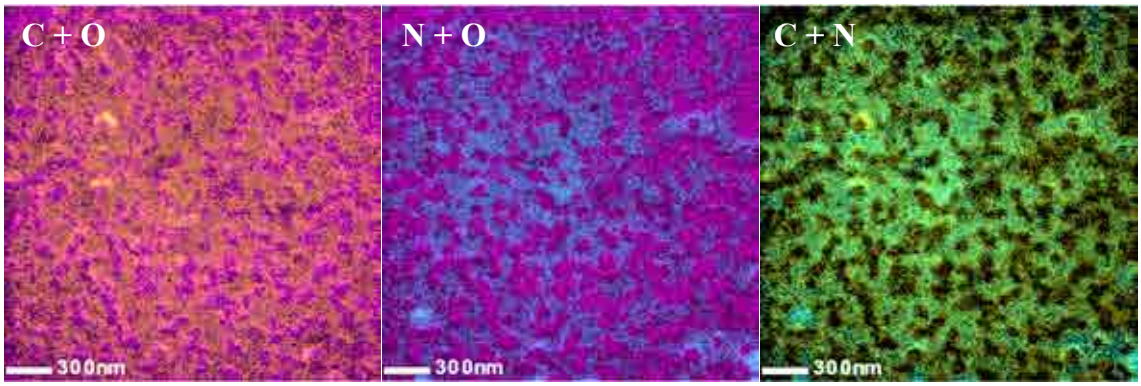

Figure 3.27: Distribution of the non-metallic elements (SAM maps of the native surface on the crystallized $Fe_{50}Cr_{15}Mo_{14}C_{15}B_6$ alloy).

Finally, the formation of Fe and Cr oxides is evidenced in Figure 3.28, where no correspondence of oxygen and Mo is observed. By coupling this observations and the results obtained from the specific scans, is possible to conclude formation of Fe and Cr oxides over the surface, with just a small Mo concentration.

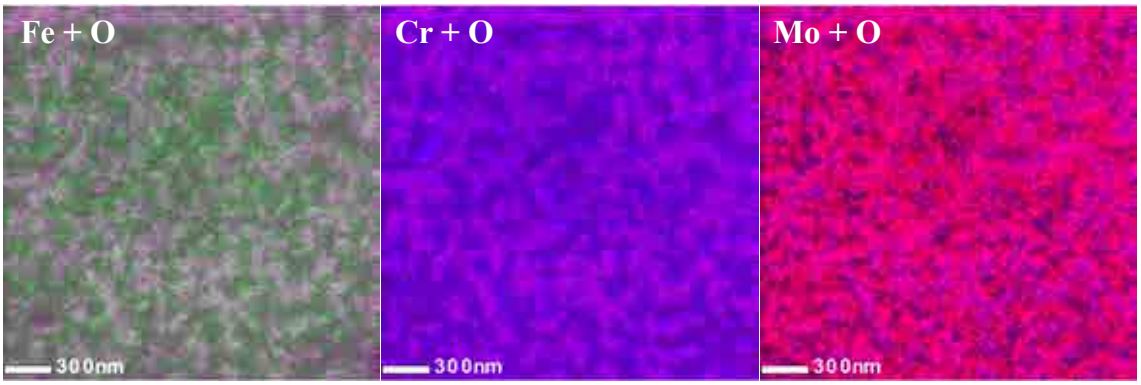

Figure 3.28: Oxygen distribution relative to the metallic elements (SAM maps of the native surface on the crystallized $Fe_{50}Cr_{15}Mo_{14}C_{15}B_6$ alloy).

For a better understanding of the observed behavior, the role of the main elements in commercial stainless steels is outlined below. Chromium is used to improve hardenability, strength and wear resistance. One of the most important Cr effects in steels is the increasing in corrosion resistance at high concentrations (above 12 at.%). It is observed that Cr forms a thin and strong oxide film on the steel surface, protecting it from chemical attacks. Molybdenum on the other hand, increases hardenability and strength as Cr does, but particularly at high temperatures and under dynamic conditions. Mo also forms part of the stabilizing ferrite elements. These elements lower the solubility of carbon in austenite, causing an increase in the amount of carbides in the steel. However, Mo is used in austenitic steels showing an improvement in corrosion resistance. At temperatures from 482° C to 760° C chromium carbides form along the austenite grains. This causes depletion of chromium from the grains resulting in decreasing in the corrosion protective passive film. This effect is called *sensitization*. Formation of chromium carbides may be avoided in stabilized austenitic stainless steels containing forming carbide elements such as titanium, niobium, tantalum, zirconium, tungsten, vanadium or molybdenum. Stabilization heat treatment of such steels results in preferred formation of carbides of the stabilizing elements instead of chromium carbides. In consequence, corrosion resistance is not affected in high carbon steels. Furthermore, carbides formation of these elements leads also to an increase on steels strength and hardness. When nitrogen is introduced in the alloy carbide forming elements also react with the nitrogen present and form nitrides.

From the results observed before in this work, molybdenum may have a similar effect in the present alloy than in conventional steels by forming carbides and nitrides that allow chromium to act as passivating agent. Taking into account the results above, it is possible to recognize that the passivated surface of the $Fe_{50}Cr_{15}Mo_{14}C_{15}B_6$ alloy after crystallization is mainly composed by chromium and iron oxides. However molybdenum carbides and nitrides in smaller concentration were also observed. These carbides and nitrides may stabilize the passive film allowing the formation of chromium oxides.

The superficial oxide layer was then removed in order to asses the bulk structure of the alloy after devitrification. Figure 3.30 shows a SAM map of the fully-crystalline sample surface, annealed at 800° during 20 min, after removing a nominal surface layer of 300 nm by sputtering. Heterogeneous atomic distribution of the metallic elements is observed. Formation of Mo-rich areas is evidenced when the three maps overlap. A correspondence between the metallic elements after crystallization is presented in Figure 3.29. Formation of Fe and Cr rich zones and Mo rich areas is confirmed once again.

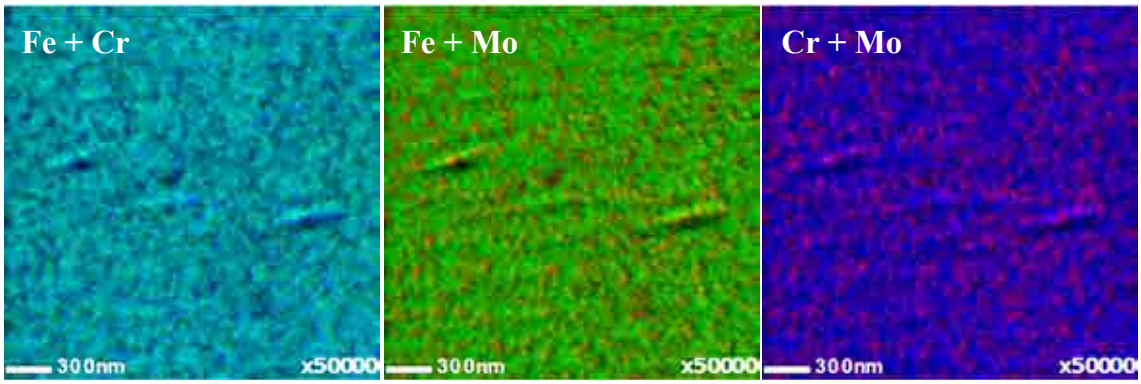

Figure 3.29: Distribution of the metallic elements (SAM maps of the crystallized $Fe_{50}Cr_{15}Mo_{14}C_{15}B_6$ alloy after sputtering of 300 nm.

By summarizing all the results obtained before, one can conclude that the surface shows 10-30 nm large Mo-rich inclusions in a Fe-Cr rich matrix. In agreement with the Auger scans, it is possible to confirm the presence of Mo-rich islands, embedded in FeCr-rich zones depleted in Mo. By correlating with X-ray diffractograms, it is inferred that the FeCr-rich zones correspond to the $M_{23}C_6$ carbide and the Mo-rich particles to the M_6C phase.

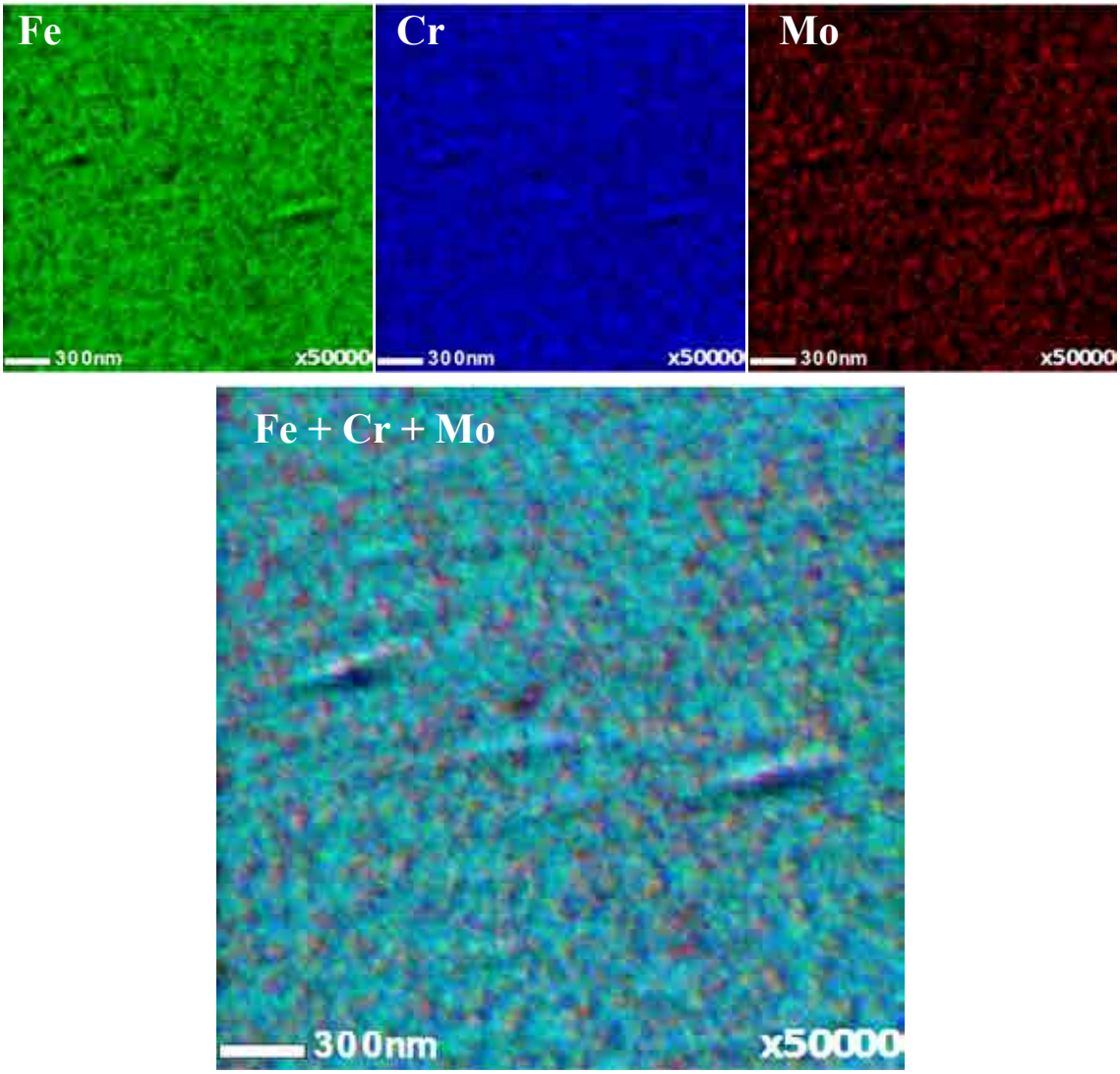

Figure 3.30: SAM maps of the crystallized $Fe_{50}Cr_{15}Mo_{14}C_{15}B_6$ alloy (800° C during 20 min) after sputtering 300 nm. *Upper panels*: metallic elements present in the alloy. *Lower panel*: Distribution of the three metallic elements.

As explained in the Methodology section, thermodynamical calculations were performed by using the database *TCFE5* and the R version of ThermoCalc. Six stable phases in the 600 – 800° C temperature range were found as shown in Figure 3.31. Among these phases, the $M_{23}C_6$ carbide is stable over all the temperature range, being the most important of the encountered phases. M_6C phase appears at 793° C. It is important to emphasize that the results obtained by this method correspond to stable phases in a crystalline structure and metallic glasses are metastable structures susceptible to changes in function of the temperature. Therefore, it is expected that the phases observed experimentally do not correspond to all phases predicted by ThermoCalc and that the calculated compositions are not exactly the same.

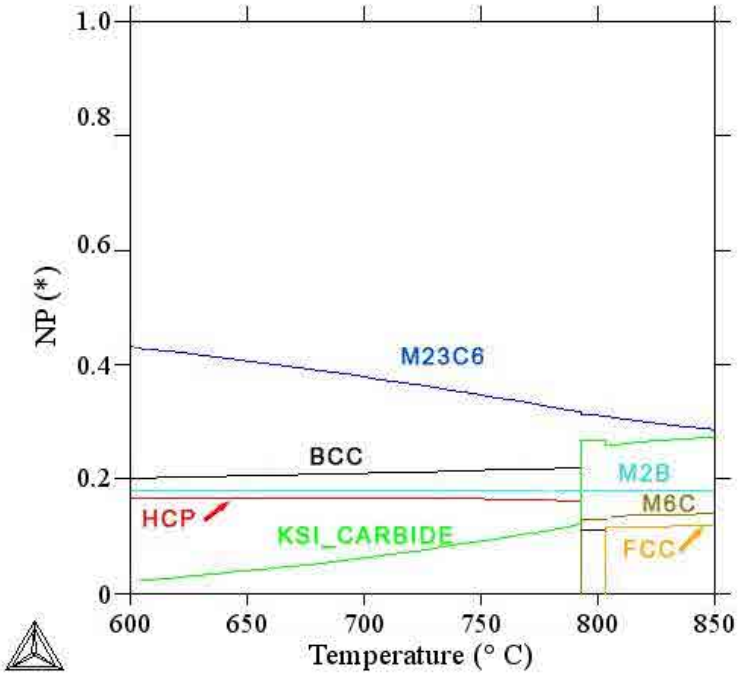

Figure 3.31: Phase distribution predicted with ThermoCalc of a crystalline alloy with the $Fe_{50}Cr_{15}Mo_{14}C_{15}B_6$ composition.

Compositions calculated by ThermoCalc were compared with the experimental data obtained by atom probe tomography. Specific concentrations for the two main carbides

detected by XRD were calculated from ThermoCalc as shown in Figure 3.32. Calculations show that C concentration remain stable over all temperature range for the $M_{23}C_6$ carbide and presence of B is not considered. Cr, Fe and Mo concentrations slightly varies as the temperature increases. Similar to $M_{23}C_6$, M_6C shows a stable concentration of C and no presence of B in all the temperature range analyzed. Changes in Mo and Fe concentration are sharper with increasing temperature for this carbide. Specific compositions obtained from this calculations at the different annealing temperatures are presented in Tables 3.14 and 3.16 and are compared with atom probe data of compositional analysis.

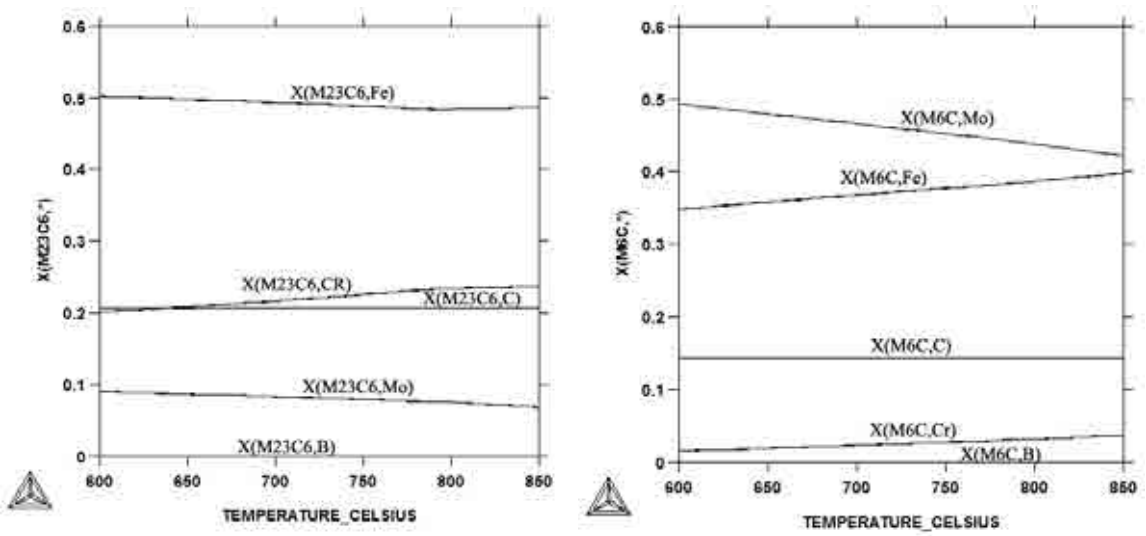

Figure 3.32: Predicted chemical composition of the main carbides formed: (a) $M_{23}C_6$, and (b) M_6C.

Other useful technique that allows sampling atoms from the nanoparticles formed as well as the atoms remaining in the matrix by means of using the field evaporation phenomena is atom probe tomography (APT). The use of this complementary technique with the previous ones allows to resolve lateral composition of the sample surface (SAM) and internal microstructure with atomic resolution (APT). Microstructural and compositional changes of the $Fe_{50}Cr_{15}Mo_{14}C_{15}B_6$ alloy upon crystallization observed with this last technique are presented below. Figure 3.33 shows a general overview of the different reconstructions obtained by APT used for microstructural and chemical analysis.

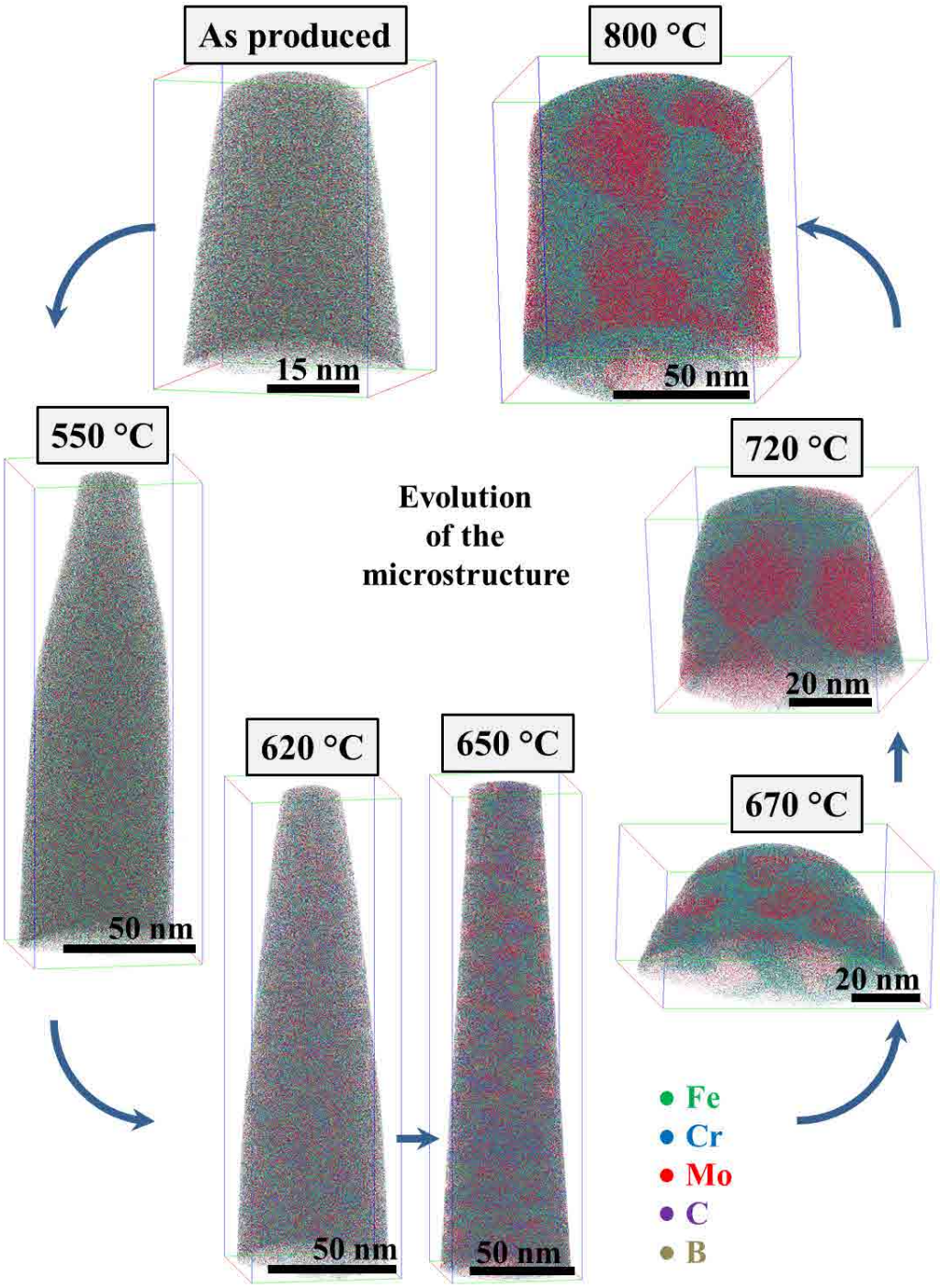

Figure 3.33: Evolution of the microstructure of the $Fe_{50}Cr_{15}Mo_{14}C_{15}B_6$ metallic glass upon devitrification followed by atom probe tomography.

Chemical composition of the as produced alloy is close to the nominal composition as observed in Table 3.12. Concentrations of each element correspond to the average value over all the measurements of the *as produced and the heat treated samples*. Differences with respect to the nominal composition may be related with the small volume analyzed (approximately 4×10^{-5} nm^3) and differences on the evaporation rate of every type of atoms. Compositions of the Mo-rich particles and the Cr-Fe enriched zones are presented separately for each annealing temperature.

Table 3.12: General composition obtained by APT of the $Fe_{50}Cr_{15}Mo_{14}C_{15}B_6$ amorphous alloy.

Element	Fe	Cr	Mo	C	B
Concentration (at. %)	48.04	15.15	16.64	13.62	5.52
Standard deviation	2.38	0.67	0.77	1.28	1.07

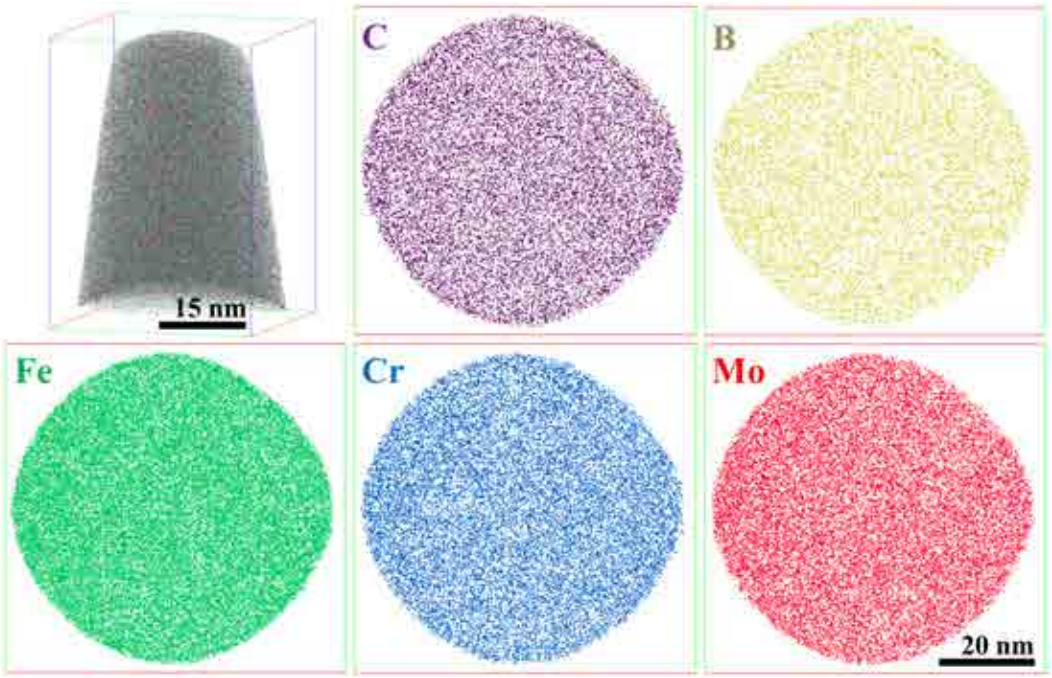

Figure 3.34: z-projection of a 3nm disc cut from the as-produced (amorphous) sample showing composition homogeneity.

Distribution analysis (as explained in Section 3.2) for each element at the amorphous state and the samples annealed near to the glass transition temperature (550° C) are presented in Figure 3.35, where the main data has been extracted and reported in Table 3.13. Small χ^2 values as in the as-produced sample indicate a small deviation of the observed behavior with respect to the calculated binomial distribution. This result suggest that the as-produced sample has a homogeneous composition with uniformly distributed elements, as it is also observed in Figure 3.34. Although significant P-values as in the case of Fe and C, were P <0.05, show a small deviation of the predicted behavior, this result may be explained by the preferential evaporation rate of these atoms in between the evaporation pulses which at the end are detected as noise. Therefore, the homogeneity over all the samples for the fully amorphous state is confirmed once more with this technique.

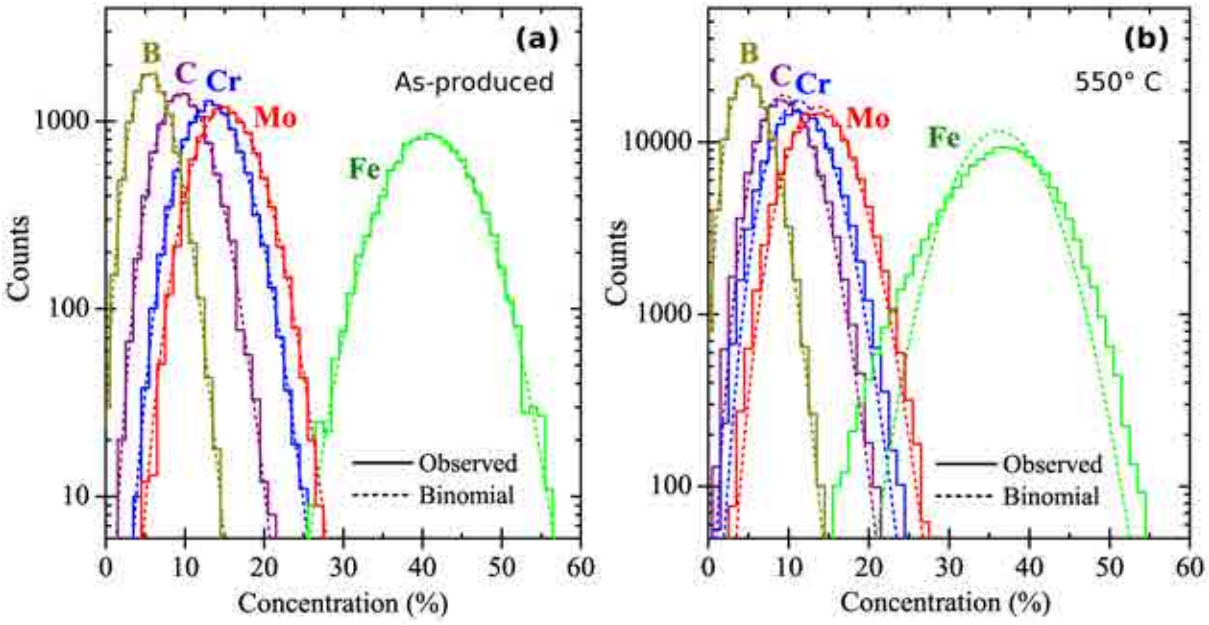

Figure 3.35: Distribution analysis of every element in the $Fe_{50}Cr_{15}Mo_{14}C_{15}B_6$ alloy: (a) as produced, and (b) annealed at 550° C.

Annealing at 550° C during 20 min generates deviation of the calculated binomial distribution. All χ^2 values correspond to highly significant P-values, which is an indication

Table 3.13: Parameters obtained from the distribution analysis of the $Fe_{50}Cr_{15}Mo_{14}C_{15}B_6$ MGs as produced and annealed at 550° C.

	As-produced				550° C			
Element	Reduced χ^2	n_d	P-value	μ	Reduced χ^2	n_d	P-value	μ
Fe	1.533	33	0.0257	0.0690	45.311	34	<0.0001	0.2470
Cr	1.043	21	0.4047	0.0455	19.321	22	<0.0001	0.1327
Mo	0.791	23	0.7463	0.0414	3.677	24	<0.0001	0.0609
C	1.608	19	0.0451	0.0537	7.465	21	<0.0001	0.0810
B	1.061	15	0.3875	0.0388	1.788	15	<0.0001	0.0336

of the heterogeneity of the alloy. By XRD as in Figure 3.18, it was observed that no signs of crystallization appear at this temperature. Nevertheless, by APT atomic arrangement is observed and diffusion of forming atoms of the first stable carbide is suggested. The most significant χ^2 values correspond to Fe and Cr, and finally C in minor extent. These elements are the main constituents of the $M_{23}C_6$ phase which allude to the first insight of a new phase formation. This observation is in agreement with the results reported for a similar composition with 2 at.% yttrium [92]. As the annealing temperature rises above 550° C, distribution analysis are no longer reported in this work. The evolution of a heterogeneous microstructure upon annealing leads to a rise in χ^2 and the consequent shift of P-values much lower than 0.05, which was set as the upper limit for significant values.

When the temperature reaches 610° C the first signs of crystallization are revealed by X-ray diffraction. Heterogeneity in the distribution analysis is increased as expected. Diffusion of elements to form FeCr-rich zones depleted in Mo appear at small scale. At 620° C atomic redistribution to form FeCr-rich areas is more visible. As a consequence, Fe and Cr depleted zones are formed where Mo concentration appears to increase. In addition to these two major phases, cluster analysis shows formation of chromium clustering at this temperature. These clusters have a high concentration of Cr above 55 at.% with different amounts of all the other elements. Cr clusters of less than 5 nm randomly distributed through the sample were observed. These observations were pointed out in the Master Thesis of Jingfei Chu.

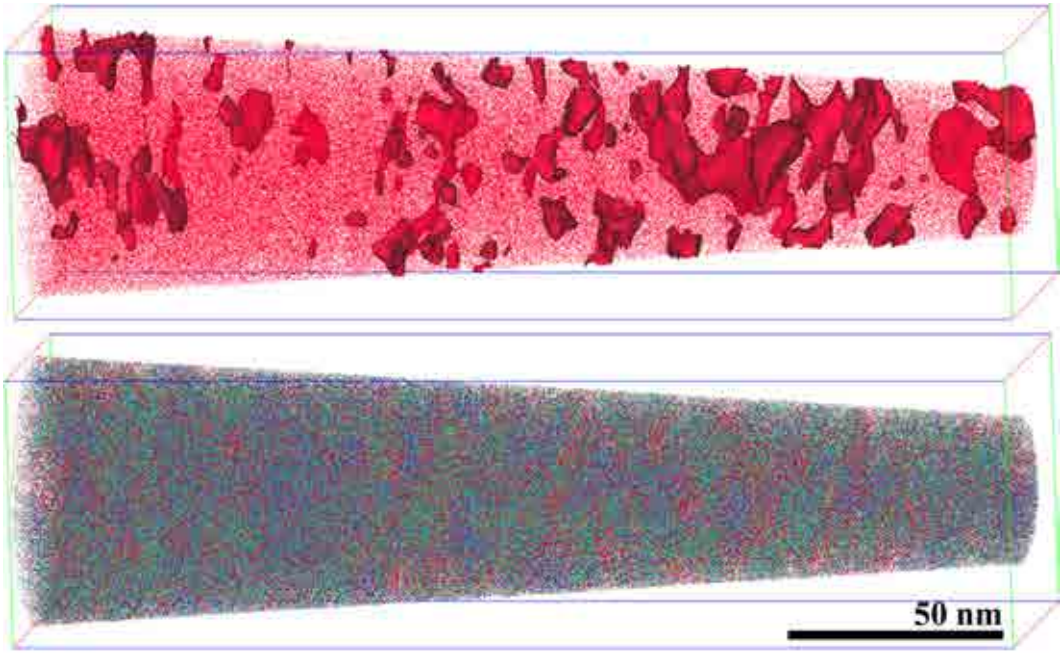

Figure 3.36: (*up*) 3D atomic map of Mo atoms plus31 at.% Mo iso-concentration surface of the partially crystallized alloy annealed at 650° C during 20 min. (*down*) 3D atomic map of all the elements in the alloy.

At the second crystallization temperature, near to 650° C the evolution of Mo-rich areas is confirmed. In the lower panel in Figure 3.36 where all the atoms in the alloy are plotted, is possible to observe that Mo-rich (in red) regions and Cr-rich (in blue) regions emerge from the reconstruction. For clarity, in the upper pannel Mo atoms and an iso-concentration surface of 31 at.% Mo are plotted. Mo-rich zones of 10-20 nm diameter, that are homogeneously distributed over all the sample, are observed. The composition corresponding to these regions is summarized in Table 3.16.

The size and number of these Mo-rich areas increase as the temperature rises up to a complete crystallization. Examples of these molybdenum rich particles are presented in Figure 3.37. In the figure, Cr atoms are represented in blue color. 31 at.% Mo iso-concentration surfaces plotted in red color enclose Mo-rich particles of 20-30 nm diameter. These regions are Cr-depleted as it is observed in the same plot. Cr atoms are found

inside the Fe,Cr-rich phases which are enclosed by 45 at. % Fe (for 650° C) and 39 at. % Fe (for 720° C) iso-concentration surfaces.

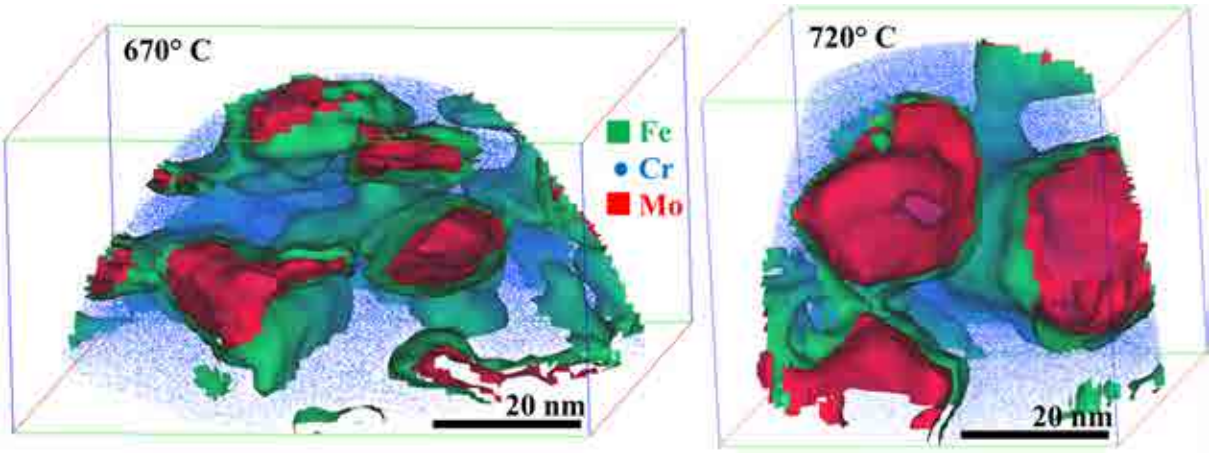

Figure 3.37: 31 at.% Mo iso-concentration surfaces (in red) and 45 at.% Fe (left) and 39 at.% Fe (right) iso-concentration surfaces (in green) and Cr atoms (blue dots) of the partially crystallized $Fe_{50}Cr_{15}Mo_{14}C_{15}B_6$ alloy annealed during 20 min at: (left) 670° C and (right) 720° C.

As the annealing temperature increases, Mo-rich and FeCr-rich areas approach to the equilibrium composition forming a fully nanocrystalline structure. A 2D plot of the $Fe_{50}Cr_{15}Mo_{14}C_{15}B_6$ alloy annealed at 800° C during 60 min is presented in Figure 3.38 where only metallic atoms are shown. Mo and Cr correspond to the blue and red dots, respectively. An iso-concentration surface of 31 at.% Mo is plotted in red, while the blue iso-concentration surface corresponds to 16 at. % Cr. The plotted iso-surfaces perfectly delimit the boundaries between two phases completely different in composition, more precisely, a Mo-rich phase and a Fe,Cr-rich phase. The size of the formed regions ranges between 10 to 50 nm. The chemical composition of these two main phases formed in the $Fe_{50}Cr_{15}Mo_{14}C_{15}B_6$ alloy after devitrification is reported in Tables 3.14 and 3.16. In the Tables, the experimental data correspond to the FeCr-rich and Mo-rich phases obtained by APT. In order to obtain these values, the interfaces between the different phases are created according to the iso-concentration surfaces. The volume inside the interfaces is then extracted and the mass spectrum corresponding to the new Region of

Interest is evaluated. The bulk composition is obtained finally from this last evaluated mass spectrum. The calculated data in the Tables correspond to the values obtained by ThermoCalc for the predicted $M_{23}C_6$ and M_6C carbides, as was explained before.

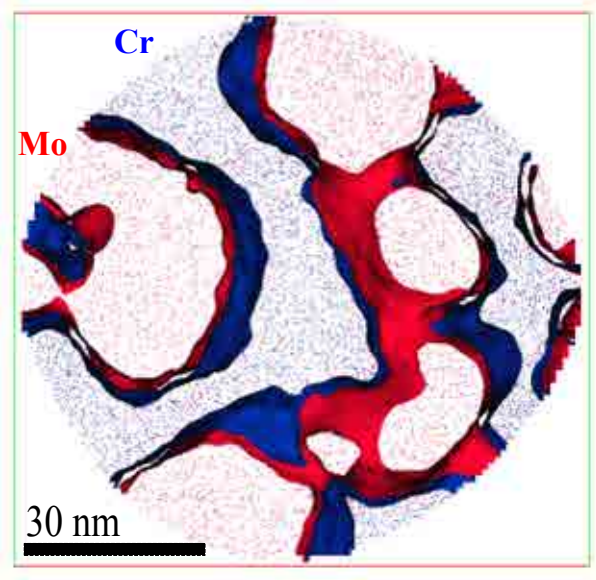

Figure 3.38: Phase separation in the crystallized alloy, annealed at 800° C during 60 min. Cr atoms are plotted in blue while Mo atoms are represented in red. Iso-concentration surfaces highlight the interfaces between the main formed phases: 16 at. % Cr in blue, and 31 at. % Mo in red.

Finally, by combining all the results presented before, some important findings can be highlighted. As predicted by ThermoCalc and XRD, the first carbide formed corresponds to the $M_{23}C_6$ phase, where M = Fe, Cr and Mo in lower concentration. Table 3.14 shows that boron forms part of these carbide in large concentration, even if it was not predicted by other techniques. Moreover, if B concentration is added to C concentration, the final amount is approximately equivalent to the C expected content, these results are shown in Table 3.15. Therefore, it can be concluded that the main formed phase corresponds not only to carbides, but also borides and it has the general composition of $M_{23}(C,B)_6$.

By regarding the experimental composition by APT for the Mo-rich phases, as in Table 3.16, it is possible to follow the specific behavior of the different atoms in the alloy

Table 3.14: Chemical composition of the FeCr-rich phase formed after devitrification. Experimental and calculated data correspond to the results obtained by APT and the $M_{23}C_6$ carbides predicted by ThermoCalc, respectively.

Temperature	Concentration	Fe (at.%)	Cr (at.%)	Mo (at.%)	C (at.%)	B (at.%)
720° C	Experimental	49.77	16.70	13.51	13.31	6.70
	Calculated ($M_{23}C_6$)	49.12	22.04	8.15	20.69	0.00
800° C *	Experimental	53.82	15.13	10.76	13.61	5.67
	Calculated ($M_{23}C_6$)	48.46	23.40	7.45	20.69	0.00

* The annealing time in this case is 60 min.

Table 3.15: Quantification of C and B concentration in the FeCr-rich phases.

Temperature	APT B + C concentration (at.%)	ThermoCalc Predicted C concentration (at.%)
720° C	20.01	20.69
800° C *	19.28	20.69

* The annealing time in this case is 60 min.

Table 3.16: Chemical composition of the Mo-rich phase formed after devitrification. Experimental and calculated data correspond to the results obtained by APT and the M_6C carbides predicted by ThermoCalc, respectively.

Temperature	Concentration	Fe (at.%)	Cr (at.%)	Mo (at.%)	C (at.%)	B (at.%)
650° C	Experimental	32.85	8.67	39.82	15.59	3.06
	Calculated (M_6C)	35.87	1.94	47.91	14.29	0.00
670° C	Experimental	38.81	6.82	33.98	16.75	3.64
	Calculated (M_6C)	36.26	2.10	47.37	14.29	0.00
720° C	Experimental	36.05	6.15	39.38	16.04	2.37
	Calculated (M_6C)	37.21	2.49	46.00	14.28	0.00
800° C *	Experimental	38.43	5.29	40.76	13.96	1.56
	Calculated (M_6C)	38.75	3.22	43.74	14.28	0.00

* The annealing time in this case is 60 min.

upon annealing. Iron shows an increase in concentration as the temperature rises up to 800° C. On the other hand, concentration of molybdenum and carbon remain more or less constant, and finally the amount of boron decreases, when temperature is increased. When these values obtained by APT are compared with the ThermoCalc predicted compositions, a clear trend towards the composition of the predicted phases is observed. The fully crystalline sample (annealed at 800° C during 1hr) exhibit a composition remarkably close to the calculated one. Low concentration of boron in the alloy still remains, nevertheless it corresponds to the lowest boron concentration displayed at the different temperatures. Taking into account all previous considerations it is possible to conclude that the concentration of the Mo-rich phases approaches to the equilibrium M_6C phase as the annealing temperature increases.

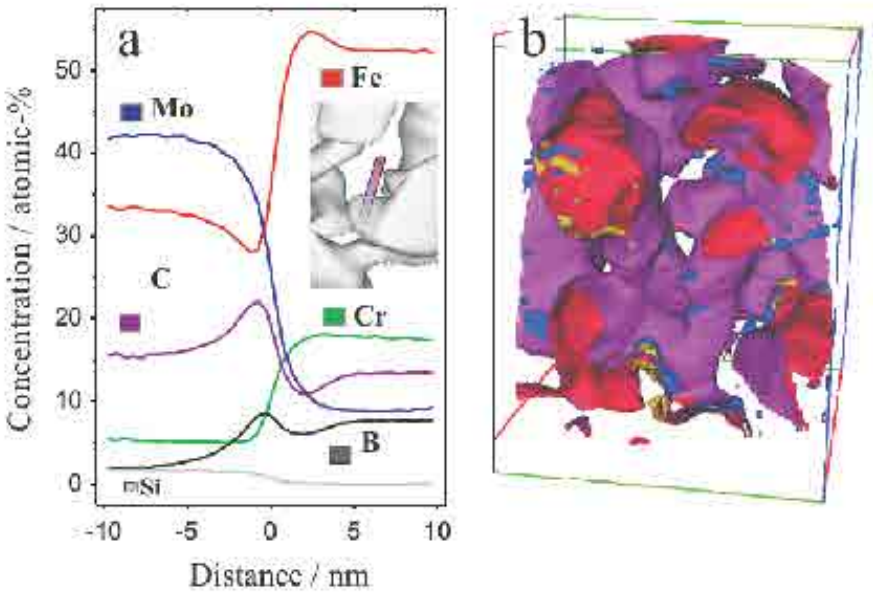

Figure 3.39: (a) One dimension concentration profile over one of the phase boundaries between Mo-rich particles and FeCr-rich zones, and (b) General structure of the crystallized alloy, annealed at 800° C during 60 min: Mo, Fe, C and B isosurfaces correspond to red, purple, blue and yellow colors, respectively.

Figure 3.39 (a) shows atom probe concentration profiles of the $Fe_{50}Cr_{15}Mo_{14}C_{15}B_6$ alloy annealed at 800° C during 60 min. The concentration profile goes through the interphase between two different regions as shown in the inset. Large Mo-rich particles depleted in Fe, Cr and B with respect to the surrounding area are observed. These particles approach to the nominal composition of the M_6C equilibrium phase predicted by ThermoCalc. The corresponding area to FeCr-rich zones displayed the composition of $M_{23}(C,B)_6$ phases, as discussed before. Concentration profiles show C and B enrichment at the Mo / FeCr rich interphase.

Based on all the results presented on the crystallization and the microstructure evolution process in $Fe_{50}Cr_{15}Mo_{14}C_{15}B_6$ alloy upon annealing may be summarized as follows. By XRD and APT, the fully amorphous structure of the as produced alloy was confirmed. Chemical heterogeneity starts in the early stage near to the glass transition temperature. Heterogeneous nucleation comes next with formation of the primary crystals of the form $M_{23}(C,B)_6$. Molybdenum is rejected from these crystals and enriches the amorphous matrix. In the second stage of the crystallization reaction M_6C phase forms in the Mo-rich areas. Both phases continue growing and the final microstructure is composed of M_6C carbides embedded in $M_{23}(C,B)_6$, with C and B enrichment at the interface.

The electrochemical behavior of the fully amorphous samples, the partially devitrified and the fully crystalline ones were analyzed by linear polarization tests in 0.1 M HCl solution at room temperature. These results are plotted in Figure 3.40. All the samples passivate spontaneously and then exhibit different passive to transpassive behavior. The fully amorphous sample shows a large passivation range, of more than 1V, up to transpassive potential, which is an indication of a high corrosion-resistant material. On the other hand, the fully nanocrystalline alloy shows rather a pseudopassive polarization curve and not a typical passivation range. The partially nanocrystalline samples show an intermediate behavior between these both extremes.

Nevertheless, it is important to notice that polarization curves of these intermediate states group near to one of the extremes. For lower annealing temperatures, up to 650° C, where the second crystalline phase just appears, polarization curves present a more anodic behavior, close to the fully amorphous stage. Small deviations showing a

detrimental effect on corrosion behavior with the formation of nanocrystals is observed. Samples annealed above 670° C show polarization curves shifted to the cathodic direction with respect to the fully amorphous sample. They show a behavior close to the fully nanocrystalline state.

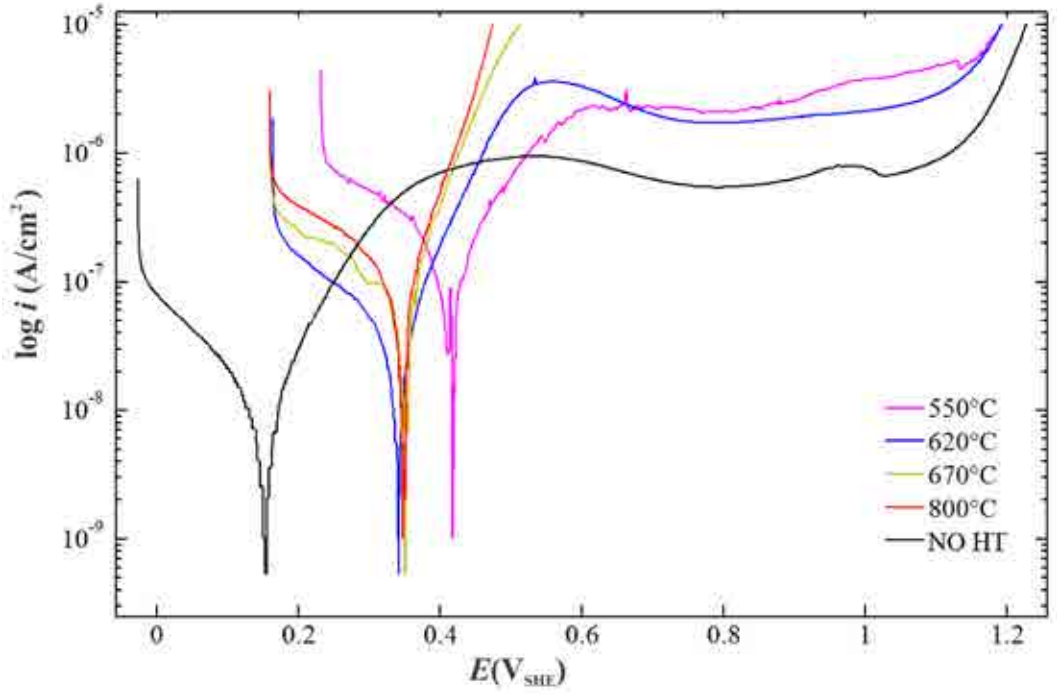

Figure 3.40: Potentiodynamic polarization curves of the fully amorphous, partially devitrified and fully nanocrystalline $Fe_{50}Cr_{15}Mo_{14}C_{15}B_6$ alloys in HCl 0.1 M.

From the obtained results is possible to observe that heat treatments have a detrimental effect on the corrosion resistance of the $Fe_{50}Cr_{15}Mo_{14}C_{15}B_6$ alloy. A large passive range at a very low current density is observed for the fully amorphous alloy and with a low degree of crystallization below 50%. The breakdown potential of these alloys reaches 1.2 V, linked to the transpassive dissolution of Mo, thus showing a highly protective film against acid solutions. As the annealing temperature increases, and the crystalline fraction reaches 50% or more, the curves show a pseudopassive behavior with a breakdown potential near to 0.4 V, three times lower than the fully amorphous state. This macroscopic corrosion behavior is therefore discussed in the basis of the chemistry and the

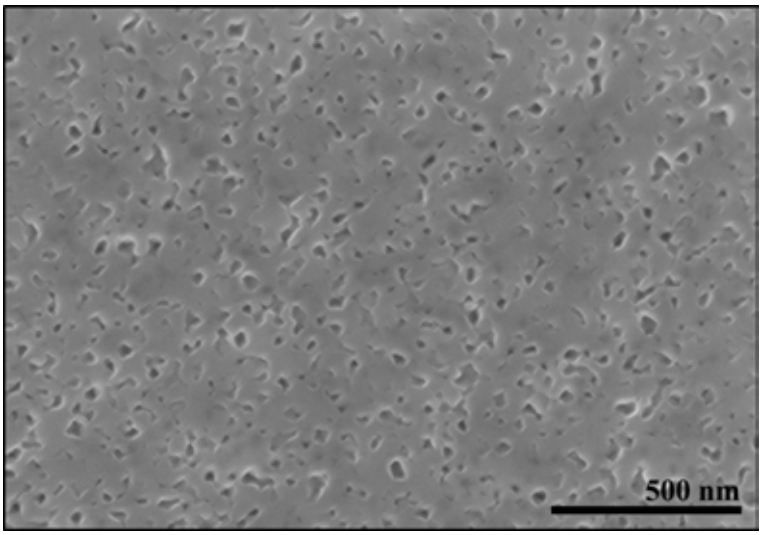

Figure 3.41: SEM image of the fully nanocrystalline $Fe_{50}Cr_{15}Mo_{14}C_{15}B_6$ alloy (annealed 800° C during 20 min) after immersion in a HCl 1 M solution.

structure of the analyzed materials. Phase separation promotes a preferential corrosion process and then an heterogeneous structure will have an unfavorable effect on corrosion resistance. Moreover, dissolution of the less chemically stable phases after crystallization is evidenced after immersion in the acid solution, as shown in Figure 3.41.

The role of Cr in the passive films on Fe-based amorphous alloys has been considered in several works. It has been proposed that formation of a passive chromium oxyhydroxide film leads to a high corrosion resistance of these alloys. This film has the general composition ($CrO_x[OH]_{3-2x} \cdot n$H2O) [77, 93]. Mo would increase corrosion resistance by forming a passive tretravalent molybdenum oxide film in regions where Cr actively dissolves, and suppressing this last effect in consequence [89]. Phase separation and crystallization causes formation of Mo-rich zones with low concentration of Cr that dissolve preferentially as observed in Figure3.41. Additionally, formation of Cr-rich carbides results in chromium depleted zones around them. This could explain the small deviations of the samples annealed at relatively low temperatures from the behavior observed in the amorphous state.

3.3.4 Conclusions

The amorphous nature of the as produced $Fe_{50}Cr_{15}Mo_{14}C_{15}B_6$ alloy is confirmed by XRD, SEM, APT. No signs of chemical heterogeneity in the fully amorphous state were detected. When the sample is annealed at 550° C near to the glass transition temperature (545° C), X-ray diffractograms reveal that the alloy remains amorphous at this stage. Nevertheless, deviation of the observed distribution with respect to the binomial distribution in atom probe results indicates heterogeneity in the composition of the alloy. As in several metallic glasses, crystallization is carried on by nucleation and growth of a primary phase under non-equilibrium conditions from the undercooled liquid state. When the temperature approaches to the onset of the first crystallization temperature at 610° C partial devitrification of the $Fe_{50}Cr_{15}Mo_{14}C_{15}B_6$ alloy causes formation of nanocrystalline carbide phases dispersed in a matrix of the remaining amorphous phase. The combination of AES and APT can link surface properties with detail in morphology and composition. In agreement with the AES result, APT data obtained from a fully-crystallized sample shows Mo-rich and Fe-Cr-rich areas clearly visible. Boron and Carbon segregate to FeCr / Mo interfaces. Devitrification process in this case may be described in a two stage crystallization process, where the first phase heterogeneously nucleates in a primary crystallization reaction to form $M_{23}(C,B)_6$. The final microstructure is composed of M_6C carbides embedded in a $M_{23}(C,B)_6$ phase.

The effects of the microstructure in corrosion behavior were discussed in terms of the chemistry and microstructure of the alloy. The homogeneity in chemistry and structure of the amorphous material provide the alloy with a high corrosion resistance. Heat treatments intended to crystallize the alloy at different stages show a detrimental effect on the corrosion properties. Heterogeneity in composition and formation of Cr-depleted zones lead to dissolution of Mo-rich phases and reduction of the corrosion resistance of the passive film. However, the general resistance of the alloy is not compromised for low annealing temperatures, or crystallization fraction below 50 %. After this threshold value, a severe detriment on the corrosion breakdown due to dissolution of Mo-rich phases, clearly depleted in chromium is promoted.

Chapter 4

Development of Zr-Ti based alloys for biocompatible applications

Materials used for medical purposes should combine appropriate mechanical and structural properties and ideally promote a healing response without causing severe bodily reactions. Titanium and zirconium alloys have proven to possess good agreement of these properties that make them ideal for biomedical applications. In the area of metallic glasses, some Ni-free alloys presenting good biocompatibility have been proposed. However, the addition of some elements intended to increase the GFA such as Ni, Be or Cu are not suitable to be in contact with the human body. Another important issue is that not only biocompatibility but bioactivity of materials is desirable for some medical applications. Surface treatments, are then performed on the material to promote a good interface between the tissue and the introduced material. Furthermore, metallic MgZnCa alloys that could biocorrode have been proposed as biodegradable implants. With all these concepts in mind, in this thesis based on the knowledge of phase diagrams, mixing enthalpies and individual properties of the elements involved, an alloy that contains Zr and Ti was designed for biocompatibility purposes. Ca is added to this alloy to improve glass forming ability. It is expected that the incorporation of calcium as microalloying element will increase also the bioactivity of this new composition.

4.1 Background

Biomedical applications require the design of new biomaterials with specific properties. Materials used in medical devices should have the appropriate mechanical and structural properties and ideally promote a healling response without causing severe bodily reactions. Ti-based alloys are extensively used for biomedical applications for their excellent mechanical properties and biocompatibility [94]. Titanium has proved to be strong, flexible and light weight, absolutely inert in the human body and immune to attack from bodily fluids. Moreover, titanium can also osseointegrate providing longer lasting bonds to tissues and bones. All this properties make titanium ideal for biocompatible alloys. However, surface properties play also an important role in medical devices. Several surface treatments, such as coating or chemical modification have to be used to enhance or modify properties such as lubricity, hydrophobicity, hydrophilicity, functionality and biocompatibility [95]. Thi is because other important aspect regarding biocompatible materials is the bioactivity. A bioactive material is defined as a material that elicits a specific response at the interface of the material, which results on the formation of a bond between the tissue and that material [96]. For this purpose, surface modification to produce a porous structure may lead to increased bioactivity. Porous structures not only help to reduce the density of metallic implants and stiffness mismatches between implant and host tissue, but also has significant influence on bone cell adhesion.

Recently, some amorphous alloys have been stated as biocompatible as in the case of Zr-Nb-Cu-Pd-Al, Zr-Nb-Cu-Fe-Al [97], Ti-Zr-Pd-Cu-Sn [98, 99] or Zr-Cu-Fe-Al [100, 101] systems. Nevertheless, they contain a considerably large amount of Cu and this element has been detected as a toxic and may lead to harmful reactions inside human body. Some elements such as Ni or Be that are common in multicomponent metallic galsses make them not suitable in biocompatible applications.

On the other hand, some examples that show favorable biocompatibility are the Ti-Zr-Fe-Si and Ti-Zr-Fe-Si-Mo-Nb systems [102]. Additionally, porous structures with irregular nanometer circles like honeycomb are developed on their surface to improve their properties. Finally, other good example on the efforts of the scientific comunity dedicated

to the search of biocompatible metalli glasses is the system with general composition Mg-Zn-Ca [103]. This alloy shows not just good biocompatibility but it has been proposed that this material can biocorrode, and therefore would not be necessary to remove implanted pieces due to this property. However, the effects of the high Zn concentration near to human tissue have not been tested yet. Therefore, the need of new alloys with good biocompatibility, bioactivity and mechanical properties motivated this work.

One of the challenges for fabricating amorphous alloys is the need of high cooling rates to avoid crystallization. In several alloys with good glass forming ability (GFA) it has been observed that they own a composition at or near to deep eutectics. For binary alloys, the process to find these compositions is rather easy by using phase diagrams. However, as it has been pointed out in the previous sections, good glass formers are usually integrated by more than two elements. The process of finding new MGs with eutectic compositions in a multicomponent system become complex by the lack of thermodynamic information and to determine experimentally the optimal concentrations turns into a time consuming and not always successful process.

It has been observed that bulk metallic glasses (BMGs) with high GFA follow three empirical component rules [1]:

1. Multicomponent systems consisting of more than three elements.
2. Significant difference in atomic size above 12% among the main three constituent elements.
3. Large negative heats of mixing among the constituent elements.

On the other hand, a special $A-B$-type binary system has been observed for several alloys. The main properties of this systems are summarized as follows [104]:

1. Element A forms binary deep eutectics with each B-type element (B_1, B_2, B_3). Generally, heat of mixing of the atomic pairs of $A-B_1$, $A-B_2$, and $A-B_3$ is largely negative.

2. B-type elements tend to form either continuous solid solution with each other or have large solubility in one another at solid states. The tendency for forming atomic bonding between these B-type elements is relatively weak. Usually, the negative heat of mixing of the atomic pairs between them is much smaller than that of $A-B$ pairs.

By using these ideas, Lu *et.al.* [104] developed a basic physical concept of strong clusters of binary eutectics to locate good glass forming compositions in a fast way. This method is summarized in Figure 4.1 for a quaternary system, where A, B_1, B_2, and B_3, represent the elements in the special $A-B$-type system. The elements must satisfy preferably the following conditions: (a) The tendency for forming chemical clusters between $A-B_x$ is more preferred over $A-A$ or B_x-B_x. (b) The tendency for forming chemical clusters of B_x-B_y is similar to that of B_x-B_x.

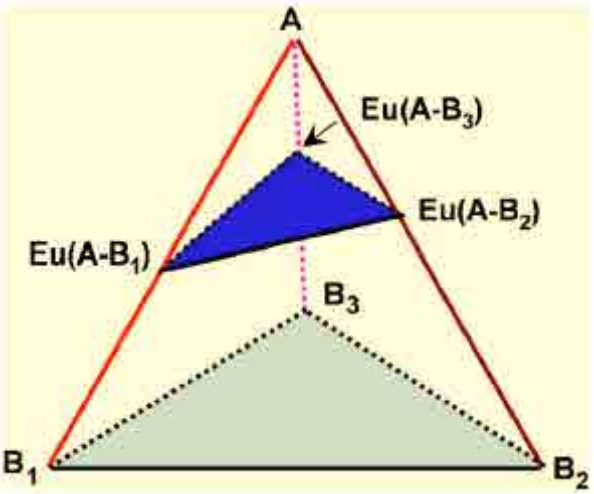

Figure 4.1: Composition diagram for a quaternary ideal glass-forming liquid A-(B_1,B_2,B_3) [104]. Good glass formers are likely within the composition range indicated by the blue triangle plane.

In order to avoid crystallization and to increase glass forming ability, all chemical clusters in the liquid should be as stable as possible. Clusters of the same element, *i.e.* near to one of the corners of the triangle, are usually highly unstable and tend to form crystalline phases. On the other hand, good glass forming liquids should contain mainly

the three types of stable binary $A - B_x$ clusters and the interaction between them must be minimal due to the small negative heat of mixing of B type elements.

Binary eutectics Eu($A - B_i$), with i=1,2,3, represent the chemical composition of the stable clusters of each A-B system. Therefore, to increase the GFA and the stability of the liquid phase, the composition range of the amorphous phase C_{am} may be obtained as follows:

$$C_{am} = \alpha[Eu(A - B_1) + \beta[Eu(A - B_2) + \gamma[Eu(A - B_3)], \tag{4.1}$$

where α, β and γ are constants and its sum is equal to the unity. The composition range obtained actually represents the blue triangle shown in Figure 4.1 bounded by the three deep binary eutectics and compositions with good glass forming ability will be located in this region.

Based on the previous ideas and on some of the criteria used to design multicomponent metallic glasses [100, 105] with the knowledge of phase diagrams, mixing enthalpies and individual properties of the elements involved, a new Zr-Ti-based amorphous alloy was prepared for biocompatibility purposes. Two of the metals introduced in small concentration proposed to increase GFA in "biocompatible"metallic glasses are Ti or Ag [106, 107]. Ca is added in this work to improve glass forming ability. It is expected that the incorporation of calcium as microalloying element will increase the GFA and the bioactivity of this new composition. Results show that the partially vitrified state of the base alloy (without calcium) becomes more stable using Ca as microalloying element. A set of samples with different Ca concentration has been prepared to evaluate the role of this element on the glass forming ability of this novel alloy.

4.2 Methodology

4.2.1 Materials

Amorphous alloys with a nominal composition of $[(Zr,Ti)_{69.5}(Al,Fe)_{30.5}]_{1-x}Ca_x$, with x=0, 1, 2, 3 and 4 (at.%) were prepared by the arc-melting and melt-spinning processes, as explained before, at the Universitat Politecnica de Catalunya (UPC-Campus Castelldefels) and the Universidad de Girona. The purity of the elements for the arc-melting process was in the range of 99.9% to 99.99%, and they were melted under a purified Ar atmosphere. Ribbons of 3 mm width and 30-50 μm thick, approximately, were obtained then by the melt-spinning method. The velocity of the copper wheel in this last process was set at 40 m/s.

4.2.2 X-ray diffraction (XRD)

The structural characterization was performed by X-ray diffraction (XRD) at beamline BM-16 at the European Synchrotron Facility (ESRF) [81]. The beamline uses a nominal energy of 12.6 keV in the Se K edge. The synchrotron X-ray beam was monochromatized at a wavelength of 0.7748 nm. The samples were positioned at ∼100 and ∼150 mm away from the detector. The measurements were performed in transmission mode. Lanthanum hexaboride is used for calibration and correction of detector distortions. As XRD data is obtained as a 2D image in the detector plate the *Fit-2D v12.081* program [43] is used to integrate the images.

4.3 Results

The selection of the two main elements, titanium and zirconium, was made based on the excellent properties that they have demonstrated in the field. Titanium is widely used in biomaterials since the 40's, and is now commercially available in pure and alloyed forms. In the alloyed form, different non-toxic elements are added to optimize its properties such as niobium, zirconium, tantalum, tin and molybdenum. In general, the elements that are avoided are nickel, chromium or cobalt. Additional heat treatments finally provide the alloy the desired properties. On the other hand, zirconium and more specifically Zr-based metallic glasses gained increased attention due to the combination of their high GFA with excellent mechanical properties such strength superior to 1.5 GPa, high elastic strain limit of around 2% and relatively low Young modulus between 50 to 100 GPa. Due to these properties, some amorphous systems of base of zirconium were proposed as biocompatible. However, most of these compositions include elements such as Ni or Cu. Finally, in order to improve the GFA in the prepared alloy in the present work, the addition of Ca is suggested to increase the GFA. This element is expected also to improve the biocompatible and bioactive properties of the final alloy.

Based on the concept of binary deep eutectics discussed in the first section of this Chapter, and the characteristics of the single elements used for the alloy preparation, the base elements chosen for the initial alloy are: Zr, Ti, Fe, Al and Ca. The atomic size and the crystalline structure presented by the individual elements are shown in Table 4.1, where differences in the atomic sizes and crystalline structures are evidenced.

Table 4.1: Some properties of the individual elements used to prepare the Zr-Ti-Fe-Al-Ca amorphous alloy.

Element	Atomic radius (Å)	Structure
Ti	1.47	hcp
Zr	1.60	hcp
Al	1.43	fcc
Fe	1.26	bcc
Ca	1.97	fcc

Large differences in the atomic structure as well as the introduction of different atomic sizes in the alloy are considered to enhance the GFA. However, the options to select the appropriate composition in a multicomponent system are considerably large. Therefore a detailed analysis of the phase diagrams is essential. Since the Zr-Ti system forms a solid solution with a heat of mixing considered as 0 kJ/mol [108] the elements of the alloy were grouped as (Zr,Ti) and (Fe,Al). In order to obtain a large GFA, the major types of binary clusters (A-B_i) in an ideal AB liquid should be as stable as possible. As it is well known, the most stable systems are located in the eutectic points. The composition of the proposed alloy is then located in a plane bounded by three binary eutectics: Zr-Fe, Zr-Al and Ti-Fe. All these three systems may form stable clusters with similar heat of mixing of -25, -44 and -17 kJ/mol [108] for the atomic pairs Zr-Fe, Zr-Al and Ti-Fe, respectively. By taking into consideration all previous data, the base composition was finaly defined as $(Zr,Ti)_{69.5}(Al,Fe)_{30.5}$.

Melt spun ribbons of the base alloy were prepared with a 40 m/s speed in the copper wheel. Figure 4.2 (up) shows the XRD pattern of the base alloy. As can be observed, signals of a crystalline phase appear as sharp peaks of high intensity, suggesting that is not possible to prepare the fully crystalline alloy under this conditions. Nevertheless, the weak signals of the crystalline phase imply that the amorphous state is predominant in the alloy and might be possible to obtain a fully amorphous sample by tuning this initial composition.

Calcium was then selected as microalloying element due to its atomic size compared with the other elements in the composition. Ca/Zr ratio is as large of 1.2, and the crystalline structures of these two elements correspond to *hcp* and fcc respectively. Other substantial reason to select calcium for this composition is that as an important element in bone formation, it would be expected that the presence of Ca in the alloy, favors the interaction alloy-tissue in biomedical applications. Calcium was then added as a percentage to the base alloy in the following ratio: $[(Zr,Ti)_{69.5}(Al,Fe)_{30.5}]_{1-x}Ca_x$. Melt spun ribbons of four alloys with different calcium concentration from 1 to 4 at.% were prepared under the same conditions than the base alloy. XRD patterns of these alloys are shown in Figure 4.2.

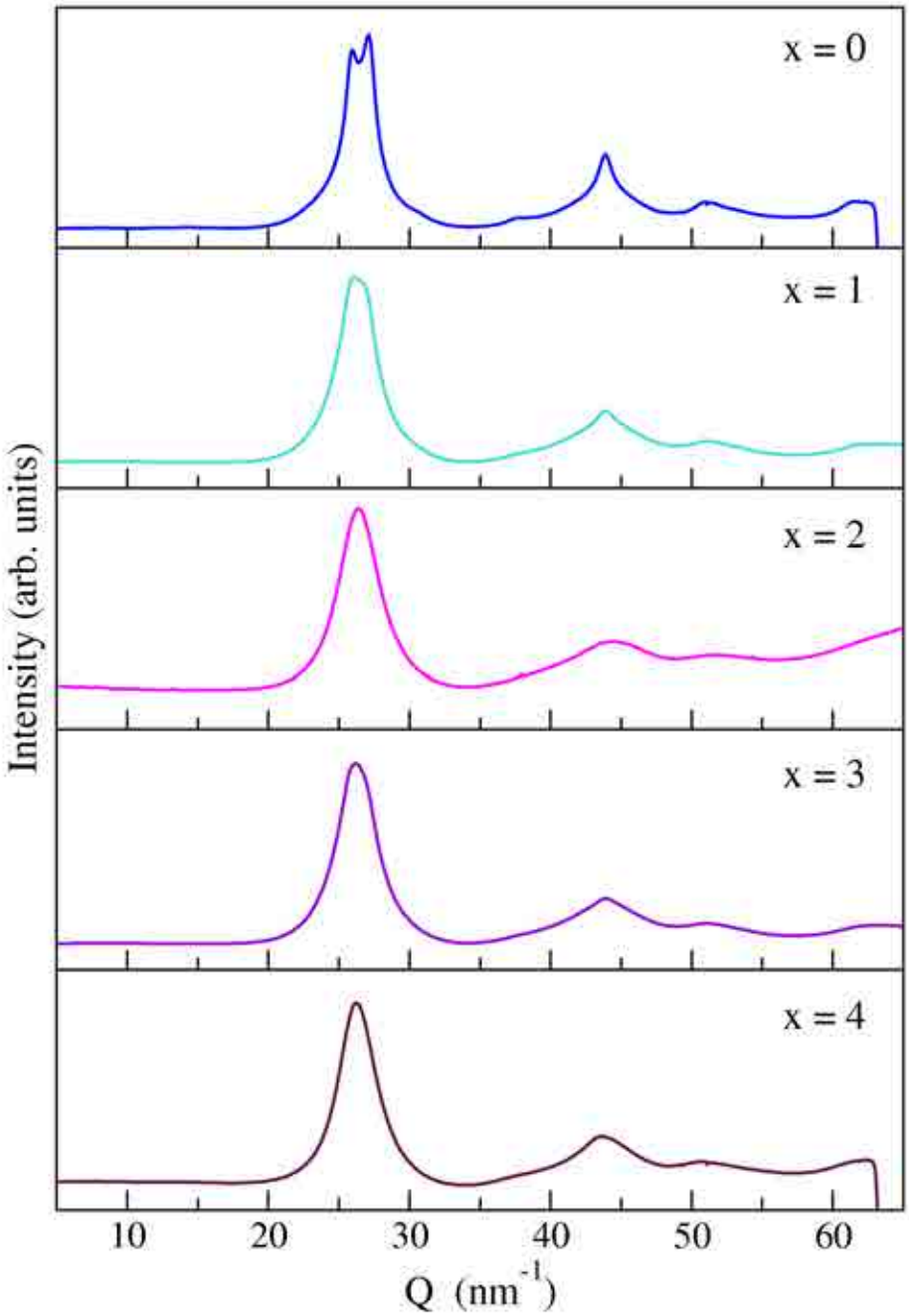

Figure 4.2: XRD patterns of the $[(Zr,Ti)_{69.5}(Al,Fe)_{30.5}]_{1-x}Ca_x$ alloys with x = 0, 1, 2, 3, and 4 at. % of Ca.

As proposed, glass forming ability was improved and no clear signals of Bragg peaks are detected in these new compositions. However, a wide peak at the most intense signal at around 28 nm^{-1} and the sharp peak at 44 nm^{-1} may indicate the presence of nanocrystals for the alloy with 1 at. % Ca. The alloys with 2 at. % Ca or more, show diffuse peaks and no signals of crystallization.

With the previous results it is possible to confirm the formation of an amorphous phase with the proposed composition. However more studies to determine the properties and possible applicability of the defined compositions are needed. For instance, in order to determine the critical diameter attainable in this system, casting test at different diameters would be required. Additional tests to evaluate the specific properties of this new composition after tunning in order to propose the final application are also envisaged. Nevertheless, a good response of combined mechanical and biocompatible properties are expected.

4.4 Conclusions and perspectives

In this section of the project, a completely new composition of metallic glasses for the multicomponent system $[(Zr,Ti)_{69.5}(Al,Fe)_{30.5}]_{1-x}Ca_x$ was prepared. This alloy does not contain toxic elements which make it suitable for further studies to evaluate its properties and possible applicability. Ca microalloying have demonstrated to improve glass forming ability by favoring glassy state stabilization.

Althought in this work is demostrated the possibility to produce an amorphous alloy with the desired elements, more studies to evaluate the properties of the prepared alloy and to tune its composition to stabilize the amorphous phase are needed. Changes in composition are followed by cahnges in the thermodynamics of the alloy and consequently the glass forming ability. The glass forming ability of the starting composition can be tunned by following different processes. By tunning the properties of the base alloy before adding the microalloying element would lead to a more stable amorphous phase. In some cases, the deepest eutectic is replaced by other eutectics in the same system. For the present work, compositions near to the deepest eutectics were selected. However, it is suggested that binary eutectics consisting of line compounds with strict stoichiometry stabilize larger clusters and glass formation is favored [104].

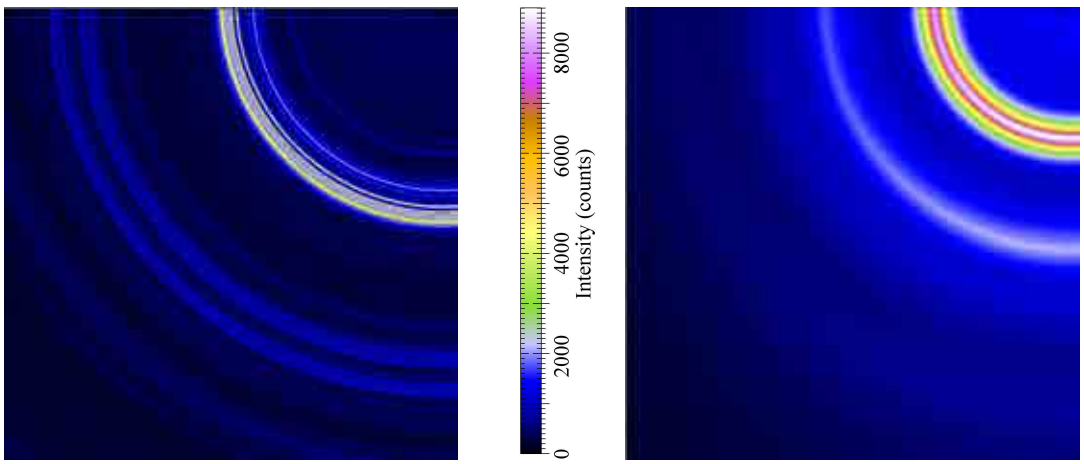

Figure 4.3: Example of the 2D patterns of the $[(Zr,Ti)_{69.5}(Al,Fe)_{30.5}]_{98}Ca_2$ ribbons: (*left*) prepared with oxidized Ca, (*right*) prepared with oxigen free Ca.

Optimization of the base alloy by following this process may lead to formation of a more stable amorphous phase, and consequently, the possibility of fabrication of larger samples could be expected. Therefore, further analysis are needed in order to determine the alloy with the suited characteristics.

On the other hand, oxygen reactivity with some elements present in the alloy, such as Ca or Ti, is an important issue to take into account during the fabrication of this alloy. Oxygen may destabilize the amorphous phase and favor intermetallic phases formation. One example of this are the selected 2D plots obtained at beamline BM-16 at the European Synchrotron Facility in Figure 4.3. In the left pannel, a not well controlled atmosphere during the sample preparation lead the formation of a fully crystalline structure for the $[(Zr,Ti)_{69.5}(Al,Fe)_{30.5}]_{1-x}Ca_x$ alloy with 2 at. % Ca. In the right pannel, an oxygen-free atmosphere during the sample preparation promotes the formation of the amorphous phase. Therefore, for the defined composition in this work, a well controlled atmosphere during sample preparation is also essential for the success in the amorphous phase stabilization.

Chapter 5

General conclusions

Through this manuscript was presented the behaviour of different compositions of metallic glasses as a response to an additional variable, namely pressure for the analysis of polyamorphic transitions in Ce-based alloys; composition and temperature for the analysis of glass forming ability, crystallization and corrosion behaviour in Fe-based metallic glasses; and microalloying in the preparation of new amorphous systems. As proposed at the beginning of this manuscript, the three different projects were separated in Chapters 2, 3 and 4. In the text of these chapters, the state of the art, results and their analysis in extent and the final discussion and conclusions are presented. In the present Chapter, only the conclusions of all the previous chapters are sumarized.

Structural and high frequency mechanical response upon application of pressure on a Ce-based metallic glass.

- A thorough investigation of the behavior of structural and mechanical properties of $Ce_{70}Al_{10}Ni_{10}Cu_{10}$ metallic glass by X-ray diffraction and inelastic X-ray scattering upon application of pressure up to 25 GPa was reported.
- A low and a high density amorphous phase were found at different pressure ranges, with an intermediate density region which could be a mixture of both phases between 2 and 10 GPa.
- Decompression from the high density phase results into a reversible change to the ambient pressure phase, though hysteresis is observed in the static structure factor for the intermediate density region.
- The XRD results correlate well with changes with pressure in the longitudinal acoustic sound speed and the associated elastic constant as revealed by IXS experiments.
- The hysteresis in structural changes affects the acoustic sound speed and becomes more apparent in the comparison of acoustic mode energies at high momentum transfers.
- Both structural and dynamical hysteresis effects seem to cancel each other in the estimate of the longitudinal elastic constant.
- The observed polyamorphic transition in $Ce_{70}Al_{10}Ni_{10}Cu_{10}$ upon application of pressure is attributed to a change in Ce $4f$ electrons from a localized electronic structure to an itinerant one, similarly to the results reported for other Ce-based MGs and for crystalline Ce.
- The analysis of reported data on similar polyamorphic transitions for other Ce-based amorphous alloys reveals a broadening of the intermediate density region with increasing atomic alloying and reducing Ce content related to higher diversity of local environments in the more complex Ce-based metallic glasses. This broadening seems to saturate upon decrease of Ce concentrations below 55 %.

- The lower limit for the polyamorphic transformation remains nearly unchanged, at 2 GPa, i.e. double the $\gamma - \alpha$ transition in crystalline Cerium, up to a concentration of 55 % atomic Cerium.

- Further IXS experiments on intermediate Ce-content amorphous alloys are required to fully uncouple the role of $4f$ Ce electrons from lattice degrees of freedom and achieve a better comprehension of polyamorphic transformations in these alloys.

Microalloying effects of Yttrium in a Fe-based metallic glass and the effect of heat treatments on structural properties and corrosion behavior.

Yttrium concentration dependence on modification of local order and glass forming ability in $Fe_{50-x}C_{15}Mo_{14}Cr_{15}B_6Y_x$ *metallic glasses, with x=0,1,2,3 at.%.*

- The positive effect of Yttrium on the glass forming ability was corroborated. The addition of 2 at.% yttrium in the $Fe_{50-x}Cr_{15}Mo_{14}C_{15}B_6Y_x$ system stabilizes the glassy state presenting the largest supercooled liquid region of the studied compositions.

- The high glass forming ability of the system allows the fabrication of bars of 3 mm diameter for the 0 at.% yttrium while at least 5 mm diameter rods are obtained when more than 1 at.% yttrium is added to the composition.

- The improvement of the glass forming ability, as well as the increase on hardness above 4 %, are attributed to the large size of yttrium atoms that contributes to strengthening the lattice and its superior bulk modulus that provides a higher hardness to the base alloy. as observed for similar alloys by other authors.

- Nanoindentation and tension tests would be advised to further understanding of the role of yttrium in the mechanical properties of amorphous steels and the formation of shear bands.

- High corrosion resistance for all the studied compositions of the system is also corroborated as they passivate spontaneously in HCl 0.1 M.

- It is suggested that the large amount of passivating elements together with the uniformity of the amorphous phase provide the alloy with an excellent corrosion resistance.

- The final breakdown potential is similar for all the compositions, indicating that there is not a remarked influence on the corrosion behavior by addition of small amounts of yttrium; however, small changes in the general behavior can be pointed out.

- The anodic current density in the active region slightly increases when yttrium is added to the alloy. The small increase of the passive current density indicates the formation of a slightly lower protective quality of the passive film. Nevertheless, these small differences do not compromise the general stability of the alloy.

- The surface preparation of the samples prior to the measurements proved to be a key aspect to ensure reproducibility of the data. Surface impurities and protective oxides formed during the melt spinning process provide an additional passive state, however, as these films are not homogeneous, a prior preparation by ion-milling, for example, to remove these impurities is advised.

Phase segregation and crystallization in a $Fe_{50}Cr_{15}Mo_{14}C_{15}B_6$ metallic glass.

- The amorphous nature of the as produced $Fe_{50}Cr_{15}Mo_{14}C_{15}B_6$ alloy is confirmed by XRD, SEM, APT.

- No signs of chemical heterogeneity in the fully amorphous state were neither detected.

- Deviation of the observed distribution with respect to the binomial distribution in atom probe results indicates heterogeneity in the composition of the, still amorphous, alloy treated near to the glass transition temperature at 550° C.

- Crystallization is carried on by nucleation and growth of a primary phase under non-equilibrium conditions from the undercooled liquid state, as in several other metallic glasses.

- Near the onset of the first crystallization temperature at 610° C partial devitrification of the $Fe_{50}Cr_{15}Mo_{14}C_{15}B_6$ alloy causes formation of nanocrystalline carbide phases dispersed in a matrix of the remaining amorphous phase.

- The combination of AES and APT can link surface properties with detail in morphology and composition. In agreement with the AES result, APT data obtained from a fully-crystallized sample shows Mo-rich and Fe-Cr-rich areas clearly visible. Boron and Carbon segregate to FeCr / Mo interfaces.

- Devitrification process in this case may be then described in a two stage crystallization process where the first phase heterogeneously nucleates in a primary crystallization reaction to form $M_{23}(C,B)_6$.

- The final microstructure is composed of M_6C carbides embedded in a $M_{23}(C,B)_6$ phase.

- The effects of the microstructure in corrosion behavior were discussed in terms of the chemistry and microstructure of the alloy.

- The homogeneity in chemistry and structure of the amorphous material provide the alloy with a high corrosion resistance.

- Heat treatments intended to crystallize the alloy at different stages show a detrimental effect on the corrosion properties. Heterogeneity in composition and formation of Cr-depleted zones lead to dissolution of Mo-rich phases and reduction of the corrosion resistance of the passive film.

- The general resistance of the alloy is not compromised for low annealing temperatures, or crystallization fraction below 50 %. After this threshold value, a severe detriment on the corrosion breakdown due to dissolution of Mo-rich phases, clearly depleted in chromium is promoted.

Development of Zr-Ti based alloys for biocompatible applications.

- A new system with composition $[(Zr,Ti)_{69.5}(Al,Fe)_{30.5}]_{1-x}Ca_x$, without toxic elements, was obtained in the fully amorphous state.
- The base composition, *i.e.* without calcium, shows weak signals of a crystalline structure within the amorphous background. A fine tuning of the composition of the base alloy is therefore necessary for further studies.
- Calcium element, added in small concentration, improves the glass forming ability of the system $[(Zr,Ti)_{69.5}(Al,Fe)_{30.5}]_{1-x}Ca_x$, with a Ca concentration superior to 1 at. %.

Chapter 6

Appendix A

All IXS spectra of the $Ce_{70}Al_{10}Ni_{10}Cu_{10}$ metallic glass for P between 0 and 22.5 GPa and Q between 2 and 12 nm^{-1} under compression and decompression are presented in the next pages. Open circles correspond to experimental data and solid lines to the best fit obtained using Eq.2.15. The individual components of the excitation and elastic line are displayed with dashed lines. Note that the quality fitting is diminished for $q = 3.2nm^{-1}$ and $q = 10.3nm^{-1}$. At these momentum transfers, the resolution functions are not able to describe properly the tails of the elastic peak. Due to this fact, these momentum transfers are not further considered in the analysis. Additionally, you may notice that the spectra correspond to momentum transfers spaced by 1.2 nm^{-1}, with the exception of the gap between 8 and 10.3 nm^{-1}. This gap results from the ill-functioning of the analyzer number 4 set at $q = 9.2nm^{-1}$, as mentioned in the Methodology section.

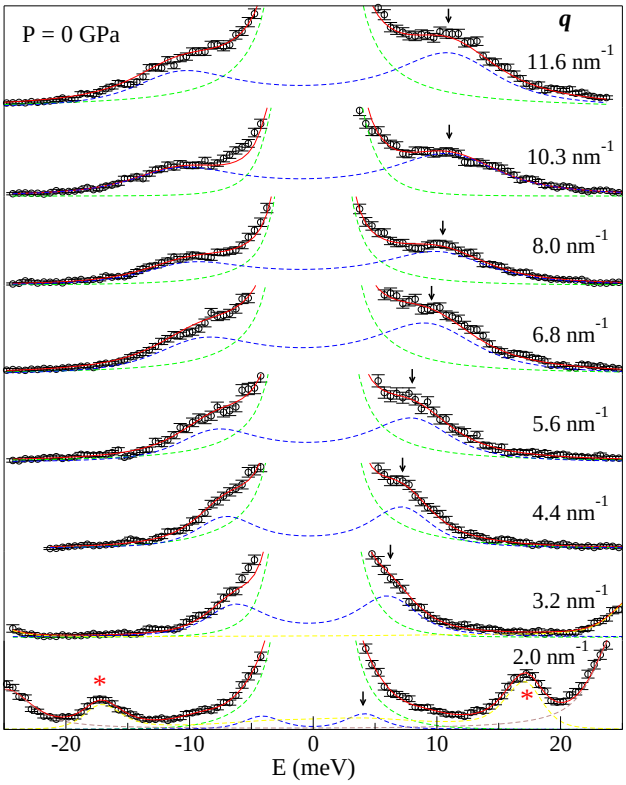

Figure 6.1: IXS spectra of the $Ce_{70}Al_{10}Ni_{10}Cu_{10}$ metallic glass for $P = \mathbf{0\ GPa}$ and Q between 2 and 12 nm^{-1}.

Table 6.1: Data obtained from the IXS spectra at 0 GPa. The error bars are given in parentheses.

Detector #	θ (deg)	Q (nm^{-1})	E (meV)	Γ (meV)	A_{In}	A_{Ph}
1	1.27	2	4.05(11)	1.5(2)	10017.9	2427.2
6	2.01	3.2				
2	2.79	4.4	7.52(13)	2.9(4)	11366.2	1930.1
7	3.54	5.6	8.89(16)	5.5(7)	7129.5	1802.2
3	4.32	6.8	10.56(12)	7.8(4)	12045.1	3747.1
8	5.06	8	11.47(16)	8.1(6)	8106.9	2542.8
9	6.57	10.3	11.84(16)	6.6(5)	8484.7	3231.8
5	7.36	11.6	12.44(13)	9.9(5)	15905.3	6230.5

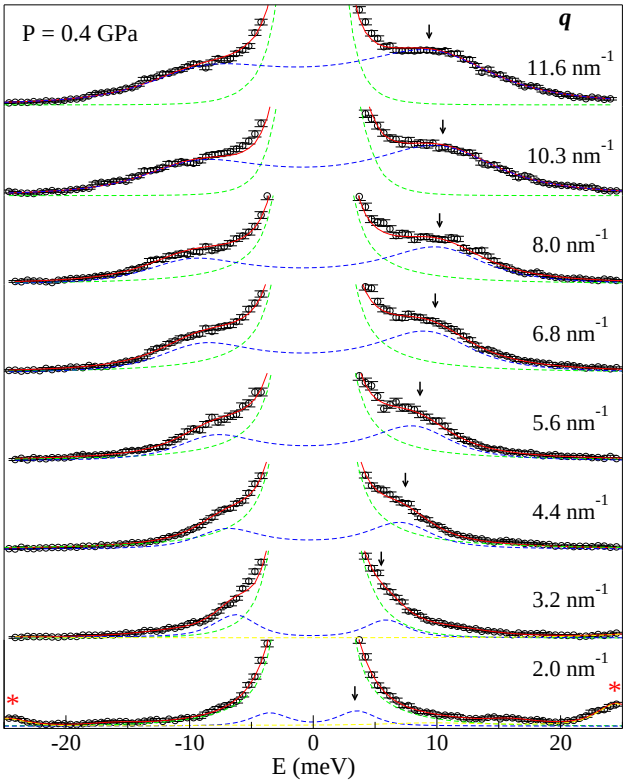

Figure 6.2: IXS spectra of the $Ce_{70}Al_{10}Ni_{10}Cu_{10}$ metallic glass for $P = \mathbf{0.39\ GPa}$ and Q between 2 and 12 nm^{-1} under compression.

Table 6.2: Data obtained from the IXS spectra at 0.39 GPa under compression. The error bars are given in parentheses.

Detector #	θ (deg)	Q (nm^{-1})	E (meV)	Γ (meV)	A_{In}	A_{Ph}
1	1.27	2	3.27(22)	0.9(1)	21049.7	1408.5
6	2.01	3.2	5.50(2)	1.6(9)	32910.1	1880.3
2	2.79	4.4	7.50(10)	3.2(3)	27453.6	4352.0
7	3.54	5.6	8.89(11)	5.3(3)	11840.1	2826.3
3	4.32	6.8	10.30(8)	7.0(2)	21787.1	7114.5
8	5.06	8	11.21(9)	7.5(3)	15112.0	4763.8
9	6.57	10.3	11.32(9)	8.2(3)		
5	7.36	11.6	11.63(7)	11.0(3)	25546.1	14774.4

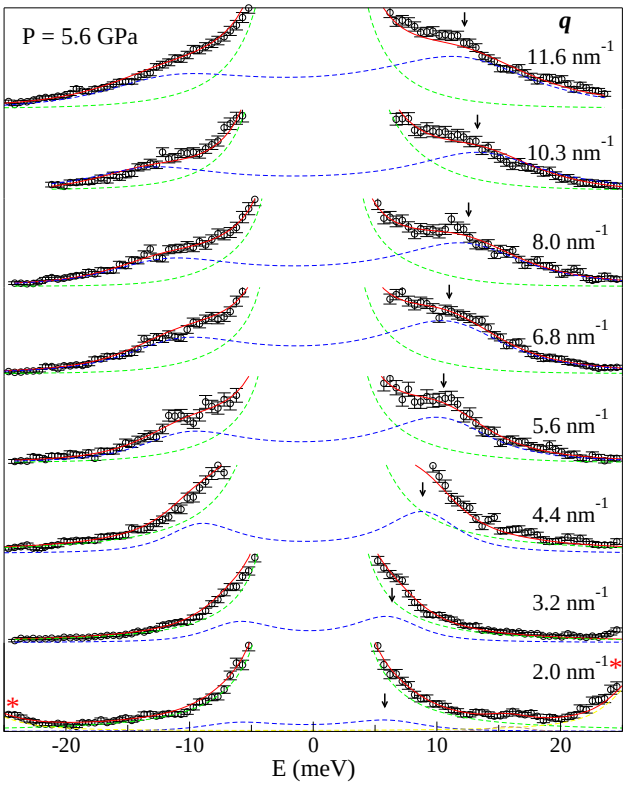

Figure 6.3: IXS spectra of the $Ce_{70}Al_{10}Ni_{10}Cu_{10}$ metallic glass for $P = \mathbf{5.60\ GPa}$ and Q between 2 and 12 nm^{-1} under compression.

Table 6.3: Data obtained from the IXS spectra at 5.60 GPa under compression. The error bars are given in parentheses.

Detector #	θ (deg)	Q (nm^{-1})	E (meV)	Γ (meV)	A_{In}	A_{Ph}
1	1.27	2	5.31(34)	1.50(-)		
6	2.01	3.2	7.04(2)	2.50(02)	17411.8	1727.1
2	2.79	4.4	9.56(17)	4.42(51)	18312.4	1709.0
7	3.54	5.6	11.28(18)	6.19(54)	7943.2	1294.1
3	4.32	6.8	12.70(14)	10.72(46)	13026.5	4037.3
8	5.06	8	13.78(18)	9.12(50)	10745.7	2065.1
9	6.57	10.3	14.73(47)	14.49(98)		
5	7.36	11.6	13.73(18)	10.45(51)	24705.0	4585.4

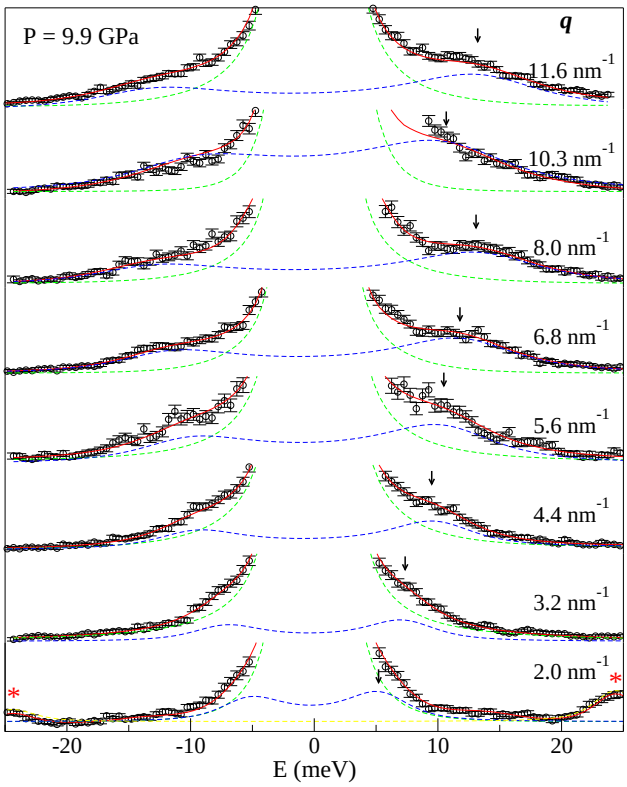

Figure 6.4: IXS spectra of the $Ce_{70}Al_{10}Ni_{10}Cu_{10}$ metallic glass for $P = \mathbf{9.92\ GPa}$ and Q between 2 and 12 nm^{-1} under compression.

Table 6.4: Data obtained from the IXS spectra at 9.92 GPa under compression. The error bars are given in parentheses.

Detector #	θ (deg)	Q (nm^{-1})	E (meV)	Γ (meV)	A_{In}	A_{Ph}
1	1.27	2	5.77(19)	3.33(62)	14541.1	2022.2
6	2.01	3.2	7.60(2)	3.42(3)	14978.3	1282.1
2	2.79	4.4	10.53(23)	3.82(69)	21658.7	1664.7
7	3.54	5.6	11.56(35)	7.08(98)	8611.7	1100.8
3	4.32	6.8	13.27(22)	8.28(71)	13453.7	2323.6
8	5.06	8	14.82(25)	11.81(88)	11396.3	1737.2
9	6.57	10.3				
5	7.36	11.6	14.86(19)	9.28(52)	27003.7	3328.9

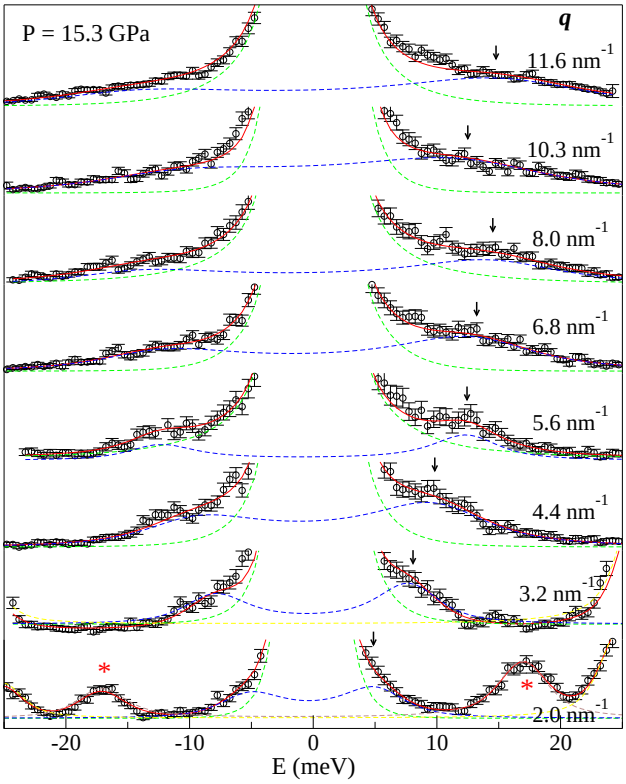

Figure 6.5: IXS spectra of the $Ce_{70}Al_{10}Ni_{10}Cu_{10}$ metallic glass for $P = \mathbf{15.31\ GPa}$ and Q between 2 and 12 nm^{-1} under compression.

Table 6.5: Data obtained from the IXS spectra at 15.31 GPa under compression. The error bars are given in parentheses.

Detector #	θ (deg)	Q (nm^{-1})	E (meV)	Γ (meV)	A_{In}	A_{Ph}
1	1.27	2	5.65(21)	3.29(62)	6854.5	1578.9
6	2.01	3.2	8.13(19)	2.56(49)	8048.2	1322.5
2	2.79	4.4	11.37(21)	4.88(64)	8606.2	797.7
7	3.54	5.6	12.71(34)	5.61(98)	4709.4	468.7
3	4.32	6.8	14.51(44)	11.59(13)	8767.8	1758.6
8	5.06	8	16.26(52)	12.89(98)	8222.6	934.1
9	6.57	10.3	156.00(46)	14.83(86)		
5	7.36	11.6	17.84(37)	16.41(98)	16284.3	2655.1

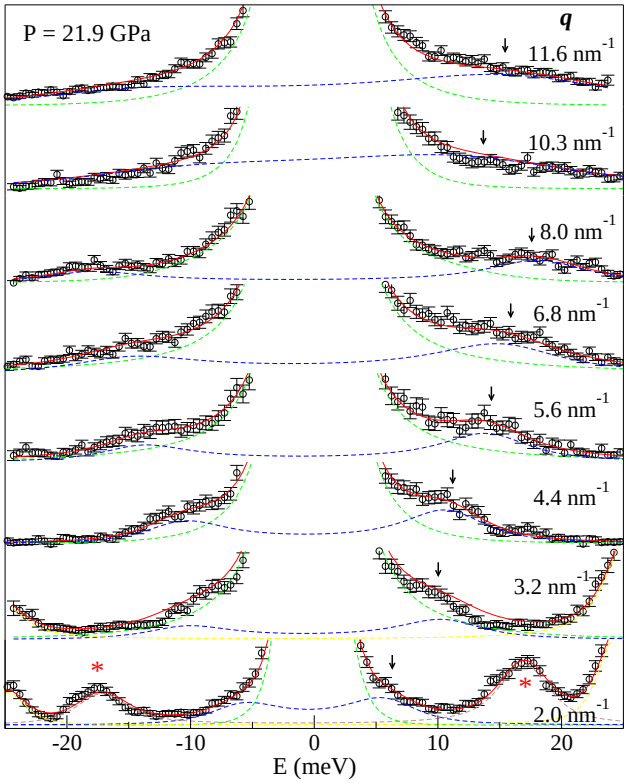

Figure 6.6: IXS spectra of the $Ce_{70}Al_{10}Ni_{10}Cu_{10}$ metallic glass for $P = \mathbf{21.9\ GPa}$ and Q between 2 and 12 nm^{-1} under compression.

Table 6.6: Data obtained from the IXS spectra at 21.9 GPa under compression. The error bars are given in parentheses.

Detector #	θ (deg)	Q (nm^{-1})	E (meV)	Γ (meV)	A_{In}	A_{Ph}
1	1.27	2	6.40(27)	4.13(82)	6262.6	957.4
6	2.01	3.2	10.51(3)			
2	2.79	4.4	11.21(25)	5.15(111)	10397.2	1375.3
7	3.54	5.6	14.32(33)	5.13(126)	5930.8	474.1
3	4.32	6.8	15.64(45)	12.62(114)	10491.0	1497.0
8	5.06	8	18.76(41)	7.28(124)	9580.6	592.5
9	6.57	10.3	19.57(57)	11.16(–)		
5	7.36	11.6	19.91(68)	20.86(231)	18243.1	2675.5

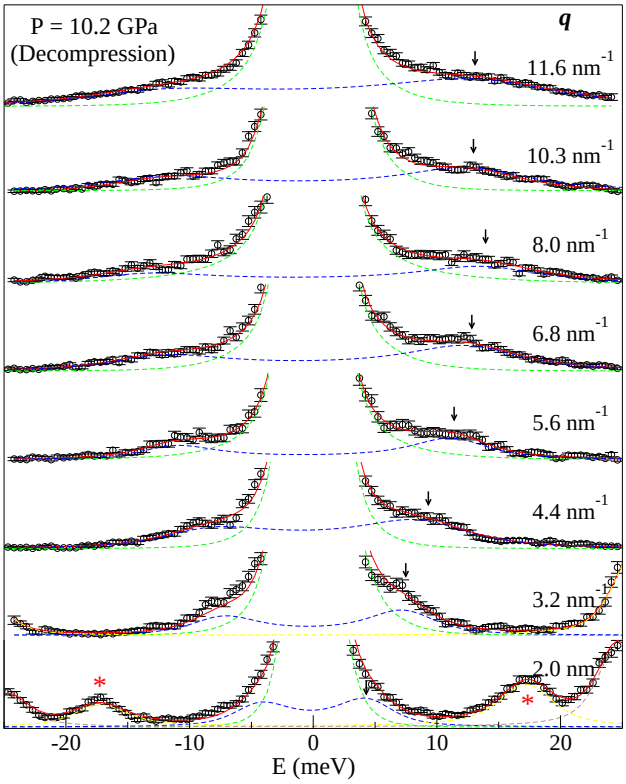

Figure 6.7: IXS spectra of the $Ce_{70}Al_{10}Ni_{10}Cu_{10}$ metallic glass for $P = \mathbf{10.24\ GPa}$ and Q between 2 and 12 nm^{-1} under **decompression**.

Table 6.7: Data obtained from the IXS spectra at 10.2 GPa under decompression. The error bars are given in parentheses.

Detector #	θ (deg)	Q (nm^{-1})	E (meV)	Γ (meV)	A_{In}	A_{Ph}
1	1.27	2				
6	2.01	3.2	7.89(2)		8404.8	602.6
2	2.79	4.4	10.04(25)	8.45(138)	8849.1	1826.2
7	3.54	5.6	11.69(26)	4.99(94)	5366.5	628.4
3	4.32	6.8	13.71(31)	9.19(111)	9620.2	1719.0
8	5.06	8	15.01(46)	9.81(133)	9169.7	1043.4
9	6.57	10.3	13.60(33)	8.41(99)	10112.7	1981.9
5	7.36	11.6	16.03(36)	15.46(111)	17287.9	3751.5

Bibliography

[1] Inoue, A., Acta Materialia **48** (2000) 279.

[2] Klement, W., Willens, R., and Duwez, P., Nature **187** (1960) 869.

[3] Ashby, M. and Greer, A., Scripta Materialia **54** (2006) 321.

[4] Johnson, W. and Samwer, K., Physical Review Letters **95** (2005) 195501.

[5] Inoue, A., Shen, B., Koshiba, H., Kato, H., and Yavari, A., Nature materials **2** (2003) 661.

[6] Shen, B. and Inoue, A., Journal of Physics: Condensed Matter **17** (2005) 5647.

[7] Inoue, A. and Nishiyama, N., MRS bulletin **32** (2007) 651.

[8] Yavari, A., Lewandowski, J., and Eckert, J., MRS Bulletin **32** (2007) 635.

[9] Sheng, H. et al., Nature Materials **6** (2007) 192.

[10] Li, Y. et al., MRS bulletin **32** (2007) 624.

[11] Wang, D. et al., Applied Physics Letters **84** (2004) 4029.

[12] Wang, D., Tan, H., and Li, Y., Acta Materialia **53** (2005) 2969.

[13] Löffler, J. and Johnson, W., Intermetallics **10** (2002) 1167.

[14] Greer, A., Science **267** (1995) 1947.

[15] Marin, P. and Hernando, A., Journal of Magnetism and Magnetic Materials **30** (2000) 80.

[16] Busch, R. et al., Materials Research Society Symposium Proceedings **806** (2004) 387.

[17] Yoshida, S., Mizushima, T., Hatanai, T., and Inoue, A., IEEE Transactions on Magnetics **36** (2000) 3424.

[18] Katayama, Y. et al., Nature **403** (2000) 170.

[19] Winter, R. et al., Journal of Physics: Condensed Matter **2** (1990) 8427.

[20] McMillan, P., Journal of Materials Chemistry **14** (2004) 1506.

[21] Mishima, O., Calvert, L., and Whalley, E., Nature **314** (1985) 76.

[22] Morishita, T., Physical Review Letters **93** (2004) 055503.

[23] Deb, S., Wilding, M., Somayazulu, M., and Mcmillan, P., Nature **414** (2001) 528.

[24] Sastry, S. and Angell, C., Nature materials **2** (2003) 739.

[25] Wilding, M. and McMillan, P., Journal of Non-Crystalline Solids **293-295** (2001) 357.

[26] McMillan, P. and Wilding, M., Journal of Non-Crystalline Solids **354** (2008) 1015.

[27] Meade, C., Hemley, R., and Mao, H., Physical Review Letters **69** (1992) 1387.

[28] Huang, L., Duffrene, L., and Kieffer, J., Journal of Non-Crystalline Solids **349** (2004) 1.

[29] Sen, S., Gaudio, S., Aitken, B., and Lesher, C., Physical Review Letters **97** (2006) 025504.

[30] Soderlind, P., Advances in Physics **47** (1998) 959.

[31] Shick, A., Pickett, W., and Liechtenstein, A., Journal of Electron Spectroscopy and Related Phenomena **114** (2001) 753.

[32] Zeng, Q. et al., Physical Review Letters **104** (2010) 105702.

[33] Zeng, Q. et al., Physical Review B **82** (2010) 054111.

[34] Dorner, B. and Peisl, J., Nuclear Instruments and Methods in Physics **208** (1983) 587.

[35] Burkel, E., Peisl, J., and Dorner, B., Europhysics Letters **3** (1987) 957.

[36] http://www.esrf.eu/.

[37] http://www.aps.anl.gov/.

[38] http://www.spring8.or.jp/.

[39] Monaco, G., Comptes Rendus Physique **9** (2008) 608.

[40] Rueff, J.-P., Reviews of Modern Physics **82** (2010) 847.

[41] Mao, H. and Bell, P., Science **191** (1976) 851.

[42] Liu, Z., Cui, Q., and Zou, G., Physics Letters A **143** (1990) 79.

[43] http://www.esrf.eu/computing/scientific/FIT2D/.

[44] Zhang, B., Wang, R., and Wang, W., Physical Review B **72** (2005) 104205.

[45] Murnaghan, F., Proceedings of the National Academy of Sciences of the United States of America **30** (1944) 244.

[46] Svane, A., Temmerman, W., Szotek, Z., Legsgaard, J., and Winter, H., International Journal of Quantum Chemistry **77** (2000) 799.

[47] Pickett, W., Physica 111B **81** (1981) 1.

[48] Rout, G., Ojha, M., and Behera, S., Physica B: Condensed Matter **367** (2005) 101.

[49] Scopigno, T., Suck, J.-B., Angelini, R., Albergamo, F., and Ruocco, G., Physical Review Letters **96** (2006) 135501.

[50] Rufflé, B., Guimbretière, G., Courtens, E., Vacher, R., and Monaco, G., Physical Review Letters **96** (2006) 045502.

[51] Krisch, M. et al., Proceedings of the National Academy of Sciences of the United States of America **108** (2011) 9342.

[52] Zeng, Q. et al., Journal of Physics: Condensed Matter **22** (2010) 375404.

[53] Zeng, Q. et al., Proceedings of the National Academy of Sciences of the United States of America **104** (2007) 13565.

[54] Inoue, A., Shen, B., and Chang, C., Acta Materialia **52** (2004) 4093.

[55] Gu, X., Poon, S. J., Shiflet, G., and Widom, M., Applied Physics Letters **92** (2008) 161910.

[56] Ponnambalam, V. et al., Applied Physics Letters **83** (2003) 1131.

[57] Wang, H., Shiflet, G., Poon, S., Matsuda, K., and Ikeno, S., Applied Physics Letters **91** (2007) 141910.

[58] Lu, Z., Liu, C., Thompson, J., and Porter, W., Physical Review Letters **92** (2004) 245503.

[59] Ponnambalam, V., Poon, S., and Shiflet, G., Journal of Materials Research **19** (2004) 1320.

[60] Ha, H., Miller, J., and Payer, J., Journal of The Electrochemical Society **156** (2009) C246.

[61] Hashimoto, K., Applied Surface Science **257** (2011) 8141.

[62] Punckt, C., Science **305** (2004) 1133.

[63] Ryan, M., Nature **415** (2002) 770.

[64] Ha, H. and Payer, J., Metallurgical and Materials Transactions A **40** (2009) 2519.

[65] Lu, Z. and Liu, C., Bulk amorphous steels based on Fe alloys. Patent number: 7052561, 2006.

[66] Zhang, Y., Applied Physics Letters **89** (2006) 131904.

[67] Chen, J., Scripta Materialia **54** (2006) 1351.

[68] Pardo, A., Merino, M., Otero, E., Lopez, M., and M hich, A., Journal of Non-Crystalline Solids **352** (2006) 3179.

[69] Szewieczek, D. and Paszenda, Z., Journal of Materials Processing Technology **78** (1998) 171.

[70] Pawlik, P. and Davies, H., Scripta Materialia **49** (2003) 755.

[71] Hono, K. and Ping, D., Materials Characterization **44** (2000) 203.

[72] Koster, U., Meinhardt, J., Roos, S., and Busch, R., Materials Science and Engineering A **226-228** (1997) 995.

[73] Naka, M., Hashimoto, K., and Masumoto, T., Journal of the Japan Institute of Metals **38** (1974) 835.

[74] Archer, M., Corke, C., and Harji, B., **32** (1987) 13.

[75] Scully, J., Gebert, A., and Payer, J., Journal of Materials Research **22** (2007) 302.

[76] Hashimoto, K., Corrosion **58** (2002) 715.

[77] Pang, S., Zhang, T., Asami, K., and Inoue, A., Acta Materialia **50** (2002) 489.

[78] Kelly, T. and Miller, M., Review of Scientific Instruments **78** (2007) 031101.

[79] Wild, R., Vacuum **31** (1980) 183.

[80] Tilinin, I., Jablonski, A., and Werner, W., Progress in Surface Science **52** (1996) 193.

[81] http://www.esrf.eu/UsersAndScience/Experiments/CRG/BM16/.

[82] http://www.cameca.com.

[83] Miller, M., Russell, K., and Thompson, G., Ultramicroscopy **102** (2005) 287.

[84] Thompson, G. et al., Ultramicroscopy **107** (2007) 131.

[85] Hellman, O., Vandenbroucke, J., Rusing, J., Isheim, D., and Seidman, D., Microscopy and Microanalysis **6** (2000) 437.

[86] http://www.thermocalc.com/.

[87] Klemm, S., Schauer, J., Schuhmacher, B., and Hassel, A., Electrochimica Acta **56** (2011) 4315.

[88] Lu, Z., Liu, C., and Porter, W., Applied Physics Letters **83** (2003) 2581.

[89] Asami, K., Naka, M., Hashimoto, K., and Masumoto, T., Journal of The Electrochemical Society **127** (1980) 2130.

[90] Moffat, T. and Latanision, R., Journal of The Electrochemical Society **139** (1992) 1869.

[91] http://www.lasurface.com/.

[92] Nouri, A., Liu, D., and Lewandowski, J., Metallurgical and Materials Transactions A **40A** (2009) 1314.

[93] Pang, S., Zhang, T., Asami, K., and Inoue, A., Corrosion Science **44** (2002) 1847.

[94] Klose, J. et al., Materialwissenschaft und Werkstofftechnik **39** (2008) 304.

[95] Quin, F., Wang, X., and Inoue, A., Intermetallics **16** (2008) 917.

[96] Gupta, R. and Kumar, A., Biomedical materials **3** (2008) 034005.

[97] Liu, L., Qiu, C., Chen, Q., Chan, K., and Zhang, S., Journal of biomedical materials research. Part A **86** (2008) 160.

[98] Oak, J.-J., Louzguine-Luzgin, D., and Inoue, A., Journal of Materials Research **22** (2007) 1346.

[99] Oak, J., Louzguine-Luzgin, D., and Inoue, A., Materials Science and Engineering: C **29** (2009) 322.

[100] Jin, K. and Loffler, J., Applied Physics Letters **86** (2005) 241909.

[101] Buzzi, S. et al., Intermetallics **14** (2006) 729.

[102] Bai, L., Cui, C., Wang, Q., Bu, S., and Qi, Y., Journal of Non-Crystalline Solids **354** (2008) 3935.

[103] Zberg, B., Uggowitzer, P., and Loffler, J., Nature Materials **8** (2009) 887.

[104] Lu, Z., Shen, J., Xing, D., Sun, J., and Liu, C., Applied Physics Letters **89** (2006) 071910.

[105] Lu, Z. and Liu, C., Materials Transactions **48** (2007) 2476.

[106] Nie, X., Yang, X., and Jiang, J., Journal of Alloys and Compounds **481** (2009) 498.

[107] Zhang, C. Li, N., Pan, J., Guo, S., Zhang, M., and Liu, L., Journal of Alloys and Compounds **504S** (2010) S163.

[108] Takeuchi, A. and Inoue, A., Materials Transactions, JIM **41** (2000) 1372.